AD_____

Award Number: DAMD17-00-1-0217

TITLE: Breast Cancer Diagnosis Using Ultrasound and Diffusive
         Light

PRINCIPAL INVESTIGATOR: Quing Zhu, Ph.D.

CONTRACTING ORGANIZATION: University of Connecticut
                            Storrs, Connecticut   06269-1113

REPORT DATE: September 2003

TYPE OF REPORT: Annual

PREPARED FOR: U.S. Army Medical Research and Materiel Command
                Fort Detrick, Maryland 21702-5012

DISTRIBUTION STATEMENT: Approved for Public Release;
                         Distribution Unlimited

The views, opinions and/or findings contained in this report are
those of the author(s) and should not be construed as an official
Department of the Army position, policy or decision unless so
designated by other documentation.

REPORT DOCUMENTATION PAGE

Form Approved
OMB No. 074-0188

Public reporting burden for this collection of information is estimated to average 1 hour per response, including the time for reviewing instructions, searching existing data sources, gathering and maintaining the data needed, and completing and reviewing this collection of information. Send comments regarding this burden estimate or any other aspect of this collection of information, including suggestions for reducing this burden to Washington Headquarters Services, Directorate for Information Operations and Reports, 1215 Jefferson Davis Highway, Suite 1204, Arlington, VA 22202-4302, and to the Office of Management and Budget, Paperwork Reduction Project (0704-0188), Washington, DC 20503

1. AGENCY USE ONLY *(Leave blank)*	2. REPORT DATE September 2003	3. REPORT TYPE AND DATES COVERED Annual (15 Aug 2002 - 14 Aug 2003)

4. TITLE AND SUBTITLE
Breast Cancer Diagnosis Using Ultrasound and Diffusive Light

5. FUNDING NUMBERS
DAMD17-00-1-0217

6. AUTHOR(S)
Quing Zhu, Ph.D.

7. PERFORMING ORGANIZATION NAME(S) AND ADDRESS(ES)
University of Connecticut
Storrs, Connecticut 06269-1113

E-Mail: qing.zhu@UCONN.EDU

8. PERFORMING ORGANIZATION REPORT NUMBER

9. SPONSORING / MONITORING AGENCY NAME(S) AND ADDRESS(ES)

U.S. Army Medical Research and Materiel Command
Fort Detrick, Maryland 21702-5012

10. SPONSORING / MONITORING AGENCY REPORT NUMBER

11. SUPPLEMENTARY NOTES
Original contains color plates: All DTIC reproductions will be in black and white.

12a. DISTRIBUTION / AVAILABILITY STATEMENT
Approved for Public Release; Distribution Unlimited

12b. DISTRIBUTION CODE

13. ABSTRACT (Maximum 200 Words)
We have developed a novel near-infrared optical technique with ultrasound localization. During the last year, we have made significant progress on using our technique to improve breast cancer diagnosis. Initial results with a group of biopsied patients have shown that early stage invasive cancers present two-fold greater total hemoglobin concentration than fibroadenomas and benign lesions. Initial results of advanced cancers have shown good correlation between cancer angiogenesis distributions imaged by the hybrid imaging technique and histological microvessel density counts. We believe our unique has a great potential to improve current practice on breast cancer diagnosis and monitor treatment responses of advanced cancers.

14. SUBJECT TERMS
Breast cancer diagnosis

15. NUMBER OF PAGES
100

16. PRICE CODE

17. SECURITY CLASSIFICATION OF REPORT Unclassified	18. SECURITY CLASSIFICATION OF THIS PAGE Unclassified	19. SECURITY CLASSIFICATION OF ABSTRACT Unclassified	20. LIMITATION OF ABSTRACT Unlimited

NSN 7540-01-280-5500

Standard Form 298 (Rev. 2-89)
Prescribed by ANSI Std. Z39-18
298-102

Table of Contents

Annual Report of DAMD17-00-1-0217
Quing Zhu (PI)

INTRODUCTION:
Diffuse optical tomography in the near infrared (NIR) is an emerging modality with potential applications in radiology and oncology [1-8]. Optical tomography with NIR light is made possible in a spectrum window that exists within tissues in the 700-900 nm NIR region, in which photon transport is dominated by scattering rather than absorption. Optical tomography offers insight into functional parameters, such as tumor angiogenesis, required for tumor growth and metastasis, tumor hypoxia, indicator of tumor response to various forms of therapy, and tumor metabolism. If a single optical wavelength is used, optical absorption related to tumor angiogenesis and other normal blood vessels can be measured. If two or more optical wavelengths are used, both oxy-hemoglobin and deoxy-hemoglobin concentrations can be measured simultaneously. However, optical tomography alone has not been widely used in clinical studies. The fundamental problem remains the intense light scattering in tissue, which makes the lesion localization difficult.

We have developed a novel near-infrared optical technique with ultrasound localization [9-16]. During the last year, we have made significant progress in clinical studies. Preliminary results with a group of biopsied patients have shown that early stage invasive cancers present two-fold greater total hemoglobin concentration than fibroadenomas and benign lesions [Appendices A and B]. Preliminary results of advanced cancers have shown good correlation between cancer angiogenesis distributions imaged by the hybrid imaging technique and histological microvessel density counts [Appendices C and D]. Our unique approach uses ultrasound localization to overcome the poor localization problem that the diffused light has and thus significantly improves the sensitivity and specificity of optical tomography.

The original tasks proposed in this proposal were

Statement of Work
Task 1:
To simultaneously deploy an ultrasound array and NIR sensors on a hand-held probe and to perform joint acoustic and optical imaging of the target (months 1-8).

a. Complete NIR imaging system by adding two more detector channels (months 1-3).
b. Simultaneously deploy an ultrasound commercial probe and NIR sensors on a hand-held probe and perform calibration of the combined probe with phantoms (months 4-6).
c. Implementing Rytov and Born optical imaging reconstruction algorithms based on the NIR sensor distribution shown in Figure 7 (months 1-6).
d. Perform joint acoustic and optical imaging of testing targets (months 4-8).

Task 2:

To acquire ultrasound and optical image data from 90 patients. To correlate optical deoxy, blood volume, absorption, scattering functional parameters with ultrasound/mammography findings

and to assess the value of optical imaging as an adjunct tool to improve breast cancer diagnosis and to reduce unnecessary biopsies.

a. Refine optical imaging reconstruction algorithms using clinical data (9-24).
b. Perform clinical studies (months 9-24).
Extract ultrasound properties of the lesions and correlate the optical parameters with the ultrasound findings. Biopsy results will be used as diagnosis standard (months 9-24).
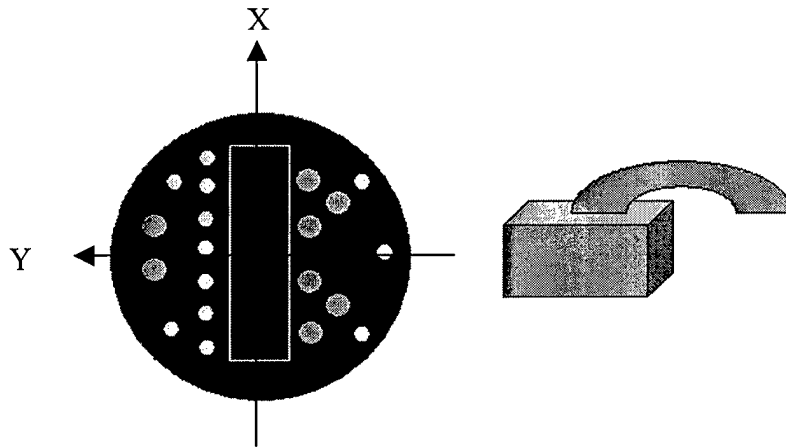
PREGRESS:
Task 1.
The proposed subtasks were all completed. The NIR imager shown in Fig.1 was built, calibrated (10, 12,13), and used at University of Connecticut Health Center and Hartford Hospital to collect data from patients who were scheduled for breast biopsy.

(a)
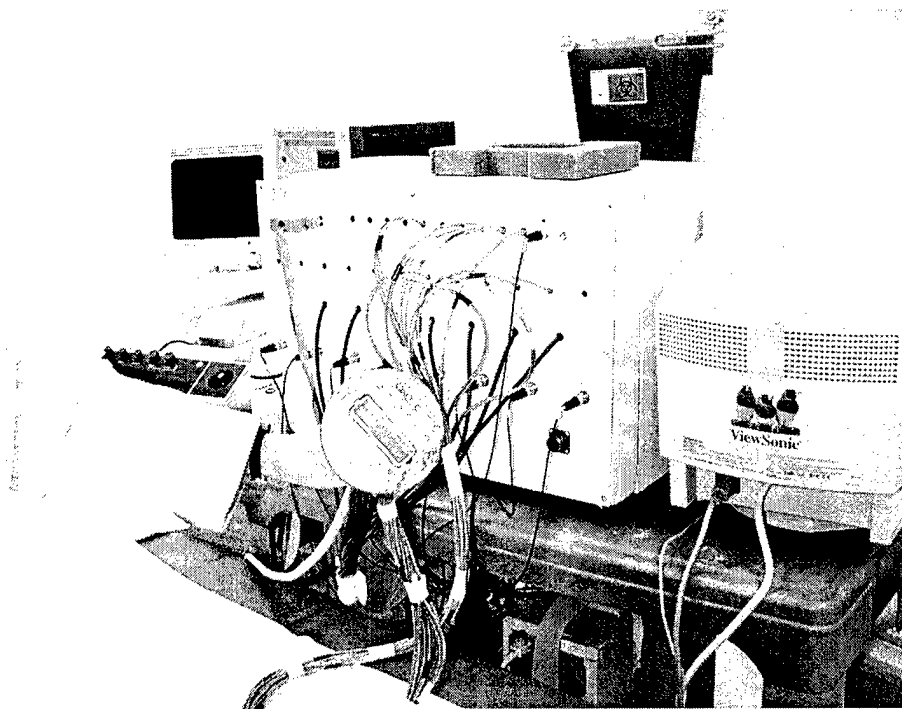
Fig. 1. (a) Picture of the combined probe and the frequency domain NIR imager. (b) Sensor distribution of the combined probe. Smaller circles in (b) are optical source fibers and big circles are detector fibers. A commercial ultrasound probe is located at the center of the combined probe and the optical source and detector fibers are distributed at the periphery of the ultrasound probe.

The optical imaging reconstruction algorithms have been optimized for imaging breast lesions (Appendices A and C). Briefly, the NIR reconstruction takes advantages of ultrasound localization of lesions and segments the imaging volume into finer grid in lesion region and coarser grid in non-lesion regions. A modified Born approximation is used to relate the scattered field measured at the source-detector pairs to absorption variations in each volume element of two regions within the sample. With this dual-mesh scheme, the inverse optical reconstruction is well-conditioned and converges in few iterations.

Task 2:
To acquire ultrasound and optical image data from 90 patients. To correlate optical deoxy, blood volume, absorption, scattering functional parameters with ultrasound/mammography findings and to assess the value of optical imaging as an adjunct tool to improve breast cancer diagnosis and to reduce unnecessary biopsies.

a. Refine optical imaging reconstruction algorithms using clinical data (9-24).
c. Perform clinical studies (months 9-24).
Extract ultrasound properties of the lesions and correlate the optical parameters with the ultrasound findings. Biopsy results will be used as diagnosis standard (months 9-24).

The proposed subtasks are nearly completed. We had initial delay on clinical study at Hartford Hospital. With the help of Hartford Hospital Co-PI Dr. Edward Cronin and Integrated Breast Care Program Coordinator, Roxanne Rotondaro, we have successfully recruited 70 biopsy patients and are continuously recruiting more patients to our study. We expect to complete the enrollment of 90 patients by the end of the year. We have another non-DOD funded clinical site at the University of Connecticut Health Center on combined breast imaging study and 57 patients have been recruited to our study.

Initial results obtained from both clinical sites are very encouraging and have shown that early stage invasive cancers present two-fold greater total hemoglobin concentration than fibroadenomas and other benign lesions [Appendice A and B]. Initial results of advanced cancers have shown that the total hemoglobin distributions are quite heterogeneous and the distributions correlate with histological microvessel density counts [Appendices C and D].

Examples are given here.
Examples of small invasive cancers
The first example is obtained from a 55-year-old woman. Figure 2 (a) shows a gray scale ultrasound image of a non-palpable lesion. The lesion was located at the 4 o'clock position of the right breast. The ultrasound showed a nodular mass with internal echoes and the lesion was considered suspicious. The estimated lesion diameters measured from two orthogonal ultrasound images was 8 mm. An ultrasound guided core needle biopsy was recommended and biopsy result revealed that the lesion was intraductal and infiltrating ductal carcinoma (nuclear grade II, histological grade III). The cancer once removed from the breast measured 1 cm in greater diameter and was composed predominantly of invasive carcinoma (>95%) extending to surgical margins.
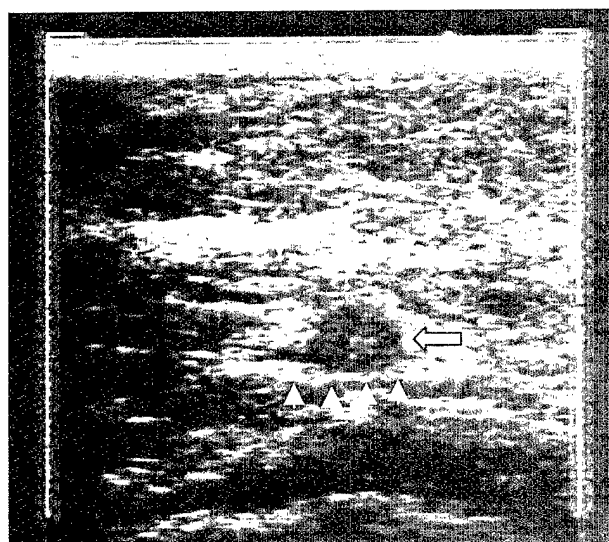
The optical absorption maps at 780nm and 830 nm are shown in Fig. 2(b) and (c), respectively. In both (b) and (c), the first slice is 0.7 cm deep into the breast tissue from the skin surface and the last slice is closer to the chest wall. The spacing of the slices is 0.5 cm. The horizontal and vertical axes of each slice are spatial x and y dimensions of 9 cm in size. The lesion is well resolved in slice #5 and has shown much larger spatial extension at 830 nm than that at 780 nm. The measured maximum absorption coefficients are μ_a^{780}=0.24 cm^{-1} and μ_a^{830}=0.28 cm^{-1}, respectively, and the absorption maximums at both wavelengths are located at (0 1.0 2.25) cm, which is close to the lesion center measured by ultrasound.

The total hemoglobin distribution of the lesion is shown in Fig.2(d). The measured maximum total hemoglobin concentration for lesion is 122.03 μmoles, and the measured average background hemoglobin concentration is 13.73 μmoles. The spatial extent of lesion's angiogenesis is measured from the full width at half maximum (FWHM) of the total hemoglobin map and it is estimated to be 2 cm. This number is about two times larger than the 8 mm diameter measured by ultrasound and suggests that optical contrasts extend well beyond the cancer periphery because of angiogenesis. This example suggests that the 1cm sample removed from the breast with invasive cells extending to surgical margins is not large enough and 2 cm cancer size imaged with NIR may be a good estimation.

Another example was obtained from a 56-year-old woman who had a non-palpable lesion located at the 10 o'clock position of the left breast. Ultrasound showed a solid mass with internal echoes measuring 9 mm in size and the lesion was considered suspicious (see Fig.3(a)). An ultrasound guided core needle biopsy was recommended and biopsy results revealed that the lesion was in-situ and invasive ductal carcinoma with ductal and lobular features (nuclear grade II, histological grade II). The tumor once removed from the breast measured 1.5 cm in greater diameter and was composed predominantly of invasive carcinoma (>80%) extending to inferior/anterior surgical margin.
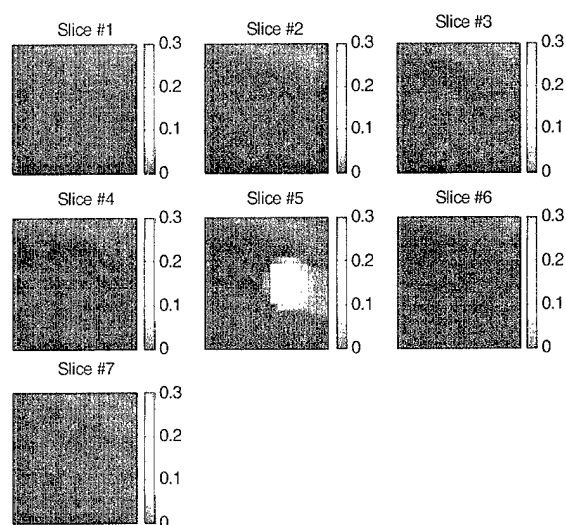
The optical absorption maps at both 780 nm and 830 nm wavelengths are shown in Fig.3 (b) and (c), respectively. In (b) and (c), the first slice is 0.4 cm deep into the breast tissue from the skin surface and the last slice is closer to the chest wall. The spacing between the slices is 0.5 cm. This lesion is well resolved in slice #4 and has shown much larger spatial extension at 780 nm than that at 830 nm. The measured maximum absorption coefficients are $\mu_a^{780}=0.29$ cm^{-1} and $\mu_a^{830} = 0.25$ cm^{-1}, respectively. The absorption maximums at both wavelengths are located at (0 1.0 1.9000) cm, which is very close to the lesion center measured by ultrasound. The calculated maximum total hemoglobin concentration of the lesion is 127.60 μmoles, and the background concentration is 24.16 μmoles. The measured FWHM of the total hemoglobin map is 3.5 cm, which is more than three times larger than 9 mm diameter measured by ultrasound and again suggests that optical contrasts extend well beyond the cancer periphery due to angiogenesis.
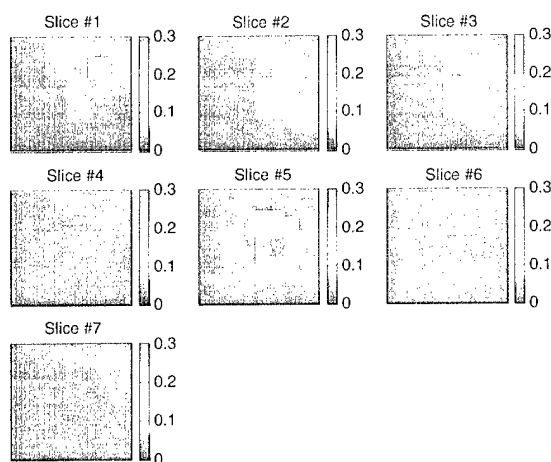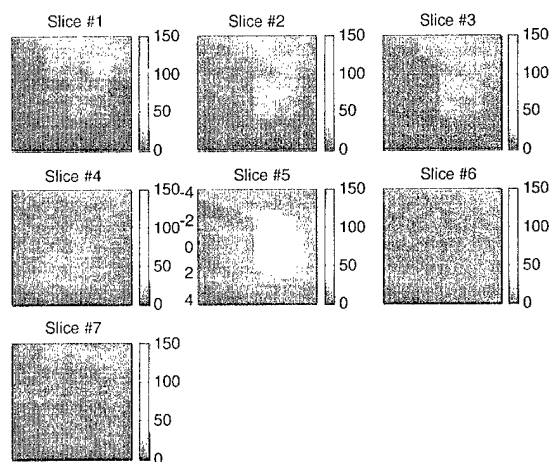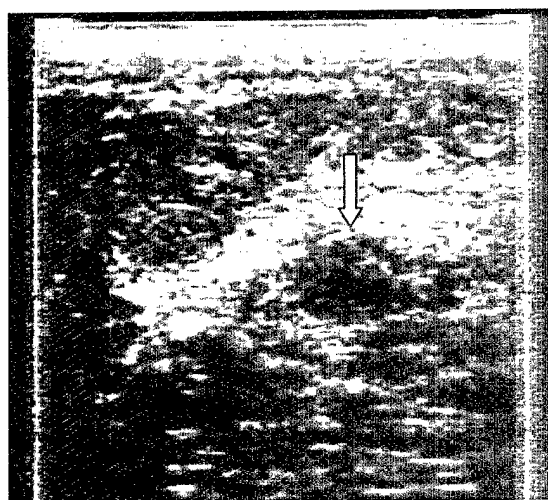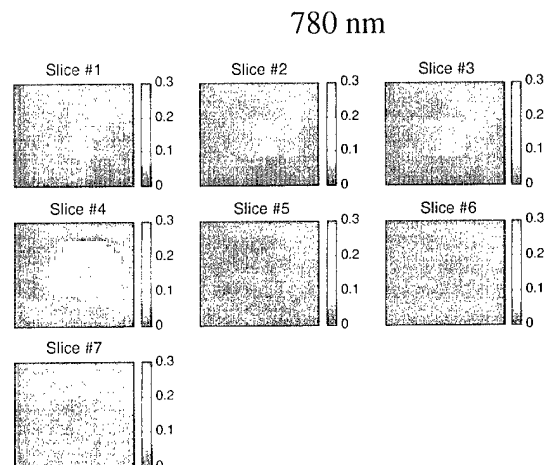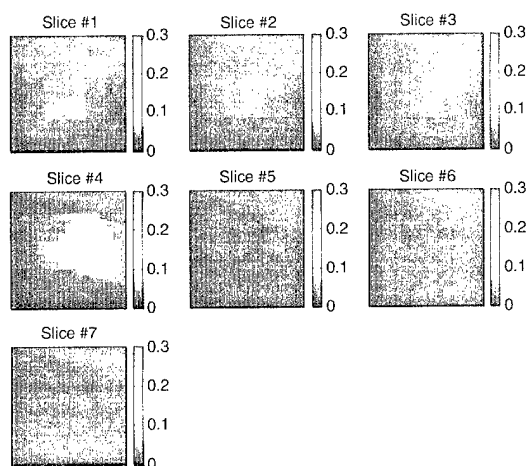
780nm

(a)

(b)

830 nm

(c)

(d)

Fig. 2. (a) shows a gray scale ultrasound image of a non-palpable lesion of a 55-year-old woman. The lesi pointed by the arrow was located at the 4 o'clock position of the right breast measuring 8 mm in diamet Ultrasound showed nodular mass with internal echoes and the lesion was considered suspicious. (b) and (c are optical absorption maps at 780 nm and 830 nm, respectively. x and y axes are spatial dimensions of 9 cr by 9 cm. The slices beginning from left to right correspond to absorption maps from 0.7 cm underneath ski surface to chest wall in 0.5 cm spacing. (d) is the total hemoglobin concentration and the vertical scale is i micro moles.
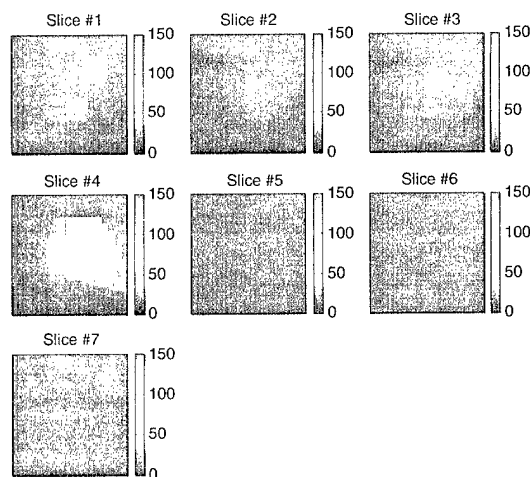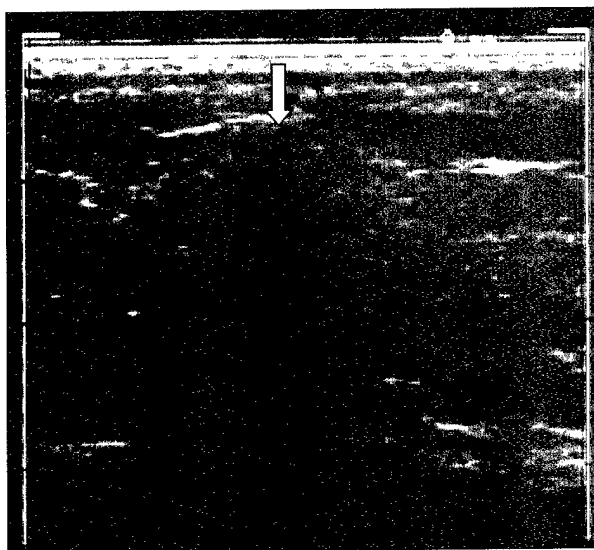
780 nm

(a)

(b)

(c)

(d)

Fig. 3. This example was obtained from a 56-year-old woman who had non-palpable lesion located at the o'clock position of the left breast. Ultrasound showed a solid mass (a) with internal echoes measuring 9 n in size and the lesion was considered suspicious. (b) and (c) are optical absorption maps at 780 nm and 83 nm, respectively. The slices beginning from left to right correspond to absorption maps from 0.4 cr underneath skin surface to chest wall in 0.5 cm spacing. (d) is the total hemoglobin concentration and th vertical scale is in micro moles.

Example of fibroadenoma and another benign lesions

Figure 4 (a) shows an ultrasound image of a hypoechoic mass of a 37-year-old woman. The diagnosis was that the lesion likely was a fibroadenoma; however, there was concern that the lesion

could be a carcinoma because of the irregular shape and the posterior shadowing seen by ultrasound. An ultrasound guided core breast biopsy revealed that the lesion was simply a fibroadenoma.

Optical absorption maps are shown in Fig. 4(b) and (c) as well as the total hemoglobin distribution in (d). Compared with the invasive cancer cases, the spatial distributions of the absorption coefficient as well as the total hemoglobin concentration are quite diffused and higher absorption region at 8^ nm corresponds to lesion region seen by ultrasound. The measured maximum lesion absorpti coefficients at 780 nm and 830 nm are $\mu_a^{780} = 0.10$ cm^{-1} and $\mu_a^{830} = 0.12$ cm^{-1}, respectively, and the values are less than half of those small invasive cancer cases. The calculated maximum tot. hemoglobin concentration is 52 μ moles and the background hemoglobin concentration is 14 μ moles. The calculated average maximum total hemoglobin concentration from four NIR images acquired at lesion region is 59 μ moles ($\pm$ 5.1 μ moles) and the average background is 16 μ moles ($\pm$ 1.0 μ moles).

780 nm

(a)

(b)

830 nm

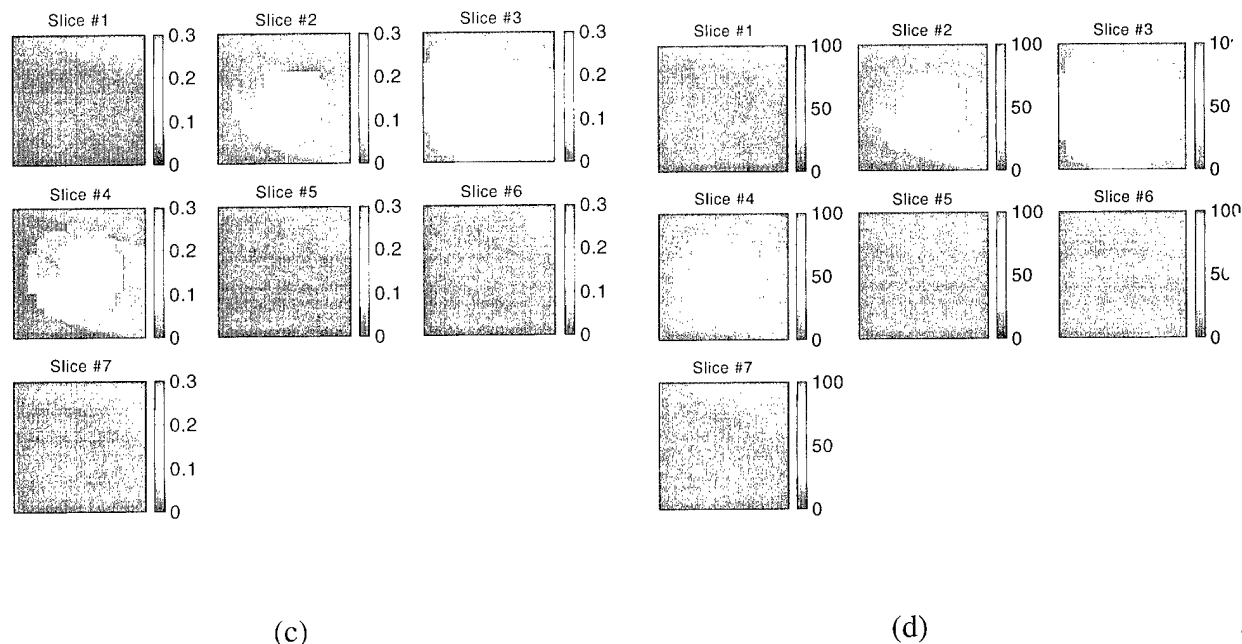(c)   (d)
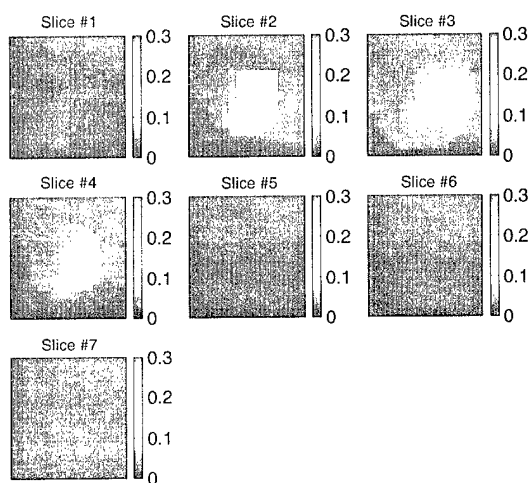
Fig.4. (a) shows an ultrasound image of a solid hypoechogenic lesion located at 9 to 10 o'cloc ⟨ position of a 37-year-old woman. The diagnosis was that the lesion could represent fibroadenom. , however, there was a chance that the lesion could be a carcinoma because of the irregular shape an ↿ posterior shadow seen by ultrasound. (b) and (c) are optical absorption maps at 780 nm and 830 nm , respectively. The slices starting from 0.5 cm underneath skin surface to chest wall in 0.5 cm spacing. (d) is the total hemoglobin concentration.

The statistics of maximum total hemoglobin concentration of three groups obtained from the 1ˈ cases are given in Ref 15 (Appendix A). The benign group of fibroadenoma (15 cases) an ↿ hyperplasia (1 case) has an average of 67 μmoles ($\pm$ 17.0 μmoles), the combined fibrocystic chan and non-invasive neoplasia/carcinoma in situ case has a maximum of 48 μmole, and the invas cancer group of 2 cases have shown about twofold greater average of 119 μmoles ($\pm$ 1.6 μmole; If average total hemoglobin concentration is use, the values are 46 μmoles ($\pm$ 11.3 μmoles), ɔ μmoles and 86 μmoles ($\pm$ 2.12 μmoles), for the three corresponding groups, respectively. The malignant group also presents about two-fold greater average hemoglobin concentration than that oᶠ the benign group. The average sizes of lesions of the three groups measured by ultrasound are 1.05 cm ($\pm$ 0.3 cm), 1.1 cm, 0.9 cm ($\pm$ 0.07 cm), respectively. The lesion size is the geometric mean of diameters measured in x and z dimensions.

Recently, we have completed data analysis of 15 patients (5 malignant cancers and 16 beni; ı lesions). These 15 patients were representative examples of the 70 patients recruited froɩ ı Hartford Hospital. The results of this group of biopsied patients have shown that sma l invasive cancers can be well-resolved in 3D optical absorption maps. The average maximuɩ ı total hemoglobin concentrations for malignant and benign groups are 110.3 μmoles and 47 ˊ

μ moles, respectively. The malignant group presents more than two-fold greater total hemoglobin concentration than that of the benign group. These results agree with earlier data obtained from University of Connecticut Health Center. The manuscript that reports these findings is attached (Appendix B).

Evidence that hybrid imaging technique can be used for assessing chemotherapy response and tumor perfusion

During the diagnostic imaging study, we scanned a patient who was undergoing chemotherapy. This 44-year-old woman had a large 4 cm x 4 cm x 1.5 cm palpable mass (Fig.5(a)) located at the 6 to 8 o'clock position of the left breast. The lesion was considered as highly suspicious for malignancy and an ultrasound guided needle biopsy revealed that the lesion was a high-grade invasive carcinoma with necrosis. Optical absorption maps of both wavelengths are shown in Fig. 5(b) and (c) and the distributions are highly heterogeneous with high absorption at cancer periphery. Slice 1 is the spatial x-y image of 9 cm x 9 cm obtained at 0.5 cm deep from the skin surface. Slice 7 is 3.5 cm deep toward the chest wall and the spacing between slices is 0.5 cm. The total hemoglobin concentration map is shown in Fig.5 (d) and the maximum and average hemoglobin concentrations are 92.12 μ moles and 26.20 μ moles. Since this cancer was too large for breast conserving surgery, the patient was treated with chemotherapy in the neo-adjuvant setting for three months. At the time the patient completed the chemotherapy, we imaged her again with the combined probe. Fig.6 (a) is the ultrasound image of the caner three month later and the cancer contrast was poor and cancer boundaries were completely unclear due to treatment. Fig.6 (b) and (c) are optical absorption maps at both wavelengths and (d) is the total hemoglobin distribution. The maximum and average hemoglobin concentrations of the lesion are 83.03 μ moles and 26.07 μ moles, respectively. Compared with the images acquired before treatment, the spatial extent of the angeogenesis pattern is much smaller and more confined to the core area. The maximum total hemoglobin concentration is reduced by about 10 μ moles and the average is about the same as before. This example clearly demonstrates the feasibility of monitoring the treatment using the combined technique.

To correlate the NIR images with vessel densities, Dr. Poornima Hegde, a pathologist at the University of Connecticut Health Center, performed micro-vessel density counts. Two samples obtained at breast-conservation surgery marked with lateral and anterior positions were used for counting. Sections 3 to 5 micrometer thick were stained on an immunohistochemistry slide staining system (DAKO autostainer) with factor 8/86 mouse monoclonal antibody (anti-human von Willebrand factor, DAKO Corp, Carpinteria, Calif) at 1:100 dilution digested by proteinase K for 3 minutes, by labeled polymers (DAKO EnVision plus) immunoperoxidase method. The microvessel density counts were performed in ten consecutive fields with the use of an ocular grid at X200 magnification. The first field chosen was a hotspot (area of maximum vascular density either within the infiltrating tumor mass or at the tumor-stromal interface). The total number of microvessels were 196 (lateral) and 114 (anterior) per 10 consecutive fields, respectively. These high counts correlate well with the high optical absorption and total hemoglobin concentration shown in Fig.6(b)-(d) NIR images.
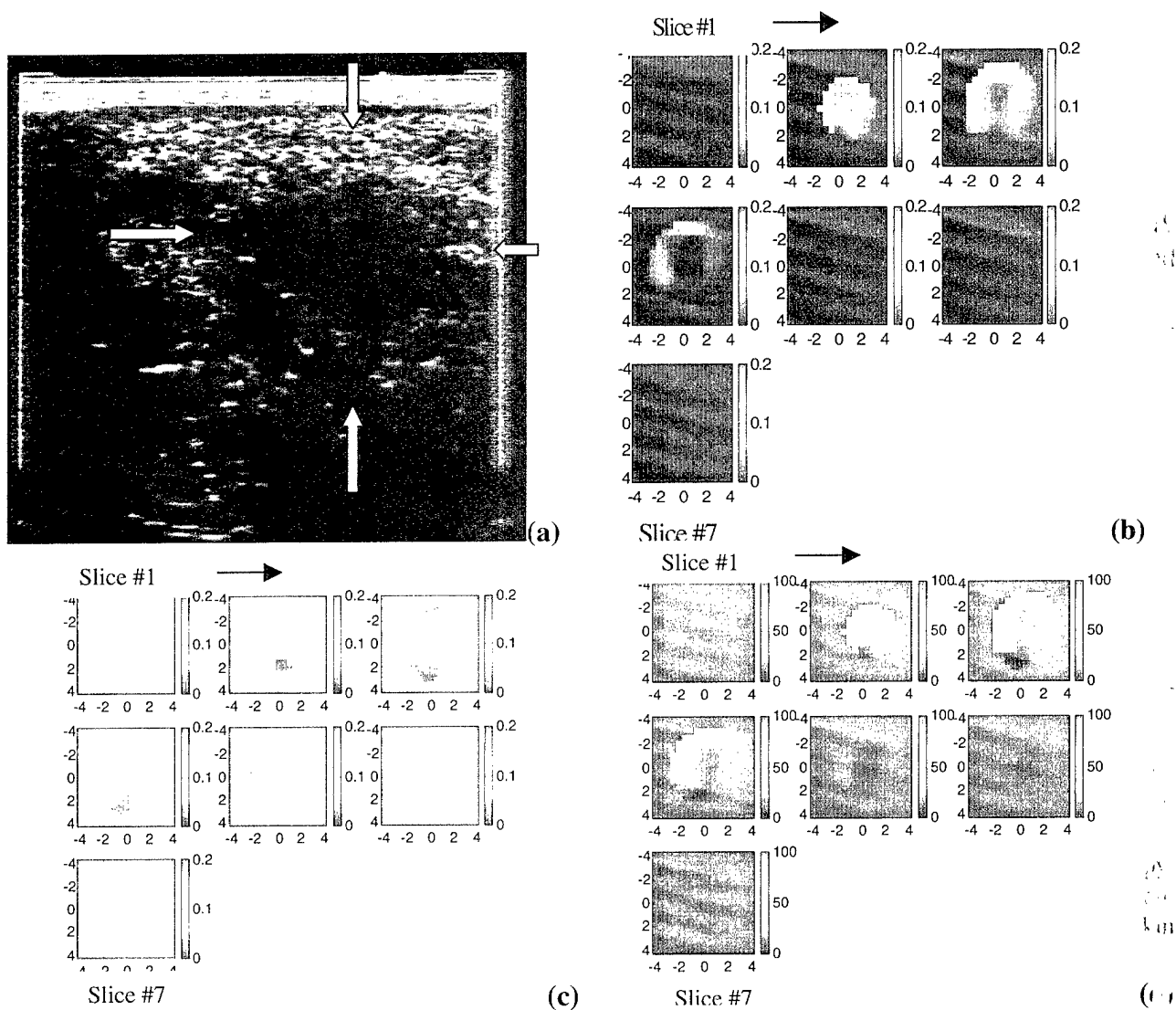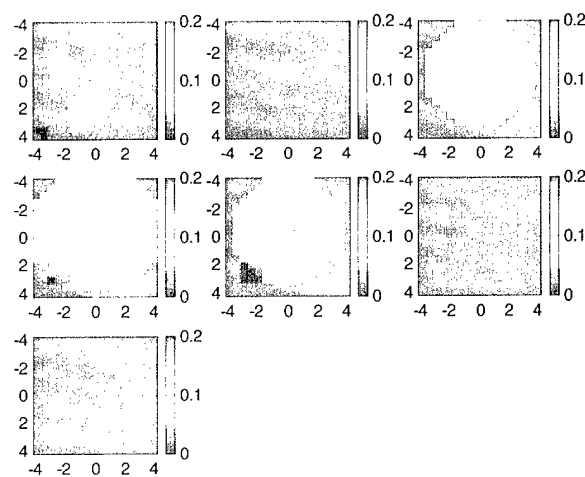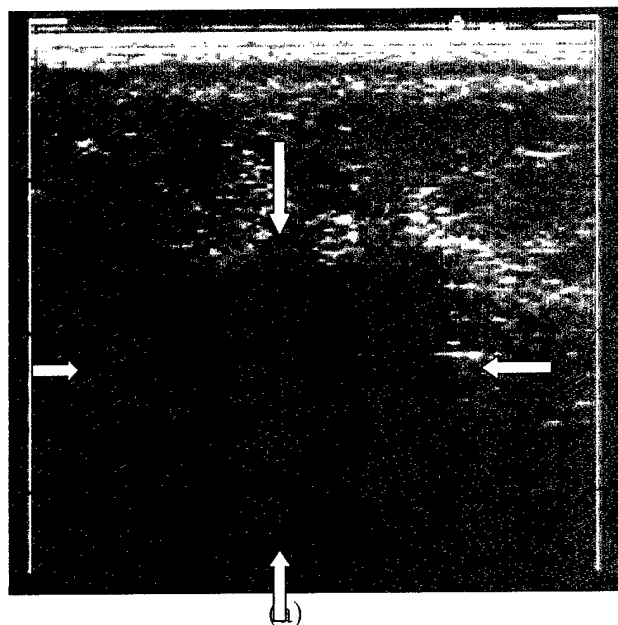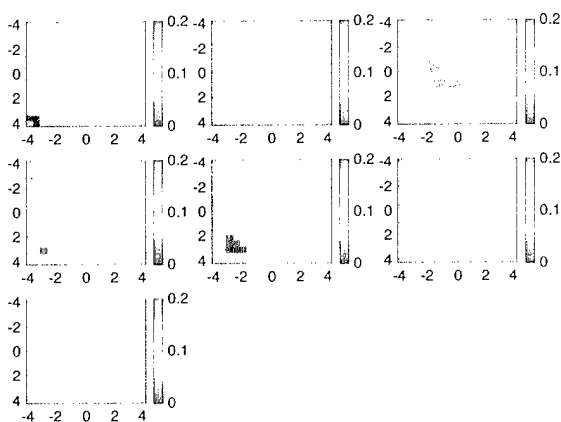
Figure 5. (a) Ultrasound image of a large cancer obtained from a 44-year-old woman before chemotherapy. (b) Optical absorption map at 780 nm. (c) Optical absorption map at 830 nm. (d) Total hemoglobin concentration of the lesion. Slice #1 is 0.5 deep from the skin surface. Slice #7 is 3.5 cm deep from the skin surface. The spacing between slices is 0.5 cm. [from Ref. 14].
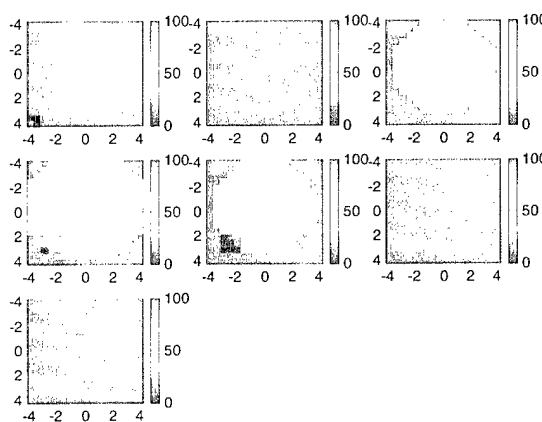
Figure 6(ID19P10). (a) Ultrasound image of the cancer treated with chemotherapy for three month;
(b) Optical absorption map at 780 nm. (c) Optical absorption map at 830 nm. (d) Total hemoglobi
concentration of the lesion.

The second imaging example was obtained from a 47-year-old woman who had a lump at 2 o'cloç
in her left breast. Ultrasound showed hypoechoic mass with irregular margins (see Fig. 7(a)) and th ;
lesion was considered as highly suspicious for malignance. Fig.7 (b) and (c) are optical absorpti
maps obtained at 780 nm and 830 nm and the vertical scale of (b) and (c) is half of that used in Fi; ;
(b) and (c). Fig. 7(d) is the total hemoglobin concentration distribution and the vertical scale is ;
same as that used in Fig. 6(d). The light absorption at both wavelengths is much lower than t
previous example but the distributions are highly heterogeneous. The measured maximu
absorption coefficients at 780 nm and 830 nm are 0.08 cm^{-1} and 0.10 cm^{-1}, respectively. The
measured maximum total hemoglobin concentration of the tumor and average background are 40.;
μmoles and 10.6 μmoles, respectively. Surgical pathology report revealed that the mass was
infiltrating carcinoma (histological grade II, nuclear grade II) with low mitotic activity. The total
counts of microvessels obtained from anterior and posterior core biopsy samples were 61 and 40 p

10 consecutive fields, respectively. The total counts measured from anterior and posterior surgical samples were 52 and 29, respectively. These low counts correlate well with the low optical absorption shown in Fig. 7 (b)-(c) and indicate that the tumor was poorly perfused.

These two examples demonstrate that NIR images correlate with microscopic angiogenesis distributions and the NIR imaging technique has a great potential for assessing tumor perfusion and therefore predicting treatment responses.
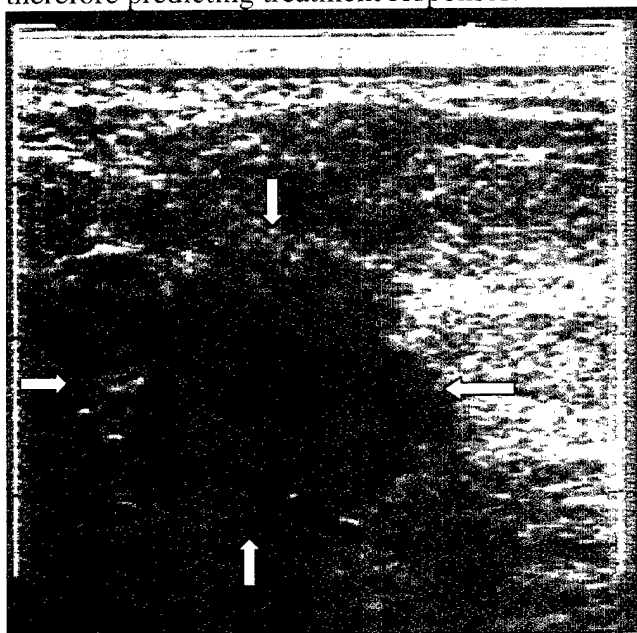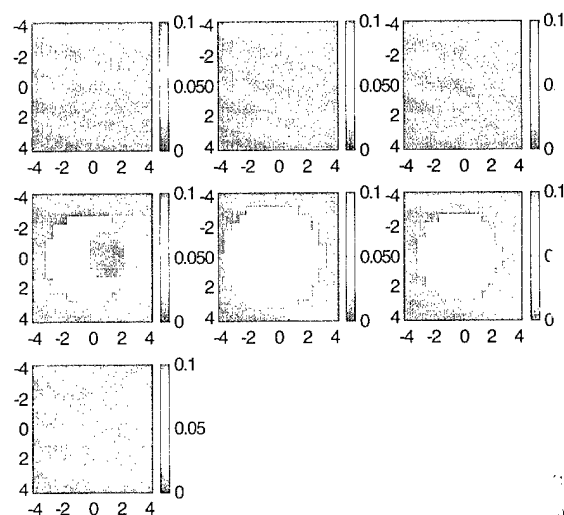
(a)　　　　　　　　　　　　　　　(b)
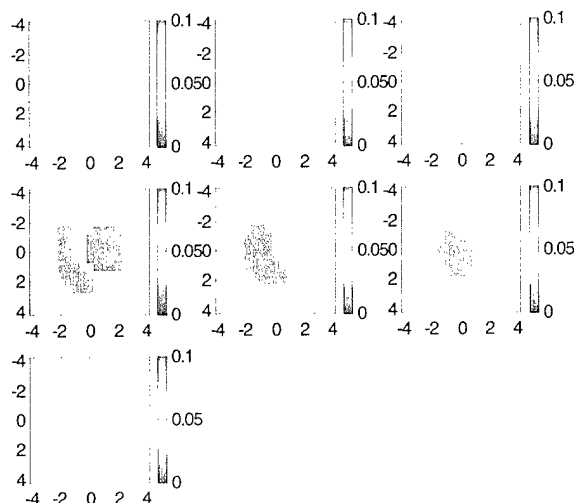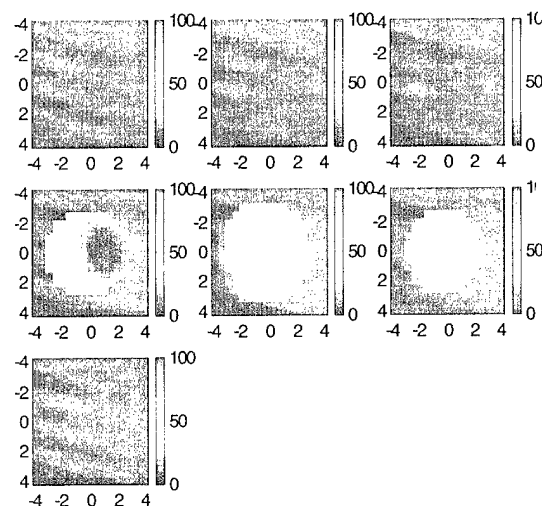
(c)　　　　　　　　　　　　　　　(d)

Figure 7 (ID5). (a) Ultrasound image of a 47-year-old woman with a highly suspicious lesion located at 2'oclock position of her left breast. (b) Optical absorption map at 780 nm. (c) Optical absorption map at 830 nm. Note the scales for Fig. 7(b) and (c) is half of that used in Fig. 6(b) and(c). (d) Total hemoglobin concentration of the lesion. The scale is the same as the Fig.6 (d).

To establish the statistic power of this novel technique on cancer diagnosis, we are continuously recruiting more patients to this study.

KEY RESEARCH ACCOMPLISHMENT:
- Initial results with a group of biopsied patients have shown that early stage invasive cancers present two-fold greater total hemoglobin concentration than fibroadenomas and benign lesions [Appendices A and B].
- Preliminary results of advanced cancers have shown good correlation between cancer angiogenesis distributions imaged by the hybrid imaging technique and histological microvessel density counts [Appendices C and D].

Publications resulting from this DOD support (august 2002 to present)

Published and In Press
Zhu Q., Chen NG, and Kurtzman SH, "Imaging tumor angiogenesis by use of combined near-infrared diffusive light and ultrasound," Optics Letter, Vol. 28, No. 5, pp 337-339 (March, 2003).

Zhu Q., Huang MM, Chen NG, Zarfos K, Jagjivan B, Kane M, Kurtzman HS, "Ultrasound-guided optical tomographic imaging of malignant and benign breast lesions: initial clinical results of 19 cases," Neoplasia, in press.

Chen NG and Zhu Q, "Time-resolved optical measurements with spread spectrum excitations," Optics Letters, Vol. 27, No. 20, pp 1806-1808 (Oct. 2002).

Huang MM, Xie TQ, Chen NG, and Zhu Q., "Simultaneous reconstruction of absorption and scattering maps with ultrasound localization: feasibility study using transmission geometry," Applied Optics, July 1 issue, 2003.

Submitted
Zhu Q., Kurtzman HS, Hegde, P, Huang MM, Chen NG, Jagjivan B, Kane M, Zarfos K, "Imaging heterogeneous tumor angiogenesis distributions of advanced breast cancers by optical tomography with ultrasound localization," submitted to Proc. of Nat. Ac. of Sci. (July 2003).

Chen NG, Huang MM, Xia HJ, Piao DQ, and Zhu Q, "Potable near infrared diffusive light imager for breast cancer detection," submitted to Journal of Biomedical Optics.

Yuan BH, Chen NG, Zhu Q., "Absorption and Emission Properties of Indocyanine Green in Intralipid Solution," submitted to Journal of Biomedical Optics, July 2003.

Huang MM and Zhu Q, "Dual-mesh Optical Imaging Reconstruction with Depth Correction," submitted to Applied Optics,(August 2003).

To be submitted:
Zhu, Q, Cronin E, Currie A, Huang MM, Chen NG, ChenX, Benign versus Malignant Breast Masses: Optical Differentiation with US Localization (work in progress), to be submitted to Radiology.

Conference Proceedings (Since August 2002)
Zhu Q, Kurtzman, S, Chen, NG, Zarfos, K, Huang, MM, Kane M, "Breast lesion diagnosis using combined near infrared and ultrasound," SPIE Photonics West, San Jose, CA, January, 2003. in SPIE Proceeding of Optical Tomography and Spectroscopy of Tissue, in press.

Chen NG and Zhu Q, "Spread spectrum time-resolved photon migration imaging system: the principle and simulation results", SPIE Photonics West, San Jose, CA, January, 2003, in SPIE Proceeding of Optical Tomography and Spectroscopy of Tissue, in press.

Chen NG, Piao DQ, Xia HJ and Zhu Q," Portable multi-channel, multi-wavelengh near infrared imager," SPIE Photonics West, San Jose, CA, January, 2003, in SPIE Proceeding of Optical Tomography and Spectroscopy of Tissue, in press.

Chen NG and Zhu Q, "Fluorescence decay profile measured by spread spectrum excitation method," SPIE Photonics West, San Jose, CA, January, 2003, in SPIE Proceeding of Optical Tomography and Spectroscopy of Tissue, in press.

Huang MM, Chen NG, Yuan, B, Zhu Q," Three-dimensional near-infrared diffusive wave imaging with ultrasound localization," SPIE Photonics West, San Jose, CA, January, 2003. in SPIE Proceeding of Optical Tomography and Spectroscopy of Tissue, in press.

Guo PY, Yan SK and Zhu Q, "Three-Dimensional simultaneous ultrasound and near-infrared imaging," SPIE Photonics West, San Jose, CA, January, 2003. in SPIE Proceeding of Optical Tomography and Spectroscopy of Tissue, in press.

CONCLUSIONS:
We have developed a novel near-infrared optical technique with ultrasound localization. During the last year, we have made significant progress on using our technique to improve breast cancer diagnosis. Initial results with a group of biopsied patients have shown that early stage invasive cancers present two-fold greater total hemoglobin concentration than fibroadenomas and benign lesions. Initial results of advanced cancers have shown good correlation between cancer angiogenesis distributions imaged by the hybrid imaging technique and histological microvessel density counts.
We believe our unique has a great potential to improve current practice on breast cancer diagnosis and monitor treatment responses of advanced cancers.

REFERENCES:
1. Yodh A and Chance B (1995). Spectroscopy and imaging with diffusing light. Phys. Today. **48**, 34-40.
2. Tromberg B, Shah N, Lanning R, Cerussi A, Espinoza J, Pham T, Svaasand L, and Butler J (2000). Non-Invasive in vivo characterization of breast tumors using photon migration spectroscopy. Neoplasia vol.2, No 1:2: 26-40.

3.   Franceschini MA, Moesta KT, Fantini S, Gaida G, Gratton E, Jess H, Seeber M, Schlag PM, Kashke M (1997). Frequency-domain techniques enhance optical mammography: initial clinical results. Proc. of Nat. Ac. of Sci., 94: 6468-6473.

4.   Pogue B, Poplack SP, McBride TO, Wells WA, Osterman K, Osterberg U, and Paulsen KD (2001). Quantitative hemoglobin tomography with diffuse near-infrared spectroscopy: pilot results in the breast. Radiology, 218: 261-266, 2001.

5. Dehghani H, Pogue B, Poplack SP, and Paulsen KD (2003). Multiwavelength three-dimensional near-infrared tomography of the breast: initial simulation, phantom, and clinical results. Applied Optics, 42 (1), 135-145.

6.   Ntziachristos V, Yodh A, Schnall M., and Chance B (2000). Concurrent MRI and diffuse optical tomography of breast after indocyanine green enhancement. Proc. of Nat. Ac. of Sci., 97 (6), 2267-2772.

Jiang H, Xu Y, Iftimia N, Eggert J, Klove K, Baron L and Fajardo L (2001). Three-dimensional optical tomographic imaging of breast in a human subject. IEEE Trans on Medical Imaging, 20(12), 1334-1340.

Jholboke M, Tromberg B, Li X, Shah N, Fishkin J, Kidney D, Butler J, Chance B, and Yodh A (2000). Three-dimentional diffuse optical mammography with ultrasound localization in human subject. Journal of Biomedical Optics 5(2), 237-247.

9. Zhu Q, Dunduran T, Holboke M, Ntziachristos V and Yodh A(1999). Imager that combines near infrared diffusive light and ultrasound. Optics Letters, 24(15), 1050-1052.

10.   Chen NG, Guo PY, Yan SK, Piao DQ, and Zhu Q (2001). Simultaneous near infrared diffusive light and ultrasound imaging. Applied Optics, 40 (34), 6367-6380.

11.   Zhu Q, Conant E, and Chance B (2000). Optical imaging as an adjunct to sonograph in differentiating benign from malignant breast lesions. Journal of Biomedical Optics, 5 (2), 229-236.

12. Zhu Q, Chen NG, Piao DQ, Guo PY and Ding XH (2001). Design of near infrared imaging probe with the assistance of ultrasound localization. Applied Optics, 40(19), 3288-3303.

13.   N. G. Chen and Q. Zhu, "Characterization of small absorbers inside turbid media," Optics Letters, Vol 27, No. 4, pp 252-254 (2002).

14.   Zhu Q, Chen NG, Kurtzman HS (2003). Imaging tumor angiogenesis by the use of combined near infrared diffusive light and ultrasound. Optics Letters, 28 (5), 337-339.

15. Zhu, Q., Huang, MM, Chen, NG, Zarfos, K, Jagjivan, B, Kane, M, Kurtzman, HS, "Ultrasound-guided optical tomographic imaging of malignant and benign breast lesions: initial clinical results of 19 cases," Neoplasia, in press.

Appendices

A. Zhu Q., Huang MM, Chen NG, Zarfos K, Jagjivan B, Kane M, Kurtzman HS, "Ultrasound-guided optical tomographic imaging of malignant and benign breast lesions: initial clinical results of 19 cases," Neoplasia, in press.

B. Zhu, Q, Cronin E, Currie A, Huang MM, Chen NG, ChenX, Benign versus Malignant Breast Masses: Optical Differentiation with US Localization (work in progress), to be submitted to Radiology.

C. Zhu Q., Chen NG, and Kurtzman SH, "Imaging tumor angiogenesis by use of combined near-infrared diffusive light and ultrasound," Optics Letter, Vol. 28, No. 5, pp 337-339 (March, 2003).

D. Zhu Q., Kurtzman HS, Hegde, P, Huang MM, Chen NG, Jagjivan B, Kane M, Zarfos K, "Imaging heterogeneous tumor angiogenesis distributions of advanced breast cancers by optical tomography with ultrasound localization," submitted to Proc. of Nat. Ac. of Sci. (July 2003).

E. Chen NG and Zhu Q, "Time-resolved optical measurements with spread spectrum excitations," Optics Letters, Vol. 27, No. 20, pp 1806-1808 (Oct. 2002).

F. Huang MM, Xie TQ, Chen NG, and Zhu Q., "Simultaneous reconstruction of absorption and scattering maps with ultrasound localization: feasibility study using transmission geometry," Applied Optics, July 1 issue, 2003.

Ultrasound-Guided Optical Tomographic Imaging of Malignant and Benign Breast Lesions: Initial Clinical Results of 19 Cases[1]

Quing Zhu*, Minming Huang*, NanGuang Chen*, Kristen Zarfos[†], Bipin Jagjivan[†], Mark Kane[†], Poornima Hedge[†] and Scott H. Kurtzman[†]

*Bioengineering Program, Electrical and Computer Engineering Department, University of Connecticut, Storrs, CT 06269-2157, USA; [†]University of Connecticut Health Center, Farmington, CT 06030, USA

Abstract

The diagnosis of solid benign and malignant tumors presents a unique challenge to all noninvasive imaging modalities. Ultrasound is used in conjunction with mammography to differentiate simple cysts from solid lesions. However, the overlapping appearances of benign and malignant lesions make ultrasound less useful in differentiating solid lesions, resulting in a large number of benign biopsies. Optical tomography using near-infrared diffused light has great potential for imaging functional parameters of 1) tumor hemoglobin concentration, 2) oxygen saturation, and 3) metabolism, as well as other tumor distinguishing characteristics. These parameters can differentiate benign from malignant lesions. However, optical tomography, when used alone, suffers from low spatial resolution and target localization uncertainty due to intensive light scattering. Our aim is to combine diffused light imaging with ultrasound in a novel way for the detection and diagnosis of solid lesions. Initial findings of two early-stage invasive carcinomas, one combined fibroadenoma and fibrocystic change with scattered foci of lobular neoplasia/lobular carcinoma in situ, and 16 benign lesions are reported in this paper. The invasive cancer cases reveal about two-fold greater total hemoglobin concentration (mean 119 mol) than benign cases (mean 67 mol), and suggest that the discrimination of benign and malignant breast lesions might be enhanced by this type of achievable optical quantification with ultrasound localization. Furthermore, the small invasive cancers are well localized and have wavelength-dependent appearance in optical absorption maps, whereas the benign lesions appear diffused and relatively wavelength-independent.
Neoplasia (2003) 5

Keywords: breast cancer detection and diagnosis, optical tomography, ultrasound imaging, tumor angiogenesis.

Introduction

Ultrasound imaging is a well-developed medical diagnostic tool that is used in conjunction with mammography for the differentiation of simple cysts from solid lesions in breast examinations [1]. When the criteria for a simple cyst are strictly adhered to, the accuracy of ultrasound is 96% to 100% [2]. Ultrasound specificity in breast cancer detection, however, is not high as a result of the overlapping characteristics of solid benign and malignant lesions [3,4]. The insufficient predictive value of ultrasound has prompted radiologists to recommend biopsies on most solid nodules, which result in a large number of biopsies yielding benign breast lesions. Currently, 70% to 80% percent of such biopsies yield benign findings [5]. In addition, the diagnostic accuracy of ultrasound depends largely on the experience of physicians.

Diffuse optical tomography in the near-infrared (NIR) is an emerging modality with potential applications in radiology and oncology [6–13]. Optical tomography with NIR light is made possible in a spectrum window that exists within tissues in the 700- to 900-nm NIR region, in which photon transport is dominated by scattering rather than absorption. Optical tomography offers several functional parameters to differentiate malignant cancers from benign lesions. It has been shown that breast cancers have higher blood volumes than nonmalignant tissues because of angiogenesis [14]. Tumor blood volume and microvascular density are parameters anatomically and functionally associated with tumor angiogenesis. If a single optical wavelength is used, optical absorption related to tumor angiogenesis and other normal blood vessels can be measured. If two or more optical wavelengths are used, both oxyhemoglobin (oxyHb) and deoxyhemoglobin (deoxyHb) concentrations can be measured simultaneously. However, optical tomography alone has not been widely used in clinical studies. The fundamental problem of intense light scattering remains, which makes the target localization difficult, especially for small lesions. In general, localization or imaging based on tomographic inverse scattering approaches suffers from low spatial resolution and location uncertainty, and the inversion problem

is, in general, underdetermined and ill posed. The image reconstruction results depend on many parameters, such as the system signal-to-noise ratio, regularization schemes used in inversion, and so on.

Due to the abovedescribed deficiencies, literature data on optical tomography have been limited to feasibility studies or case reports [7–13]. However, these deficiencies can be overcome by a novel technique using a combination of NIR diffusive light and ultrasound [15–18]. The combined imager consists of a hand-held probe housing a commercial ultrasound probe and NIR source and detectors for coregistration. Ultrasound is used to scan suspicious lesions, whereas coregistered optical measurements are used to image and characterize the functional parameters of the lesions. With the *a priori* knowledge of lesion structure initially obtained by ultrasound, the tissue volume can be approximately segmented into a lesion region and a background region; optical reconstruction from the optical measurements can be performed by using finer imaging voxel size corresponding to the lesion region and coarse voxel size corresponding to the background region [18]. Consequently, the image reconstruction is well defined because the total number of imaging voxels with unknown optical properties is reduced significantly. In addition, the reconstruction is less sensitive to noise because the weight matrix is appropriately scaled for inversion, and convergence can be achieved within a small number of iterations.

In this paper, we report our initial clinical results of using the combined technique to image and characterize ultrasonically detected breast lesions. A total of 18 patients (19 cases) of invasive breast carcinomas (2 cases), combined fibroadenoma and fibrocystic changes with scattered foci of lobular neoplasia/lobular carcinoma *in situ* (noninvasive carcinoma; 1 case), juvenile atypical ductal hyperplasia (1 case), and fibroadenomas and fibrocystic changes (15 cases) are reported here. The diameters of these lesions are on the order of 1 cm. For the first time, we report high sensitivity of optical tomography in diagnosing early-stage invasive cancers and in differentiating them from small benign lesions. We also show a highly localized pattern of angiogenesis distribution of small invasive cancers. Our initial results are very encouraging and suggest that the discrimination of benign and malignant breast masses could be enhanced by this type of achievable optical quantification coupled with ultrasound localization.

Materials and Methods

The major technical aspects of our combined imaging technique have been described in detail previously [16]. Briefly, the NIR system consists of 12 pairs of dual-wavelength (780 and 830 nm) laser diodes, which are used as light sources, and their outputs are amplitude-modulated at 140 MHz. For each source pair, the outputs from the two laser diodes at both wavelengths were coupled to the tissues through a 200-µm optical fiber. On the receiver side, eight photomultiplier tubes (PMTs) were used to detect diffusely scattered light from the tissues, and eight optical fibers (3 mm in diameter)

were used to couple detected diffusive light from the tissues to the PMTs. The high-frequency radiofrequency (RF) signals were amplified and heterodyned to 20 kHz. The heterodyned signals were further amplified and band pass–filtered at 20 kHz. A reference signal of 20 kHz was also generated by directly mixing the detected RF signals with the RF signal generated from the oscillator. The reference signal was necessary for retrieving phase shifts. Eight detection signals and one reference were sampled and acquired into the PC simultaneously. The entire data acquisition took about 3 to 4 seconds, which was fast enough for acquiring data from patients.

A picture of our combined probe and imaging system used in the reported clinical studies is shown in Figure 1*a*, and the probe configuration and optical sensor distribution are shown in Figure 1*b*. Both amplitude and phase at each source–detector pair are obtained and the resulting total number of measurements is $12 \times 8 \times 2 = 192$. The combined probe is made of a black plastic plate 10 cm in diameter; therefore, a semi-infinite boundary condition can be used for NIR measurement geometry. The amplitudes and phases acquired at all source–detector pairs at the normal contralateral breast were used to calculate the

(a)
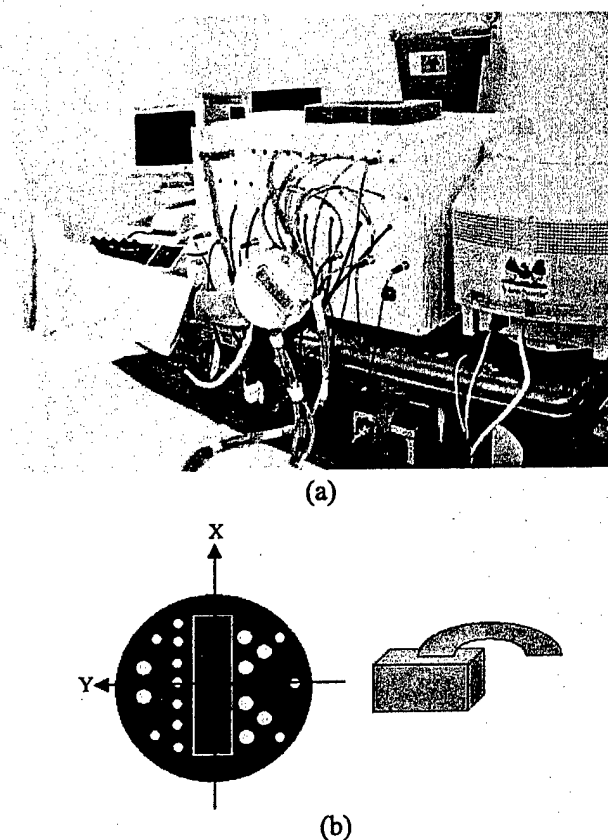
(b)

Figure 1. *(a) Picture of the combined probe and frequency domain imager. (b) Sensor distribution of the combined probe. Smaller circles in (b) are optical source fibers and big circles are detector fibers. A commercial ultrasound probe is located at the center of the combined probe, and the optical source and detector fibers are distributed at the periphery of the ultrasound probe.*

background absorption coefficient $\bar{\mu}_a$ and the reduced scattering coefficient $\bar{\mu}_s'$

The details of our dual-mesh optical imaging reconstruction algorithm have been described in Ref. [18]. Briefly, the entire tissue volume is segmented based on initial coregistered ultrasound measurements into a lesion region L and a background region B. A modified Born approximation is used to relate the scattered field $U_{sd}(r_{su}, r_{dt}, \omega)$ measured at the source (s) and detector (d) pair i to absorption variations $\Delta\mu_a$ (r') in each volume element of two regions within the sample. The matrix form of image reconstruction is given by:

$$[U_{sd}]_{M \times l} = [W_L, W_B]_{M \times N}[M_L, M_B]_{N \times 1}^{T}$$

where W_L and W_B are weight matrices for lesion and background regions, respectively; and $[M_L] = [\int_{1_L} \Delta\mu_a(r') d^3 r', \ldots \ldots \int_{N_L} \Delta\mu_a(r') d^3 r'$ and $[M_B] = [\int_{1_B} \Delta\mu_a(r') d^3 r', \ldots \ldots \int_{N_B} \Delta\mu_a(r') d^3 r')$ are total absorption distributions of lesion and background regions, respectively. The weight matrices are calculated based on the background $\bar{\mu}_a$ and $\bar{\mu}_s'$ measurements obtained from the normal contralateral breast.

Instead of reconstructing the $\Delta\mu_a$ distribution directly, as is done in the standard Born approximation, the total absorption distribution M is reconstructed and the total is divided by different voxel sizes of lesions and background tissues to obtain the $\Delta\mu_a$ distribution. By choosing a finer grid for lesion and a coarse grid for background tissues, we can maintain the total number of voxels with unknown absorption on the same scale of the total measurements. As a result, the inverse problem is less underdetermined. In addition, because the lesion absorption coefficient is higher than that of background tissues, in general, the total absorption of the lesion over a smaller voxel is on the same scale as the total absorption of the background over a bigger voxel. Therefore, the matrix $[M_L, M_B]$ is appropriately scaled for inversion. In all experiments, a finer grid of $0.5 \times 0.5 \times 0.5$ (cm^3) and a coarse grid of $1.5 \times 1.5 \times 1.5$ (cm^3) were chosen for the lesion region and the background tissues, respectively. The total reconstruction volume was chosen to be $9 \times 9 \times 4$ cm^3. The reconstruction is formulated as a least square problem and the unknown distribution M is iteratively calculated using the standard conjugate gradient method.

The perturbations for both wavelengths used to calculate absorption maps were normalized as $U_{sd}(r_{si}, r_{di}, \omega) = \frac{U_L(r_{si}, r_{di}, \omega) - U_N(r_{si}, r_{di}, \omega)}{U_N(r_{si}, r_{di}, \omega)} U_B(r_{si}, r_{di}, \omega)$, where $U_L(r_{si}, r_{di}, \omega)$ and U_N (r_{si}, r_{di}, ω) were optical measurements obtained at the lesion Mregion and the normal region of the contralateral breast, and $U_B(r_{si}, r_{di}, \omega)$ was the calculated incident field using the measured background. This procedure cancels the unknown system gains associated with different sources and detectors as well as electronic channels.

The commercial one-dimensional (1-D) ultrasound probe acquires two-dimensional (2-D) ultrasound images in the x–z plane (z is the propagation direction) and the 2-D NIR probe provides three-dimensional (3-D) optical measurements for 3-D image reconstruction. Therefore, at each location, a 2-D ultrasound image is coregistered with a corresponding set of 3-D optical measurements in the x–z plane. However, if we approximate a lesion as an ellipsoid, we are able to estimate its diameters from two orthogonal ultrasound images. The 3-D lesion center can be approximated from two orthogonal 2-D ultrasound images. However, two sources of error can affect accurate lesion location and volume estimation. First, the diameter measurements of large irregular lesions are inaccurate because lesion boundaries may not be well defined in ultrasound images. Second, the target boundaries seen by different modalities may be different due to different contrast mechanisms. To account for these errors, we use a lesion center estimated from the 2-D coregistered ultrasound image and use much larger diameters in both spatial dimensions than ultrasound-measured ones to highlight the lesion region for fine-mesh optical reconstruction. We have found from experiments that the abovementioned measurement inaccuracies have little effects on reconstructed optical properties as long as the lesion depth is measured correctly and the total number of unknown voxels is of the same order as the total number of measurements. The lesion depth z and the lesion boundaries in the z direction can be estimated reasonably well from 2-D coregistered ultrasound using normal tissue structure patterns.

Clinical studies were performed at the University of Connecticut Health Center (UCHC; Farmington, CT). The UCHC IRB committee approved the human subject protocol. Patients with palpable and nonpalpable masses that were visible on clinical ultrasound and who were scheduled for biopsy were enrolled as research subjects. These subjects were scanned with the combined probe, and ultrasound images and optical measurements were acquired at multiple locations including the lesion region scanned at two orthogonal positions, a normal region of the same breast if the breast was large, and a normal symmetric region of the contralateral breast also scanned at two orthogonal positions.

Results

Examples of Invasive Cancers

Figure 2a shows a gray scale ultrasound image of a nonpalpable lesion of a 55-year-old woman. The ultrasound showed a nodular mass with internal echoes and the lesion was considered suspicious. The estimated lesion diameter measured from two orthogonal ultrasound images was 8 mm. An ultrasound-guided core needle biopsy was recommended and the biopsy result revealed that the lesion was intraductal and infiltrating ductal carcinoma (nuclear grade II, histologic grade III). The cancer, once removed from the breast, measured 1 cm in greatest diameter, and was composed predominantly of invasive carcinoma (>95%), extending to surgical margins. Negative margins were achieved upon reexcision.

The average tissue background absorption coefficients $\bar{\mu}_a$ and the reduced scattering coefficients $\bar{\mu}_s'$ at 780 and 830 nm were measured as $\mu_a^{780} = 0.02$ cm^{-1}, $\mu_s'^{780} = 8.2$ cm^{-1}, $\mu_a^{830} = 0.04$ cm^{-1}, and $\mu_s'^{830} = 6.0$ cm^{-1}, respectively. The initial estimates of the lesion center and the
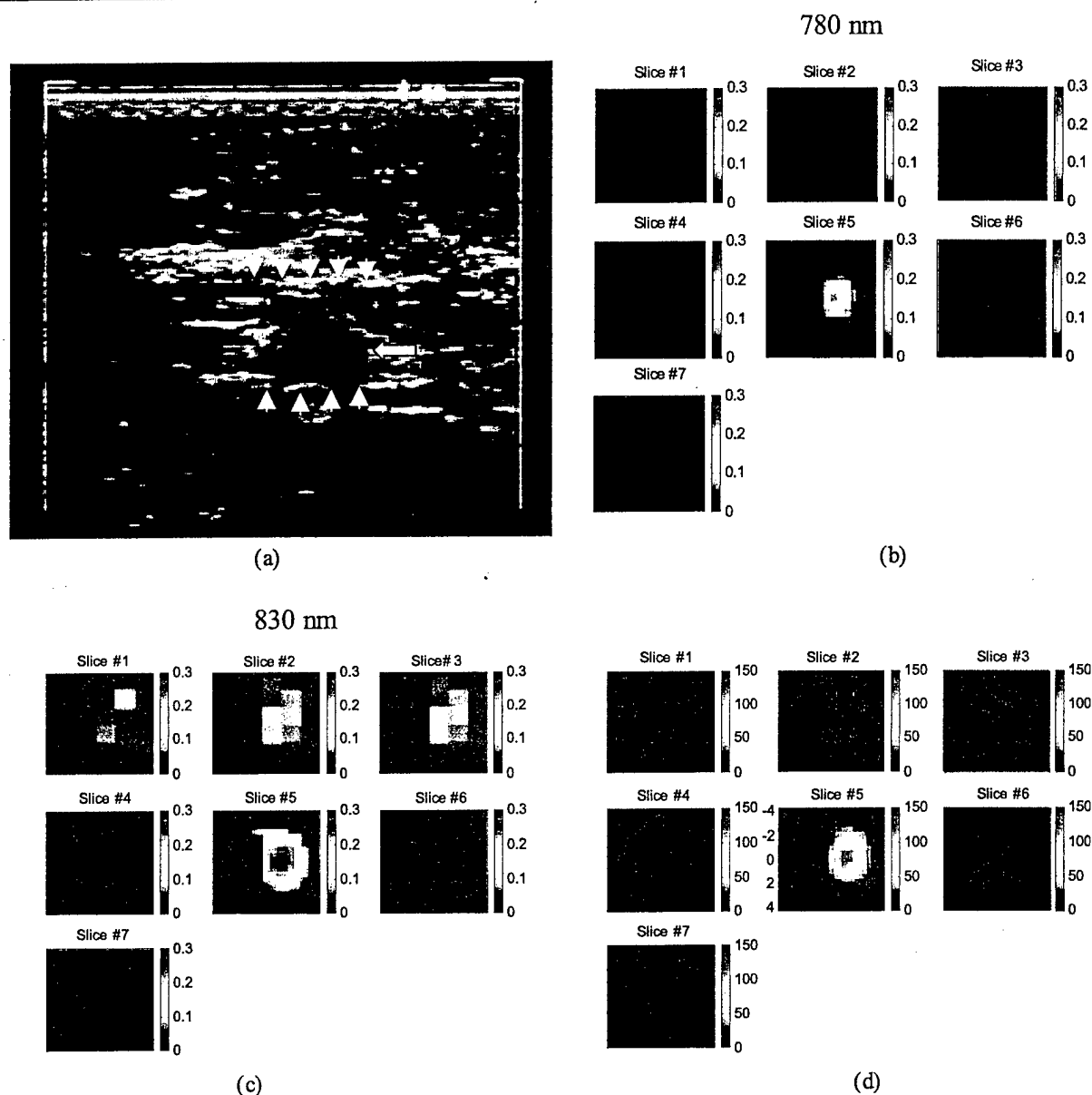
780 nm

(a)

(b)

830 nm

(c)

(d)

Figure 2. *(a) shows a gray scale ultrasound image of a nonpalpable lesion of a 55-year-old woman. The lesion pointed by the arrow was located at the 4 o'clock position of the right breast measuring 8 mm in diameter. Ultrasound showed nodular mass with internal echoes and the lesion was considered suspicious. (b) and (c) are optical absorption maps at 780 and 830 nm, respectively. x and y axes are spatial dimensions of 9 × 9 cm. The slices starting from left to right correspond to absorption maps from 0.7 cm underneath the skin surface to the chest wall in 0.5-cm spacing. (d) is the total hemoglobin concentration and the vertical scale is in micromoles.*

diameter from coregistered ultrasound were (0, 0.3, 2.3) cm and 8 mm. To account for errors in lesion geometry estimate and for differences in optical contrast, we used a 6-cm diameter in both x and y spatial dimensions at the center of (0, 0.3, 2.3) cm for fine-mesh optical reconstruction. The lesion diameter in depth is estimated as 1 cm by comparing the top and the bottom of lesion boundaries from normal tissue patterns. The white arrow arrays on the top and bottom of the lesion in Figure 2a point to normal tissue boundaries.

The optical absorption maps at both wavelengths are shown in Figure 2, *b* and *c*, respectively. In both Figure 2, *b* and *c*, the first slice is 0.7 cm deep into the breast tissue from the skin surface and the last slice is closer to the chest

wall. The spacing of the slices is 0.5 cm. The horizontal and vertical axes of each slice are spatial x and y dimensions of 9 cm in size. The lesion is well resolved in slice 5 and has shown much larger spatial extension at 830 nm than that at 780 nm. The measured maximum absorption coefficients are $\mu_a^{780} = 0.24$ cm^{-1} and $\mu_a^{830} = 0.28$ cm^{-1}, respectively, and the absorption maxima at both wavelengths are located at (0, 1.0, 2.3) cm, which is close to the lesion center measured by ultrasound.

By assuming that the major chromophores are oxygenated (oxyHb) and deoxygenated (deoxyHb) hemoglobin molecules in the wavelength range studied, we can estimate the distribution of total hemoglobin concentration as

shown in Figure 2d. The extinction coefficients used for calculating oxyHb and deoxyHb concentrations were ε_{Hb}^{780} = 2.54, $\varepsilon_{HbO_2}^{780}$ = 1.70, ε_{Hb}^{830} = 1.80, $\varepsilon_{HbO_2}^{830}$ = 2.42, obtained from Ref. [19] in a natural logarithm scale with units of inverse millimoles times inverse centimeters. The measured maximum total hemoglobin concentration for lesions is 122 μmol, and the measured average background hemoglobin concentration is 14 μmol. The spatial extent of the lesion's angiogenesis is measured from the full width at half maximum (FWHM) of the total hemoglobin map and it is estimated to be 2.0 cm. This number is about two and half times larger than the 8 mm diameter measured by ultrasound and suggests that optical contrasts extend well beyond the cancer periphery due to angiogenesis.
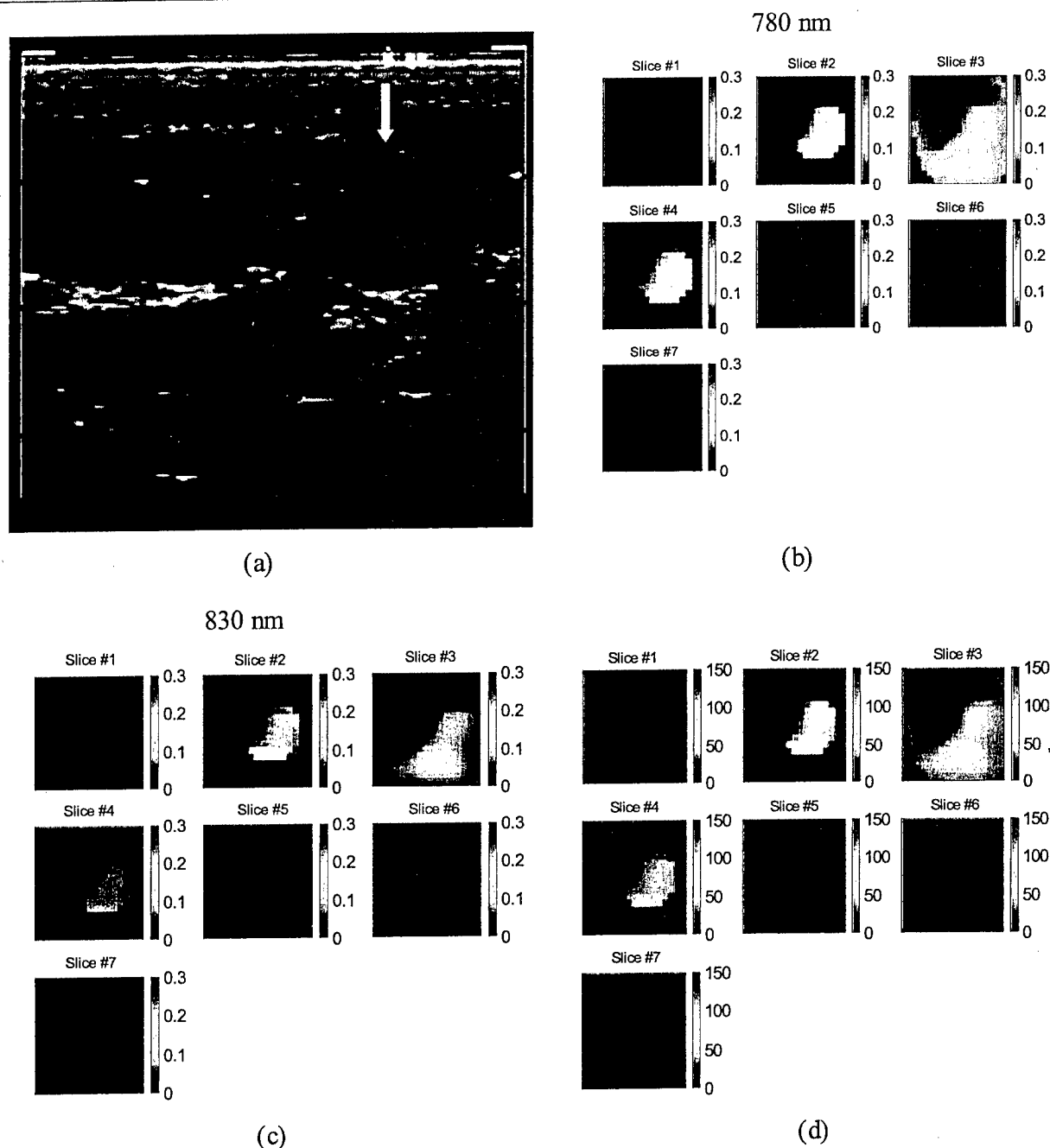
Because our hand-held probe can be easily rotated or translated, we have acquired at least three coregistered ultrasound and NIR data sets at the lesion location for each patient and have reconstructed corresponding optical absorption maps as well as the total hemoglobin concentration distribution under the coregistered ultrasound guidance. The average maximum total hemoglobin concentration at the cancer region is 115 μmol (±27.6 μmol) and the average background total hemoglobin concentration is 13 μmol (±1.5 μmol). The large standard deviation at the cancer region is likely related to the probe compression at different spatial locations and elastic properties of the blood vessels in the cancer region.

Another example was obtained from a 56-year-old woman who had a solid mass with internal ultrasound echoes measuring 9 mm in size (Figure 3a). The lesion was considered suspicious, and ultrasound-guided core needle biopsy revealed that the lesion was *in situ* and

(a)

780 nm

(b)

830 nm

(c)

(d)
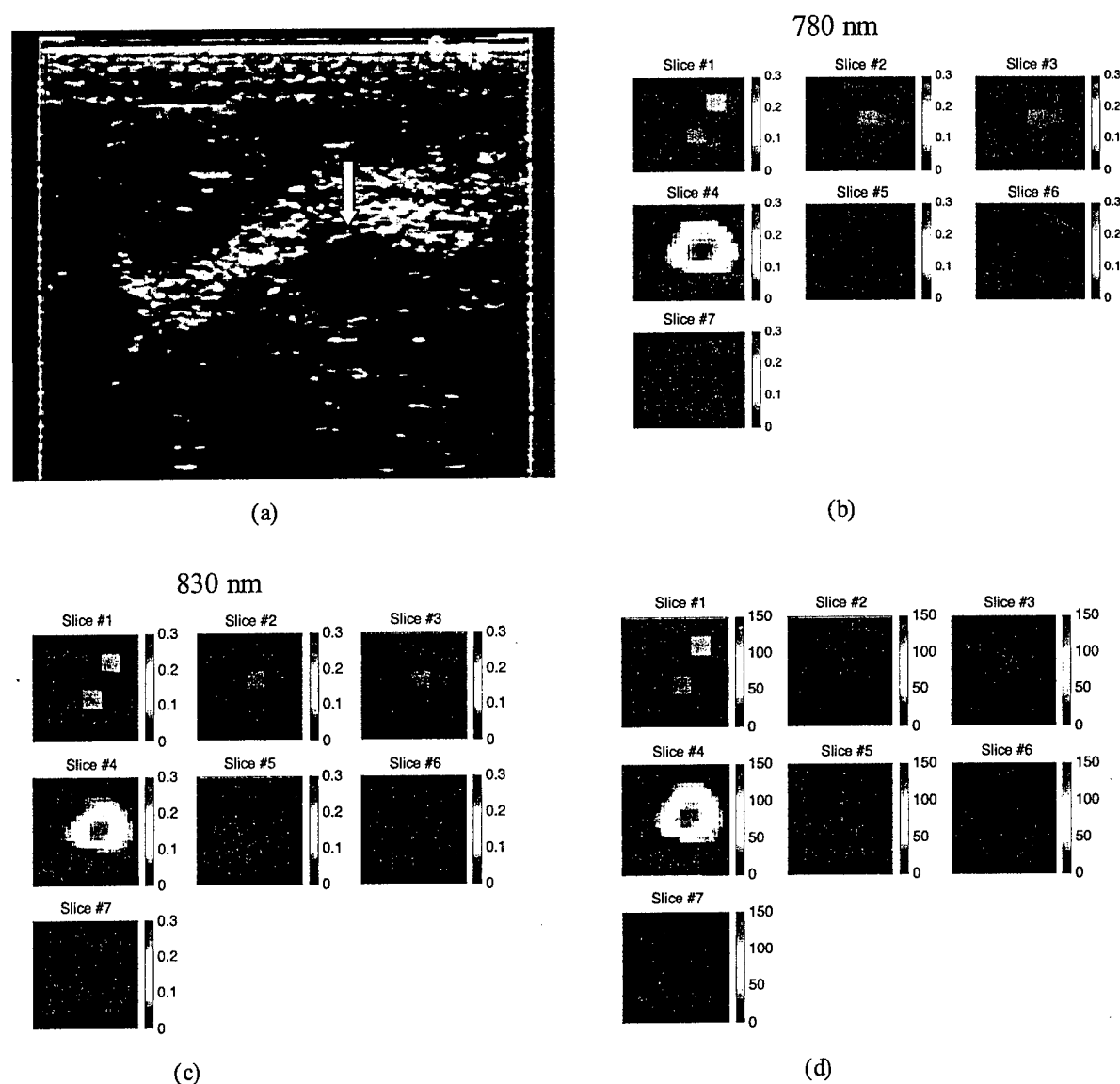
Figure 3. *This example was obtained from a 56-year-old woman who had nonpalpable lesion located at the 10 o'clock position of the left breast. Ultrasound showed a solid mass (a) with internal echoes measuring 9 mm in size and the lesion was considered suspicious. (b) and (c) are optical absorption maps at 780 and 830 nm, respectively. The slices start from 0.4 cm underneath the skin surface to the chest wall in 0.5-cm spacing. (d) is the total hemoglobin concentration.*

780 nm

Slice #1 0.3 0.2 0.1 0
Slice #2 0.3 0.2 0.1 0
Slice #3 0.3 0.2 0.1 0
Slice #4 0.3 0.2 0.1 0
Slice #5 0.3 0.2 0.1 0
Slice #6 0.3 0.2 0.1 0
Slice #7 0.3 0.2 0.1 0

(a)

(b)

830 nm

Slice #1 0.3 0.2 0.1 0
Slice #2 0.3 0.2 0.1 0
Slice #3 0.3 0.2 0.1 0
Slice #4 0.3 0.2 0.1 0
Slice #5 0.3 0.2 0.1 0
Slice #6 0.3 0.2 0.1 0
Slice #7 0.3 0.2 0.1 0

Slice #1 150 100 50 0
Slice #2 150 100 50 0
Slice #3 150 100 50 0
Slice #4 150 100 50 0
Slice #5 150 100 50 0
Slice #6 150 100 50 0
Slice #7 150 100 50 0

(c)

(d)

Figure 4. (a) shows a solid lesion at the 2 o'clock position measuring 1.1 cm in diameter in ultrasound image. The lesion was diagnosed as having benign appearance because of well-defined boundaries. Ultrasound-guided core biopsy revealed scattered foci of lobular neoplasia, carcinoma in situ but not invasive, and fibroadenoma and fibrocystic changes with associated microcalcifications. (b) and (c) are optical absorption maps at 780 and 830 nm, respectively. The slices start from 0.5 cm underneath the skin surface to the chest wall in 0.5-cm spacing. (d) is the total hemoglobin concentration.

invasive ductal carcinoma (nuclear grade II, histologic grade II). The tumor, once removed from the breast, measured 1.5 cm in greatest diameter, and was composed predominantly of invasive carcinoma (>80%), extending to the inferior/anterior surgical margin. Negative inferior margin was achieved upon reexcision.

The average tissue background absorption coefficient $\bar{\mu}_a$ and the reduced scattering coefficient $\bar{\mu}'_s$ at 780 and 830 nm were measured as $\mu_a^{780} = 0.04$ cm^{-1}, $\mu_s'^{830} = 4.7$ cm^{-1}, $\mu_a^{780} = 0.03$ cm^{-1}, and $\mu_a'^{830} = 5.8$ cm^{-1}, respectively. The initial

estimate of the lesion center and diameters from coregistered ultrasound were (0, 0.6, 1.9) cm and 9 mm, respectively. Again, we used a 6-cm diameter in both x and y spatial dimensions at the center of (0, 0.6, 1.9) for fine-mesh optical reconstruction. The optical absorption maps at both wavelengths are shown in Figure 3, b and c, respectively. In Figure 3, b and c, the first slice is 0.4 cm deep into the breast tissues from the skin surface and the last slice is closer to the chest wall. The spacing between the slices is 0.5 cm. This lesion is well resolved in slice #4 and has shown much larger

BEST AVAILABLE COPY

spatial extension at 780 nm than that at 830 nm. The measured maximum absorption coefficients are $\mu_a^{780} = 0.29$ cm^{-1} and $\mu_a^{830} = 0.25$ cm^{-1}, respectively. The absorption maxima at both wavelengths are located at (0 1.0 1.9000) cm, which is very close to the lesion center measured by ultrasound. The calculated maximum total hemoglobin concentration of the lesion is 128 μmol, and the background concentration is 24 μmol. The measured FWHM of the total hemoglobin map is 3.5 cm, which is more than three times larger than the 9 mm diameter measured by ultrasound and again suggests that optical contrasts extend well beyond the cancer periphery due to angiogenesis. The average maxi-

mum total hemoglobin concentration calculated from three NIR data sets is 123 μmol (±6.2 μmol) and the average background hemoglobin concentration is 24 μmol (±0.5 μmol). The variation of total hemoglobin concentrations acquired at slightly different spatial probe positions is much smaller than that in the previous case.

An Example of Combined Fibroadenoma and Fibrocystic Changes with Scattered Foci of Lobular Neoplasia/Lobular Carcinoma In Situ (Noninvasive Carcinoma)

This patient had a solid lesion measuring 1.1 cm in diameter as shown in Figure 4a ultrasound image. The lesion

(a)

(b)

(c)

(d)
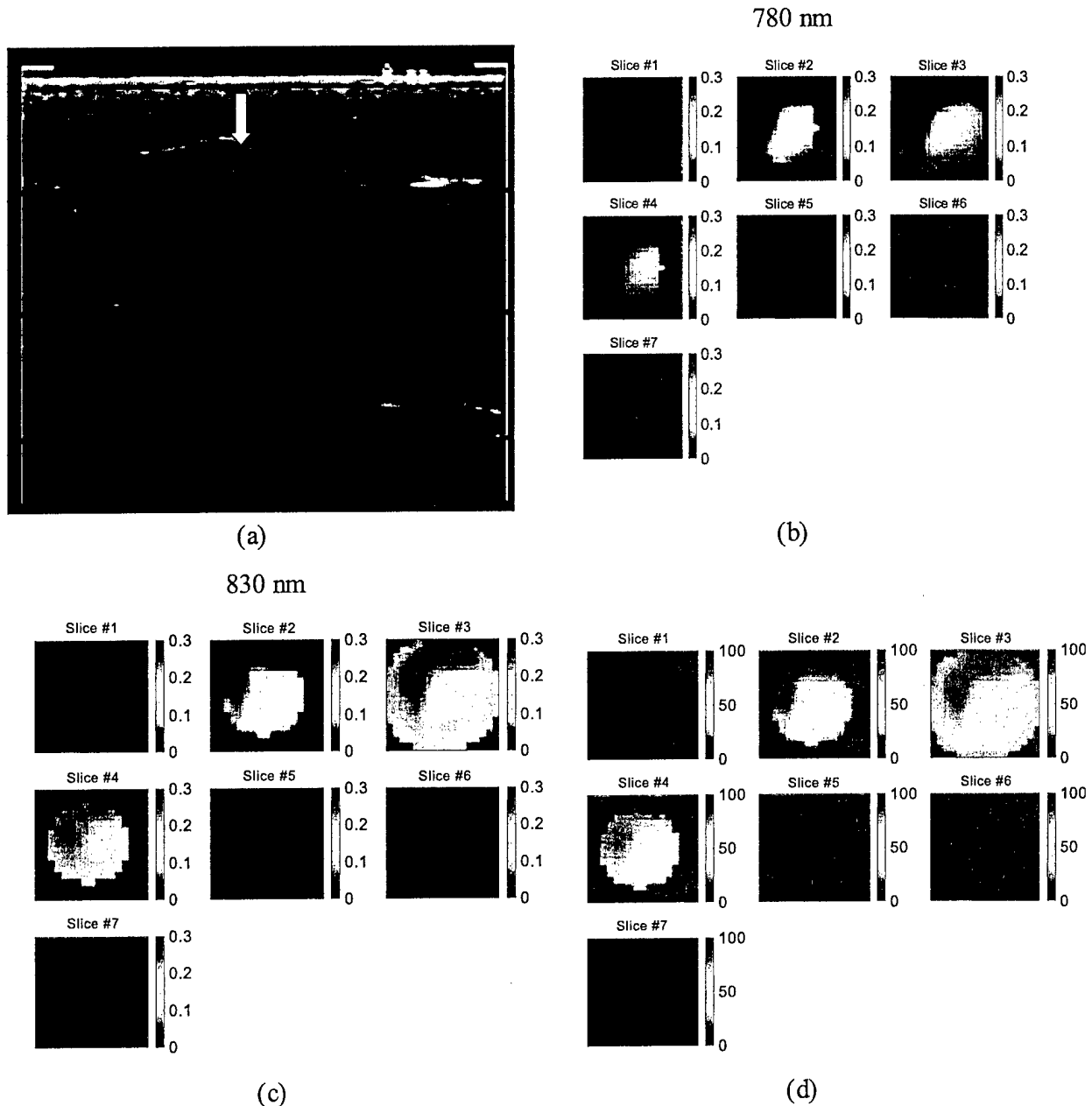
Figure 5. *(a) shows an ultrasound image of a solid hypoechogenic lesion located at 9 to 10 o'clock position of a 37-year-old woman's breast. The diagnosis was that the lesion could represent fibroadenoma; however, there was a chance that the lesion could be a carcinoma because of the irregular shape and posterior shadow seen by ultrasound. (b) and (c) are optical absorption maps at 780 and 830 nm, respectively. The slices start from 0.5 cm underneath the skin surface to the chest wall in 0.5-cm spacing. (d) is the total hemoglobin concentration.*

Table 1. Measured Parameters of 19 Cases.

Reference Number	Biopsy Results	Lesion Size (Ultrasound) [cm]	ROI	FWHM (NIR) [cm]	Max μ_a [cm^{-1}], 780 nm	Max μ_a [cm^{-1}], 830 nm	Max Total Hb [μM]	Average Total Hb [μM]
13	Invasive cancer	0.9 × 0.6	6 × 6 × 1	3.5	0.28	0.24	123	87
			10 × 10 × 1	3.5	0.27	0.24	122	88
25	Invasive cancer	0.8 × 0.5	6 × 6 × 1	2.0	0.22	0.26	115	84
			10 × 10 × 1	2.1	0.22	0.26	115	84
32	Fibrocystic and lobular neoplasia/carcinoma	1.1 × 1.1	10 × 10 × 1.2	6.1	0.12	0.08	48	30
11	Fibroadenoma	1.2 × 0.8	8 × 8 × 1	4.9	0.11	0.10	49	37
8	Fibroadenoma	2.2 × 1.3	8 × 8 × 1.6	2.7	0.07	0.03	24	16
9	Fibroadenoma	0.9 × 0.7	8 × 8 × 1	4.9	0.15	0.18	77	52
7	Fibroadenoma and sclerosing adenosis with extensive calcification	1.0 × 0.6	10 × 10 × 1	3.8	0.16	0.11	59	41
17	Fibrocystic changes	0.6 × 0.7	10 × 10 × 1	5.8	0.16	0.16	76	53
20	Fibroadenoma	1.2 × 0.6	10 × 10 × 1	5.7	0.14	0.14	67	45
30	1: Fibrocystic change	1.7 × 1.1	8 × 8 × 1.3	4.0	0.10	0.15	59	39
30	2: Sclerosing adenosis and epithelial hyperplasia without atypical	1.4 × 1.2	8 × 8 × 1.3	4.0	0.15	0.23	88	57
22	Fibroadenoma	1.0*	10 × 10 × 1.5	3.7	0.15	0.15	72	46
36	Fibroadenoma	1.9 × 0.9	9 × 9 × 1	4.7	0.13	0.18	73	50
28	Fibroadenoma	1.9 × 1.1	9 × 9 × 1.3		0.14	0.16	71	45
33	Fibroadenoma	1.2 × 0.7	10 × 10 × 1	7.0	0.13	0.13	61	44
37	Fibroadenoma	0.8 × 0.6	8 × 8 × 1	6.0	0.16	0.18	80	53
35	Fibroadenoma	1.3 × 1.3	9 × 9 × 2	4.3	0.14	0.15	59	41
38	Hyalinized fibroadenoma	0.8 × 0.4	6 × 6 × 1	2.5	0.17	0.22	90	67
29	Atypical ductal hyperplasia	1.1 × 0.8	9 × 9 × 1	3.7	0.10	0.17	64	44

*See by X-ray.

was diagnosed as having a benign appearance; however, the biopsy result revealed combined fibrocystic changes associated with microcalcifications and scattered foci of lobular neoplasia/lobular carcinoma *in situ* with pagetoid extension along ducts, but no invasive carcinoma. Also present was a fibroadenoma involved by lobular neoplasia.
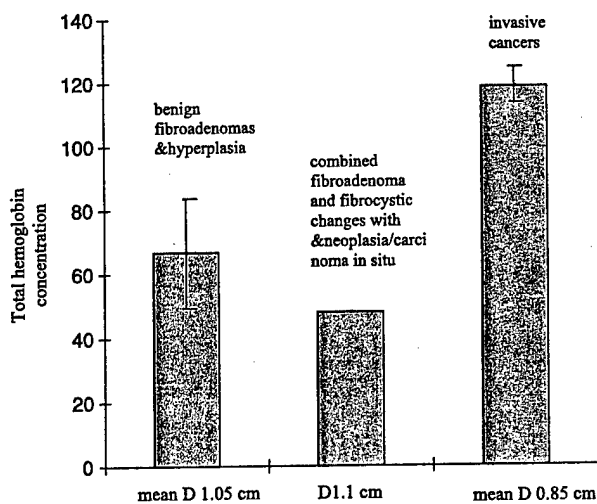
Figure 6. *The average maximum total hemoglobin concentration obtained from benign fibroadenomas and hyperplasia, and combined fibroadenoma and fibrocystic change with neoplasia/carcinoma in situ (noninvasive) and invasive cancer groups are shown in bars. The standard deviations of three groups are also provided. The average sizes of lesions of the three groups are 1.05 (0.3), 1.1, and 0.9 (0.07) cm, respectively.*

The average background tissue absorption coefficients and reduced scattering coefficients at both wavelengths were measured as $\mu_a^{780} = 0.04$ cm^{-1}, $\mu_s'^{780} = 3.3$ cm^{-1}, $\mu_a^{830} = 0.02$ cm^{-1}, and $\mu_s'^{830} = 3.5$ cm^{-1}, respectively. The initial estimate of the lesion center and the diameter from ultrasound were (0, 0.9, 1.4) and 1.1 cm. The reconstructed absorption maps as well as total hemoglobin concentration distribution are shown in Figure 4, *b–d*, respectively. The measured maximum absorption coefficients are $\mu_a^{780} = 0.13$ cm^{-1} and $\mu_a^{830} = 0.09$ cm^{-1}, respectively, which are about half of those measured in invasive cancer cases. In addition, the absorption coefficient distributions are diffused at both wavelengths and no resolvable or localized lesions are seen. The calculated maximum total hemoglobin concentration is 53 μmol, which is less than half of those in invasive cancer cases. The calculated background value is 13 μmol. The average maximum hemoglobin concentration calculated from four reconstructed NIR images at lesion location is 48 μmol (±2.8 μmol) and the value for the background is 12 μmol (±0.4 μmol). This example suggests that tumor vascularization may not be developed at the early noninvasive stage of combined fibrocystic change and neoplasia/carcinoma *in situ*.

Example of Fibroadenoma and Other Benign Lesions

Figure 5*a* shows an ultrasound image of a hypoechoic mass of a 37-year-old woman. The diagnosis was that the lesion likely was a fibroadenoma; however, there was

concern that the lesion could be a carcinoma because of the irregular shape and the posterior shadowing seen by ultrasound. An ultrasound-guided core breast biopsy revealed that the lesion was simply a fibroadenoma.

Optical absorption maps are shown in Figure 5, b and c, as well as the total hemoglobin distribution in Figure 5d. Compared with the invasive cancer cases, the spatial distributions of the absorption coefficients as well as the total hemoglobin concentration are quite diffused, and a higher absorption region at 830 nm corresponds to lesion regions seen by ultrasound. The measured maximum lesion absorption coefficients at 780 and 830 nm are $\mu_a^{780}=0.10$ cm^{-1} and $\mu_a^{830}=0.12$ cm^{-1}, respectively, and these values are less than half of those small invasive cancer cases. The calculated maximum total hemoglobin concentration is 52 μmol and the background hemoglobin concentration is 14 μmol. The calculated average maximum total hemoglobin concentration from four NIR images acquired at lesion region is 59 μmol (±5.1 μmol) and the average background is 16 μmol (±1.0 μmol).

Table 1 lists all the measured parameters of the 19 cases [from left to right: biopsy result, lesion size measured by ultrasound in x and z dimensions (because lesions are small, the lesion size in y is similar to that measured in the x dimension), region of interest (ROI) used for fine-mesh NIR imaging, FWHM measured from NIR imaging, maximum absorption coefficients measured at both wavelengths, maximum and average total hemoglobin concentrations (the average is computed within FWHM)]. For the two invasive cancer cases, NIR parameters are given for two different ROIs and the results show that the choice of ROI has negligible effects on the absorption and hemoglobin measurements.

The statistics of maximum total hemoglobin concentration of three groups obtained from the 19 cases are shown in Figure 6. The benign group of fibroadenoma (15 cases) and hyperplasia (1 case) has an average of 67 μmol (±17.0 μmol), the combined fibroadenoma and fibrocystic change with noninvasive neoplasia/carcinoma *in situ* case has a maximum of 48 μmol, and the invasive cancer group of two cases has shown about two-fold greater average of 119 μmol (±1.6 μmol). If average total hemoglobin concentration is used, the values are 46 (±11.3), 30, and 86 (±2.12) μmol for the three corresponding groups, respectively. The malignant group also presents about two-fold greater average hemoglobin concentration than that of the benign group. The average sizes of lesions of the three groups measured by ultrasound are 1.05 (±0.3), 1.1, and 0.9 (±0.07) cm, respectively. The lesion size is the geometric mean of diameters measured in x and z dimensions.

Because our study is in its early clinical trial stage, we do not intend to provide the sensitivity and specificity of the combined method due to the limited sample size available. However, our initial findings are very encouraging and suggest that early-stage small invasive cancers have much higher optical contrast than benign lesions and could be diagnosed with high specificity possibly due to tumor angiogenesis.

Discussion

As described earlier, due to intense light scattering, optical tomography alone has not been widely used in clinical studies. Data in the published literature have been limited to feasibility studies or case reports. Pogue et al. [9] reported pilot results of one invasive ductal carcinoma 1 cm in size and one benign fibroadenoma 3 cm in size. The reported maximum total hemoglobin concentrations were 68 μmol for the cancer case and 55 μmol for the benign case. Although the invasive cancer size reported by this group is comparable to ours, the system they used can only acquire NIR data from a ring area with optical sources and detectors deployed around the breast (2-D imager). Therefore, incomplete information could lead to smaller reconstructed absorption coefficients and total hemoglobin concentrations than those reported here using our 3-D NIR imager. In addition, an investigation with phantoms has shown that NIR alone, in general, reconstructs lower absorption coefficients and therefore lower total hemoglobin concentrations than true values [20]. This can be seen from two studies of the same data reported in Refs. [7,13]. Authors in Ref. [7] reported an average of 35 μmol total hemoglobin concentration of a 2-cm ductal carcinoma *in situ* by using NIR measurements alone. After reprocessing the same NIR measurement data using an approximate lesion depth obtained from a separate ultrasound image, the authors reported that the calculated average total hemoglobin concentration was increased to 67 μmol [13].

The reported small early-stage invasive cancers appear isolated and are well resolved from background tissues in optical absorption maps as well as in total hemoglobin distributions. However, the combined fibroadenoma and fibrocystic change with scattered foci of lobular neoplasia/lobular carcinoma *in situ* case showed no difference in optical absorption and hemoglobin concentration than those obtained from fibroadenoma cases. This suggests that optical tomography may not be sensitive to early-stage mixed benign changes and noninvasive neoplasia/carcinoma *in situ* because tumor neovascularization has not been developed. This result is consistent with magnetic resonance imaging (MRI) findings on the low detection sensitivity of carcinoma *in situ* [21–23]. However, optical imaging may be a valuable tool for monitoring the development or transition of lesions from noninvasive to early invasive stage. Certainly, more cases are needed to validate the observations reported here. For larger cancers, highly heterogeneous wavelength-dependent optical absorption distributions and total hemoglobin distribution have been observed in four cases [18], and these distributions could provide valuable information for monitoring and assessing cancer therapy under treatment. Currently, we are pursuing research along this line and more cases will be reported in the future.

In principle, the distribution of oxygenation saturation can be estimated as $S = oxyHb/(oxyHb+deoxyHb)$, with deoxyHb and oxyHb distributions calculated from absorption maps at the two wavelengths of 780 and 830 nm. However, because background tissues mainly consist of water and lipid and these two chromophores contribute to the total

concern that the lesion could be a carcinoma because of the irregular shape and the posterior shadowing seen by ultrasound. An ultrasound-guided core breast biopsy revealed that the lesion was simply a fibroadenoma.

Optical absorption maps are shown in Figure 5, *b* and *c*, as well as the total hemoglobin distribution in Figure 5*d*. Compared with the invasive cancer cases, the spatial distributions of the absorption coefficients as well as the total hemoglobin concentration are quite diffused, and a higher absorption region at 830 nm corresponds to lesion regions seen by ultrasound. The measured maximum lesion absorption coefficients at 780 and 830 nm are μ_a^{780}=0.10 cm^{-1} and μ_a^{830}=0.12 cm^{-1}, respectively, and these values are less than half of those small invasive cancer cases. The calculated maximum total hemoglobin concentration is 52 μmol and the background hemoglobin concentration is 14 μmol. The calculated average maximum total hemoglobin concentration from four NIR images acquired at lesion region is 59 μmol ($\pm$5.1 μmol) and the average background is 16 μmol ($\pm$1.0 μmol).

Table 1 lists all the measured parameters of the 19 cases [from left to right: biopsy result, lesion size measured by ultrasound in *x* and *z* dimensions (because lesions are small, the lesion size in *y* is similar to that measured in the *x* dimension), region of interest (ROI) used for fine-mesh NIR imaging, FWHM measured from NIR imaging, maximum absorption coefficients measured at both wavelengths, maximum and average total hemoglobin concentrations (the average is computed within FWHM)]. For the two invasive cancer cases, NIR parameters are given for two different ROIs and the results show that the choice of ROI has negligible effects on the absorption and hemoglobin measurements.

The statistics of maximum total hemoglobin concentration of three groups obtained from the 19 cases are shown in Figure 6. The benign group of fibroadenoma (15 cases) and hyperplasia (1 case) has an average of 67 μmol ($\pm$17.0 μmol), the combined fibroadenoma and fibrocystic change with noninvasive neoplasia/carcinoma *in situ* case has a maximum of 48 μmol, and the invasive cancer group of two cases has shown about two-fold greater average of 119 μmol ($\pm$1.6 μmol). If average total hemoglobin concentration is used, the values are 46 ($\pm$11.3), 30, and 86 ($\pm$2.12) μmol for the three corresponding groups, respectively. The malignant group also presents about two-fold greater average hemoglobin concentration than that of the benign group. The average sizes of lesions of the three groups measured by ultrasound are 1.05 ($\pm$0.3), 1.1, and 0.9 ($\pm$0.07) cm, respectively. The lesion size is the geometric mean of diameters measured in *x* and *z* dimensions.

Because our study is in its early clinical trial stage, we do not intend to provide the sensitivity and specificity of the combined method due to the limited sample size available. However, our initial findings are very encouraging and suggest that early-stage small invasive cancers have much higher optical contrast than benign lesions and could be diagnosed with high specificity possibly due to tumor angiogenesis.

Discussion

As described earlier, due to intense light scattering, optical tomography alone has not been widely used in clinical studies. Data in the published literature have been limited to feasibility studies or case reports. Pogue et al. [9] reported pilot results of one invasive ductal carcinoma 1 cm in size and one benign fibroadenoma 3 cm in size. The reported maximum total hemoglobin concentrations were 68 μmol for the cancer case and 55 μmol for the benign case. Although the invasive cancer size reported by this group is comparable to ours, the system they used can only acquire NIR data from a ring area with optical sources and detectors deployed around the breast (2-D imager). Therefore, incomplete information could lead to smaller reconstructed absorption coefficients and total hemoglobin concentrations than those reported here using our 3-D NIR imager. In addition, an investigation with phantoms has shown that NIR alone, in general, reconstructs lower absorption coefficients and therefore lower total hemoglobin concentrations than true values [20]. This can be seen from two studies of the same data reported in Refs. [7,13]. Authors in Ref. [7] reported an average of 35 μmol total hemoglobin concentration of a 2-cm ductal carcinoma *in situ* by using NIR measurements alone. After reprocessing the same NIR measurement data using an approximate lesion depth obtained from a separate ultrasound image, the authors reported that the calculated average total hemoglobin concentration was increased to 67 μmol [13].

The reported small early-stage invasive cancers appear isolated and are well resolved from background tissues in optical absorption maps as well as in total hemoglobin distributions. However, the combined fibroadenoma and fibrocystic change with scattered foci of lobular neoplasia/lobular carcinoma *in situ* case showed no difference in optical absorption and hemoglobin concentration than those obtained from fibroadenoma cases. This suggests that optical tomography may not be sensitive to early-stage mixed benign changes and noninvasive neoplasia/carcinoma *in situ* because tumor neovascularization has not been developed. This result is consistent with magnetic resonance imaging (MRI) findings on the low detection sensitivity of carcinoma *in situ* [21–23]. However, optical imaging may be a valuable tool for monitoring the development or transition of lesions from noninvasive to early invasive stage. Certainly, more cases are needed to validate the observations reported here. For larger cancers, highly heterogeneous wavelength-dependent optical absorption distributions and total hemoglobin distribution have been observed in four cases [18], and these distributions could provide valuable information for monitoring and assessing cancer therapy under treatment. Currently, we are pursuing research along this line and more cases will be reported in the future.

In principle, the distribution of oxygenation saturation can be estimated as S = oxyHb/(oxyHb+deoxyHb), with deoxyHb and oxyHb distributions calculated from absorption maps at the two wavelengths of 780 and 830 nm. However, because background tissues mainly consist of water and lipid and these two chromophores contribute to the total

absorption estimate as well, we could not obtain reasonable background oxygenation saturation and compare it with lesion oxygenation saturation. Recently, we have improved our NIR system by adding another wavelength at 660 nm, which may allow us to accurately estimate the background oxygenation saturation and to compare it with lesion oxygenation saturation.

If we reconstruct the lesion area only, we could distribute partial perturbations caused by background to lesion and increase calculated lesion absorption and therefore hemoglobin concentration. However, with the dual-mesh scheme, we reconstruct the entire imaging volume instead of the lesion area only, and distribute the perturbations to both lesion and background. We did phantom experiments using the dual-mesh scheme and obtained absorption coefficients, which were always within 10% of the true values depending on the phantom contrasts [24].

Two-dimensional ultrasound provides fine tissue layer structures in depth (z) direction (Figure 2, *arrow arrays*), and the 2-D ultrasound image is coregistered with optical data in z. Therefore, we only need to consider possible angiogenesis extensions in z and we have extended the lesions to the closest normal tissue lines in z. In spatial dimensions, we have some uncertainty in another dimension (y) based on 2-D $x–z$ ultrasound image, and we need to extend the lesion region to a larger area to account for this as well as for possible angiogenesis extension.

The reported optical tomography study was used to image and characterize ultrasonically detected lesions. However, in one benign fibroadenoma case, the lesion was not visible in ultrasound but was seen by conventional X-ray mammogram. By knowing the approximate lesion region with respect to the nipple location from the patient's mammogram, we used a fine mesh for optical reconstruction in a larger region of $9 \times 9 \times 1.5$ cm^3, and identified a possible lesion that showed slightly higher optical absorption than that of the background. We believe that optical tomography, assisted by conventional mammography and/or ultrasound localization, has potential as a screening tool to identify and characterize malignancy.

Our initial findings provide evidence that optical tomography, combined with ultrasound, could be used to differentiate early-stage small invasive breast cancers from benign lesions. Because of the limited sample size available, we are not able to provide sensitivity and specificity results in this paper. In addition, for the patients studied, four fibroadenoma cases and one intraductal hyperplasia were excluded from the statistics shown in Figure 6. The four fibroadenoma cases were scanned at the beginning of the study. One patient was scanned after core biopsy due to scheduling problem, and the possible blood distribution change due to biopsy procedure has to be considered. The other three young patients have small and dense breasts. For these three patients, the optical amplitude and phase data sets were highly scattered even in the normal contralateral breast. Therefore, no reliable background tissue absorption and scattering coefficients can be obtained. Three possible sources for these findings were identified.

First, because these breasts were small and dense, the skin and probe contact was not always good. Second, a thick gel layer used for coupling the ultrasound transducer with the skin can serve as a light tunneling medium from sources to detectors. This portion of the light can saturate the detectors and give false readings. Caution was taken in the later studies by compressing the probe harder against the examined breast to ensure good probe–tissue contact, and by placing a very thin gel layer underneath the ultrasound transducer during scanning. The third source are tissue heterogeneities of the young dense breasts. However, by carefully removing outliers from normal breast data, we could obtain reasonably good reference data for imaging. One patient with intraductal hyperplasia data was excluded from the study. This patient had a solid lesion located at the nipple area and the nipple had a very dark color. Four NIR image data sets obtained at the lesion area had the same artifacts and the artifact consistently showed up with very high absorptions at both wavelengths. When the lesion locations were changed in different images with different probe positions, the artifact location changed very little. A similar artifact showed up in the two reference data sets acquired in the contralateral normal breast. We do not know the exact source of this artifact because there was no report that this patient had problems at the contralateral breast. Care was taken in the later studies by acquiring at least four reference data sets at the normal symmetric region of the contralateral breast, as well as at normal regions of the same lesion breast. Reference data sets were always checked for normal background absorption changes before imaging the lesions.

Summary

Initial clinical results from the use of optical tomography combined with conventional ultrasound demonstrate that there is a huge optical contrast between early-stage invasive cancers and benign solid lesions due to angiogenesis. An average of 52 μmol difference was obtained between two small invasive cancers and a group of 16 benign solid lesions. In addition, the small invasive cancers were localized well in absorption maps and have shown wavelength-dependent absorption changes, whereas the benign lesions appeared more diffused in absorption maps and have shown relatively wavelength-independent absorption changes. The combined fibrocystic changes and noninvasive neoplasia/ carcinoma *in situ* case did not show a significant difference in optical absorption and total hemoglobin concentration than those of benign lesions. This suggests that the angiogenesis may not be developed at the early noninvasive stage of the mixed benign changes and fibroadenoma with neoplasia/ carcinoma *in situ*. However, optical tomography may have a potential role in monitoring the development and/or transition of cancers from the noninvasive to the invasive stage.

Our reported initial results are very encouraging and demonstrate that our unique approach, which combines optical tomography with ultrasound, has great potential to detect and characterize breast lesions.

References

[1] Stavros TA, Thickman D, and Rapp C (1995). Solid breast nodules: use of sonography to distinguish between benign and malignant lesions. *Radiology* **196**, 123–34.

[2] Sickles EA (1998). Detection and diagnosis of breast cancer with mammography. *Perspect Radiol* **1**, 36–65.

[3] Rahbar G, Sie AC, Hansen GC, Prince JS, Melany ML, Reynolds H, Jackson VP, Sayre JW, and Bassett LW (1999). Benign *versus* malignant solid breast masses: US differentiation. *Radiology* **213**, 889–94.

[4] Jackson VP (1995). The current role of ultrasonography in breast imaging. *Radiol Clin North Am* **33**, 1161–170.

[5] Sickles EA (1988). Detection and diagnosis of breast cancer with mammography. *Perspect Radiol* **1**, 36–65.

[6] Yodh A, and Chance B (1995). Spectroscopy and imaging with diffusing light. *Phys Today* **48**, 34–40.

[7] Tromberg B, Shah N, Lanning R, Cerussi A, Espinoza J, Pham T, Svaasand L, and Butler J (2000). Non-invasive *in vivo* characterization of breast tumors using photon migration spectroscopy. *Neoplasia* **2** (1:2), 26–40.

[8] Franceschini MA, Moesta KT, Fantini S, Gaida G, Gratton E, Jess H, Seeber M, Schlag PM, and Kashke M (1997). Frequency-domain techniques enhance optical mammography: initial clinical results. *Proc Natl Acad Sci* **94**, 6468–473.

[9] Pogue B, Poplack SP, McBride TO, Wells WA, Osterman K, Osterberg U, and Paulsen KD (2001). Quantitative hemoglobin tomography with diffuse near-infrared spectroscopy: pilot results in the breast. *Radiology* **218**, 261–66.

[10] Dehghani H, Pogue B, Poplack SP, and Paulsen KD (2003). Multiwavelength three-dimensional near-infrared tomography of the breast: initial simulation, phantom, and clinical results. *Appl Opt* **42** (1), 135–45.

[11] Ntziachristos V, Yodh A, Schnall M, and Chance B (2000). Concurrent MRI and diffuse optical tomography of breast after indocyanine green enhancement. *Proc Natl Acad Sci* **97** (6), 2267–772.

[12] Jiang H, Xu Y, Iftimia N, Eggert J, Klove K, Baron L, and Fajardo L (2001). Three-dimensional optical tomographic imaging of breast in a human subject. *IEEE Trans Med Imaging* **20** (12), 1334–340.

[13] Jholboke M, Tromberg B, Li X, Shah N, Fishkin J, Kidney D, Butler J, Chance B, and Yodh A (2000). Three-dimensional diffuse optical mammography with ultrasound localization in human subject. *J Biomed Opt* **5** (2), 237–47.

[14] Vaupel P, Kallinowski F, and Okunieff P (1989). Blood flow, oxygen and nutrient supply, and metabolic microenvironment of human tumors: a review. *Cancer Res* **49**, 6449–465.

[15] Zhu Q, Dunrana T, Holboke M, Ntziachristos V, and Yodh A (1999). Imager that combines near infrared diffusive light and ultrasound. *Opt Lett* **24** (15), 1050–1052.

[16] Chen NG, Guo PY, Yan SK, Piao DQ, and Zhu Q (2001). Simultaneous near infrared diffusive light and ultrasound imaging. *Appl Opt* **40** (34), 6367.–380.

[17] Zhu Q, Conant E, and Chance B (2000). Optical imaging as an adjunct to sonograph in differentiating benign from malignant breast lesions. *J Biomed Opt* **5** (2), 229–36.

[18] Zhu Q, Chen NG, and Kurtzman HS (2003). Imaging tumor angiogenesis by the use of combined near infrared diffusive light and ultrasound. *Opt Lett* **28** (5), 337–39.

[19] Cope M (1991). PhD Dissertation University of College London.

[20] Zhu Q, Chen NG, Piao DQ, Guo PY, and Ding XH (2001). Design of near infrared imaging probe with the assistance of ultrasound localization. *Appl Opt* **40** (19), 3288–303.

[21] Gilles R, Zafrani B, Guinebretiere JM, et al. (1995). Ductal carcinoma *in situ*: MRI imaging–histopathologic correlation. *Radiology* **196**, 415–19.

[22] Fischer U, Westerhof JP, Brinck U, Korabiowska M, Schauer A, and Grabbe E (1996). The ductal carcinoma *in situ* in contrast-enhanced dynamic MR mammography. *RoFo* **164**, 290–94.

[23] Orel SG, Mendoca MH, Reynolds C, Schnall MD, Solin LJ, and Sullivan DC (1997). MR imaging of ductal carcinoma *in situ*. *Radiology* **202**, 413–20.

[24] Huang MM, Chen NG, Yuan BH, and Zhu Q (2003). 3D simultaneous absorption and scattering coefficients reconstruction for the reflection geometry. *Opt Tomogr Spectrosc Tissue V* **4955** (in press).

AUTHOR QUERIES

AUTHOR PLEASE ANSWER ALL QUERIES

1. There should be five keywords. Please supply one more.
2. Reference list: Please supply all author names in place of et al.
3. Ref. [24]: Please provide an update on the status of publication.

Appendix B

Will be submitted to Radiology

Benign versus Malignant Breast Masses: Optical Differentiation with US Localization

(work in progress)

Quing Zhu+, Edward Cronin*, Allen Currie*, Minming Huang+, NanGuang Chen+, Xu Chen+

+ Bioengineering Program, Electrical and Computer Engineering Department, University of

Connecticut, Storrs, CT 06269

*Radiology Department, Hartford Hospital, Hartford Connecticut, CT

Abstract

Purpose: To investigate the feasibility of optical tomography with ultrasonography (US) localization in differentiating benign from malignant breast masses. To compare optical method with Doppler US in mapping tumor angiogenesis.

Material and Methods: Using optical tomography with US localization, we have overcome the light scattering problem. A hand-held probe with a commercial ultrasound transducer deployed in the middle and optical sensors distributed at the periphery is used for simultaneously acquiring co-registered US image and optical measurements. The lesion location provided by US is used to segment the imaging volume for optical imaging reconstruction. Two optical wavelengths are used and three-dimensional (3D) light absorption maps at these wavelengths are obtained. From the absorption maps, lesion total hemoglobin concentration distribution, which is a direct measure of tumor angiogenesis, can be calculated.

Results: Initial results of 5 malignant cancers and 16 benign lesions have shown that small invasive cancers can be well-resolved in 3D optical absorption maps. The average maximum total hemoglobin concentrations for malignant and benign groups are 110.3 μ moles and 47.6 μ moles, respectively. The malignant group presents more than two-fold greater total hemoglobin concentration than that of the benign group.

Conclusion: Optical tomography with US localization has a great potential in differentiating benign from malignant breast lesions. The optical specificity on mapping tumor angiogenesis is much higher than Doppler US.

Index terms: US, Optical tomography, Diagnosis, Breast Neoplasma

Introduction

The large number of biopsies performed for benign breast abnormalities has long been recognized as a serious problem (1). The use of US as an adjunct to x-ray mammography decreased the number of biopsies by enabling reliable identification of simple cysts (2-4) from solid lesions. However, US features were not yet reliable enough to determine whether biopsy should be performed on a solid mass (5,6).

Tumor angiogenesis or neovascularity is known to be critical for the autonomous growth and spread of breast cancers (7,8). Tumor angeogenesis is a complex process involving both the incorporation of existing host blood vessels into the tumor and the creation of tumor microvessels. This process is moderated by tumor angiogenesis factor (9). In principle, the altered hemodynamics that accompany tumor angiogenesis provide the basis for discrimination between malignant and benign masses of the breast by color Doppler sonography (10). However, the contribution of Doppler US to differentiate benign and malignant solid masses is still controversial (11,12).

Optical tomography, a new technique that employs diffuse light in near infrared spectrum, has recently been under intensive investigations in pilot clinical studies (13-17). Optical tomography provides functional images of tumor angiogenesis and tumor hypoxia. If a single optical wavelength is used, the optical absorption related to tumor angiogenesis can be measured. If appropriately selected multiple wavelengths are used, the optical absorptions at these wavelengths can be measured and distributions of oxyhemoglobin (oxyHb) and deoxyhemoglobin (deoxyHb) of tumors can be deduced. The total hemoglobin concentration and tumor hypoxia can be calculated from distributions of oxyHb and deoxyHb and these functional parameters are highly correlated with lesion malignancy. However, optical tomography when used alone has been limited to feasibility studies in the past. The intense

scattering caused by tissue limits the imaging resolution as well as location certainty. Novel combination of optical tomography with other modalities, such as US and MRI, has shown promising results of utilizing full advantages of light to characterize malignancy versus benign processes (17-20). Flexible light guide using optical fibers makes optical imaging compatible with many other imaging modalities and allows for simultaneous imaging under identical geometric conditions. Further more, the lesion structure information provided by other modalities can be used to assist optical imaging reconstruction and therefore reduce the location uncertainty and improve the quantification accuracy of light.

We have investigated the optical tomography using a priori lesion structural information provided by co-registered US. The light guide using optical fibers are coupled to a hand-held probe with a commercial ultrasound transducer deployed in the middle. Preliminary results of 19 solid lesions have shown that two early stage invasive cancers have shown two-fold high total hemoglobin concentration than a group of benign lesions (19). Preliminary results of 4 advanced cancers have shown heterogeneous total hemoglobin distributions and the distributions correlate with histological micro-vessel density counts (20). In this paper, we further demonstrate the clinical potential of optical tomography assisted with US localization in distinguishing benign from malignant lesions, and we compare optical tomography with Doppler US on mapping tumor angiogenesis.

Materials and Methods

NIR system

A hand-held hybrid probe consists of a commercial ultrasound transducer located at the middle and near-infrared source-detector light guides (optical fibers) distributed at the periphery (see Fig.1). The

technical aspects of the NIR imager have been described in detail previously (21). Briefly, the imager consists of 12 pairs of dual wavelength (780nm and 830nm) laser diodes, which are used as light sources, and their outputs are coupled to the probe through optical fibers. On the receiving side, 8 photomultiplier tubes were used to detect diffusely scattered light from the tissue and 8 optical fibers were used to couple detected light to the PMTs. The laser diodes' outputs were amplitude modulated at 140 MHz and the detector outputs were demodulated to 20KHz. Eight detection signals and one reference were amplified, sampled and acquired into a PC simultaneously. The entire data acquisition took about 3 to 4 seconds, which was fast enough for acquiring data from patients.

Clinical protocol

Clinical studies were performed at the Radiology Department of Hartford Hospital. The Hartford Hospital IRB committee approved the human subject protocol. Patients who were scheduled for ultrasound guided biopsy were recruited to the study. The state-of-the art US scanner, Acuson Sequoia, was used for the study. Ultrasound images and optical measurements were acquired simultaneously before biopsy procedures at multiple locations including the lesion region, a normal region of the same breast, and a normal symmetric region of the contralateral breast. The optical data acquired at normal region were used as reference for calculating the scattered field caused by lesions.

Based on x-ray/US or MRI images, one of radiologists (EC, AC, VH) scored each biopsied lesion using BIRAD as possibly benign, suspicious, and highly suspicious for malignancy. For Doppler US measurements, any persistence color Doppler signals were taken to represent blood vessels. The location of the vessels with respect to the lesion was documented as peripheral to the lesion, within the lesion, or both.

Optical Imaging Method

The details of our dual-mesh optical imaging reconstruction algorithm have been described in Ref (19). Briefly, the NIR reconstruction takes advantages of ultrasound localization of lesions and segments the imaging volume into finer grid in lesion region and coarser grid in non-lesion regions. A modified Born approximation is used to relate the scattered field measured at the source-detector pairs to absorption variations in each volume element of two regions within the sample. With this dual-mesh scheme, the inverse optical reconstruction is well-conditioned and converges in few iterations.

Results

The first example was obtained from a 45-year old woman who had a suspicious lesion located at 12 o' clock position shown on MRI. The lesion was identified sonographically at the time of biopsy as ill-defined slightly heterogeneous, mildly hypoechoic mass of 7 mm in diameter. Doppler US revealed large blood vessels both inside and at peripheral of the lesion (Fig.2 (a)). US images and optical measurements were obtained simultaneous before US guided biopsy procedure. Surgical pathology reports revealed that the lesion was intraductal and invasive mammary duct carcinoma (nuclear grade III, histologic grade III).

The average tissue background optical absorption coefficients μ_a and reduced scattering coefficients μ'_s at 780 nm and 830 nm were measured at the normal contralateral breast as $\mu_a^{780} = 0.07$ cm^{-1}, $\mu'^{780}_s = 5.32$cm^{-1}, $\mu_a^{830} = 0.06$ cm^{-1} and $\mu'^{830}_s = 5.83$ cm^{-1}, respectively. Optical absorption maps of lesion region at both wavelengths 780nm and 830 nm were reconstructed as shown in Fig. 2(b) and (c). The first slice is the spatial x-y image of 0.5 cm deep from the skin surface and the last slice is 3.5 cm deep toward the chest wall. The spacing between the slices is 0.5 cm. The vertical scale is the absorption

coefficient in cm^{-1}. The lesion is well resolved in slice #2. The total hemoglobin concentration map is shown in Fig 2. (d) and the vertical scale is in μM. The measured maximum value at lesion area is 162.0 μM with the average value of 121.1 μM calculated within full width of half maximum (FWHM) of the maximum value. The average background total hemoglobin outside of the FWHM region is 29.1 μM. Since our hand-held probe can be easily rotated or translated, we have acquired at least three co-registered ultrasound and NIR data sets at the lesion location and reconstructed the corresponding optical absorption maps as well as the total hemoglobin concentration distribution under the co-registered ultrasound guidance. The average maximum total hemoglobin concentration at the cancer region is 149.91 μmoles ($\pm$39.23 μmoles) and the average background total hemoglobin concentration is 29.03 μmoles ($\pm$0.18 μmoles). The large standard deviation obtained from slightly different probe positions is likely due to the probe compression at different positions and elastic properties of the blood vessels in the cancer region. We have noticed in our earlier studies that one of the two early stage invasive cancers showed a large standard deviation on total hemoglobin concentrations at the cancer region with similar scales (19).

Another example was obtained from a 37-year old woman who had a known infiltrating lobular carcinoma (nuclear grade II-III) located at 12 o'clock position of the right breast and measuring 1 cm in size by US at the time of this study (Fig. 3(a)). The patient had family history of breast cancer. Two new lesions located at 7 o'clock of the same breast and 10 o'clock of the contralateral breast were shown in MRI. The new lesions were identified sonographically at the time of biopsy measuring 6 and 7 mm in diameter, respectively. Figure 4 (a) is the US image of the 7 o'clock right breast lesion. No blood vessels or flow were identified in all lesions by Doppler US.

The average tissue background optical absorption coefficients μ_a and reduced scattering coefficients μ'_s at 780 nm and 830 nm were measured at contralateral normal breast area as μ_a^{780}=0.03 cm^{-1}, μ'^{780}_s = 8.08cm^{-1}, μ_a^{830} = 0.03 cm^{-1} and μ'^{830}_s=7.76 cm^{-1}, respectively. The absorption maps of the known cancer at both wavelength are shown in Fig.3 (b) and (c) and the computed total hemoglobin concentration map is shown in Fig.3 (d). The lesion is resolved in slices #3 and #4 and shown 110.4 μM peak and 77.8 μM average total hemoglobin concentration, respectively. The mean maximum hemoglobin concentration of three NIR scans at slightly different probe locations is 102.1 μM and the mean within FWHM of the three NIR scans is 68.7 μM . The absorption maps of the new lesion located at the 7 o'clock position of the same breast are shown in Fig. 4(b) and (c) and the total hemoglobin concentration is shown in Fig. 4(d). No resolvable lesion was found in absorption maps and the maximum total hemoglobin concentration is only 24.2 μM. The biopsy result revealed benign non-proliferative fibroadipose breast tissue with focal microcystic alteration, apocrine metaplasia and periductal chronic mastitis. No atypical cells were found. The 10 o'clock suspicious lesion of the contralateral breast had similar ultrasonic and optical characteristics. No resolvable lesion was found in optical absorption maps and the maximum total hemoglobin concentration is only 27.5 μM. The biopsy result revealed benign proliferative fibroadipose breast tissue with focal aprocrine papillary epitheliosis. No atypical cells were found. This example demonstrates that the specificity of optical contrast is much higher than that of Doppler US as it is related to the microvessel development of tumor angiogenesis process in contrast to the larger vessels seen by Doppler US.

The third example was obtained from a 75-year old woman who had a suspicious lesion with solid component (pointed by the arrow in Fig. 5 (a)) adjacent to a cyst. The lesion was located at 9 o'clock of the right breast. Doppler US has shown several large blood vessels located at the peripheral of the

lesion. Optical absorption maps at both wavelengths as well as the total hemoglobin concentration map are shown in Fig. 5(b), (c) and (d), respectively. The absorption maps of the lesion have showed low light absorption and low hemoglobin concentration. The absorption distributions are quite diffused as compared with the localized distributions of malignant cancer cases. The measured maximum total hemoglobin concentration is 38.18 μM and the average is 26.31 μM. The biopsy result revealed that the lesion was intraductuctal papilloma with no evidence of atypical cells or malignancy.

The last example was obtained from a 47-year old woman who had a suspicious tabulated solid nodule shown in Fig. 6(a). No blood flow was observed in Doppler US. The patient had family history of breast cancer. Optical absorption maps as well as the total hemoglobin concentration map are shown in Fig.6 (b)-(c). The lesion was resolved in slice 2 and showed 83.0 μM maximum and 60.8 μM average total hemoglobin concentration. The biopsy result revealed benign breast tissue with minimally proliferative fibrocystic changes and dense fibrosis. This lesion has the highest total hemoglobin concentration among all the benign cases reported in this paper. Since this patent had family history of breast cancer, 6 months follow up is scheduled. The possibility of core biopsy might have missed the suspicious area cannot be completely ruled out.

Tables I and II list results of 5 malignant cases (5 malignant cancers and 3 benign lesions) and 10 benign cases (13 benign lesions) studied so far. Starting from column 2, the tables provide biopsy results, measured lesion size by US, combined x-ray, US and/or MRI diagnosis, Doppler US findings, measured mean maximum value of total hemoglobin concentration with mean taken at three probe positions, measured mean average value of total hemoglobin concentration with mean taken at three probe positions, and measured lesion size by NIR using FWFM. In Table I, two patients (Ref. #52 and Ref.

#23) have multiple benign lesions in addition to malignant ones and the results are grouped in Table I under the same reference number. The first important finding is that the invasive cancers have shown much higher total hemoglobin concentrations than those of benign cases. Figure 7 provides statistics of these two groups. The mean values of maximum and average total hemoglobin concentration of malignant group (5 lesions) are 110.3 μM (± 21.2 μM) and 76.7 μM ($\pm 18.3 \mu$M), respectively, and mean values of benign group (16 lesions) are 47.2 μM (± 18.5 μM) and 32.9 μM ($\pm 13.2 \mu$M), respectively. A more than two-fold greater optical contrast is obtained from malignant group and it suggests that the optical differentiation of benign and malignant breast masses is feasible. The mean sizes measured by US for these two groups were 1.22 cm and 0.7 cm, respectively. The second important finding is that optical tomography provides much higher specificity than Doppler US. Although Doppler US blood flow was demonstrated in three out of five malignant cases, the blood flow was also present in many benign cases. Since the diffused light probes microvessel density rather than relatively large blood vessels as the Doppler US, the specificity of optical contrast is expected to be much higher than Doppler US.

Discussion

With the increased public awareness of the potential benefits of early detection of breast cancer, more women are now practicing self-examination and undergo periodic screening. As a result, more lesions are being detected by palpation, screening mammography and screening MRI for high risk or dense breasts. Consequently, radiologists and surgeons are performing an even increasing number of breast biopsies, with the vast majority of these revealing benign findings. Therefore, alternative, less invasive methods of distinguishing malignant from benign masses are needed to reduce the number of unnecessary biopsies. US is frequently used as an adjunct tool to x-ray mammography in differentiating

simple cysts from solid lesions and also plays an important role in guiding interventional procedures such as needle aspiration, core-needle biopsy, and prebiopsy needle localization (4, 22,23). Recently, screening US has also been advocated for the dense breast (24). However, the specificity of Doppler US and gray scale imaging in differentiating benign from malignant lesions is low as many solid lesions are diagnosed as suspicious. Our technique of using optical tomography with US localization has demonstrated a great potential for non-invasively distinguishing malignant and benign solid masses and therefore a potential role for reducing unnecessary biopsies. Earlier results obtained from two invasive early stage cancers and 17 benign lesions have shown that malignant cancers of 1 cm in size present an average of 119 μM maximum total hemoglobin concentration while the benign group has an average of 67 μM. A nearly two hold higher contrast has been obtained. This paper further demonstrates the diagnostic potential of this technique with 5 cancer cases and a group of 16 biopsied benign solid lesions. Again, the invasive cancers reveal about two-fold greater total hemoglobin concentration (mean 110.3 μM) compared with benign cases (mean 47.3 μM). Currently, more patients are being recruited to this study from multiple clinical sites and the specificity of the optical method with US localization in breast cancer diagnosis will be reported in the near future. Our technique may also be useful for monitoring chemotherapy responses of breast cancer treatment and assessing treatment efficacy (20).

Due to intense light scattering, optical tomography alone has not been widely used in clinical studies. The data in the published literature have been limited to case reports. Furthermore, the optical systems and measurement configurations vary among different research groups. Pogue et al reported pilot results of one invasive ductal carcinoma and one benign fibroadenoma (13). The reported maximum total hemoglobin concentrations were 68 μmoles for the cancer case and 55 μmoles for the benign

case. Since the system they used can only acquire NIR data from a ring area with optical source and detectors deployed around the breast (two-dimensional imager). Therefore, incomplete information could lead to smaller reconstructed absorption coefficients and total hemoglobin concentrations than those reported here using our three-dimensional NIR imager. In another study (25), the authors used the *a priori* lesion depth information acquired from a separate US image and obtained an average of 67 μmole total hemoglobin concentration from a ductual carcinoma in situ. This value is close to the average of 76.7 μmoles obtained from the malignant group reported in this paper.

In principle, the distribution of oxygenation saturation can be estimated as S = oxyHb /(oxyHb+deoxyHb) with deoxyHb and oxyHb distributions calculated from absorption maps at the two wavelengths of 780 nm and 830 nm. However, since background tissue mainly consists of water and lipid and these two chromophores contribute to the total absorption estimate as well, we could not obtain reasonable background oxygenation saturation and compare it with lesion oxygenation saturation. Currently, we are in the process of adding more wavelengths to the NIR system. Nevertheless, initial experience with a small group of cancer cases suggests that the deoxyHb concentration of malignant lesions may not be as significant as stressed by previous investigators but the total hemoglobin concentration (deoxyHb + oxyHb) is highly specific in differentiating small invasive malignant cancers from benign lesions.

Acknowledgements

References:

1. Howard J. Using mammography for cancer control: an unrealized potential. Cancer 1987; 33:33-48.

2. Hilton SW, Leopold GR, Olson LK, Willson SA. Real-time breast sonography: application in 300 consecutive patients. AJR 1986; 147:479-486.

3. Rubin E, Miller VE, Berland LL, Han SY, Koehler RE, Stanley RJ. Hand-held real-time breast sonography. AJR 1985; 144:623-627.

4. Jackson VP. The current role of ultrasonography in breast imaging. Radiol Clin North Am 1995; 33: 1161-1170.

5. Sickles EA, Filly FA, Callen PW. Breast cancer detection with ultrasonography and mammography: comparison using state-of-the-art equipment. AJR 1983; 140:843-845.

6. Rahbar G, Sie AC, Hansen GC, Prince JS. Melany ML, Reynolds HE. Jackson VP, Sayre JW and Bassett LW. Benign versus malignant solid masses: US differentiation. Radiology 1999; 213:889-894.

7. Schor AM, Schor SL. Tumour angiogenesis. J Pathol 1983; 141:385-413.

8. Folkman J, Watson K, Ingber D, Hanahan D. Induction of angiogenesis during the transition from hyperplasia to neoplasia. Nature 1989; 339:58-61.

9. Vaupel P, Kallinowski F, Okunieff P. Blood flow, oxygen and nutrient supply, and metabolic microenvironment of human tumors: a review. Cancer Research 1989; 49: 6449-6465.

10. Taylor KJW, Ramos I, Carter D. et al. Correlation of Doppler US tumor signals with neovascular morphologic features. Radiology 1988; 166-57.

11. Wilkens TH, Burke BJ, Cancelada DA, Jatoi I. Evaluation of palpable breast masses with color Doppler sonography and gray scale imaging. J Ultrasound Med 1998; 17:109-115.

12. Reinukainen H, Rissanen, T, Paivansalo, M, Paakko, E, jauhiainen, J, and Suramo, I. B-mode, power Doppler and contrast-enhanced power Doppler ultrasonography in the diagnosis of breast tumors. Acta Radiologica 2001; 42 (1): 106-113.

13. Pogue B, Poplack SP, McBride TO, Wells WA, Osterman K, Osterberg U, and Paulsen KD. Quantitative hemoglobin tomography with diffuse near-infrared spectroscopy: pilot results in the breast. Radiology 2001; 218: 261-266.

14. Franceschini MA, Moesta KT, Fantini S, Gaida G, Gratton E, Jess H, Seeber M, Schlag PM, Kashke M. Frequency-domain techniques enhance optical mammography: initial clinical results. Proc. of Nat. Ac. of Sci., 1997; 94: 6468-6473.

15. Tromberg B, Shah N, Lanning R, Cerussi A, Espinoza J, Pham T, Svaasand L, and Butler J. Non-Invasive in vivo characterization of breast tumors using photon migration spectroscopy. Neoplasia 2000; 2(1:2): 26-40.

16. Jiang H, Xu Y, Iftimia N, Eggert J, Klove K, Baron L and Fajardo L (2001). Three-dimensional optical tomographic imaging of breast in a human subject. IEEE Trans on Medical Imaging, 20(12), 1334-1340.

17. Ntziachristos V, Yodh A, Schnall M., and Chance B. Concurrent MRI and diffuse optical tomography of breast after indocyanine green enhancement. Proc. of Nat. Ac. of Sci. 2000; 97 (6): 2267-2772.

18. Zhu Q, Chen NG, Kurtzman HS. Imaging tumor angiogenesis by the use of combined near infrared diffusive light and ultrasound. Optics Letters 2003; 28 (5): 337-339.

19. Zhu Q., Huang, MM, Chen, NG, Zarfos, K, Jagjivan, B, Kane, M, Hegde P, Kurtzman, SH. Ultrasound-guided optical tomographic imaging of malignant and benign breast lesions: initial clinical results of 19 cases. Neoplasia 2003; 5(5). in press.

20. Zhu Q,, Kurtzman SH, Hegde P., Huang MM, Chen NG, Jagjivan B, Kane M, Zarfos K. Imaging heterogeneous tumor angiogenesis distributions of advanced breast cancers by optical tomography with ultrasound localization. Submitted to Proc. of Nat. Ac. of Sci.

21. Chen NG, Guo PY, Yan SK, Piao DQ, and Zhu Q. Simultaneous near infrared diffusive light and ultrasound imaging. Applied Optics 2001; 40 (34): 6367-6380.

22. Bassett LW, Ysrael M, Gold RH, Ysrael C. Usefulness of mammography and sonography in women less than 35 years of age. Radiology 1991; 180:831-835.

23. Fornage BD, Coan JD, David CL. Ultrasound-guided needle biopsy of the breast and other interventional procedures. Radiol Clin North Am 1992; 30:167-185.

24. T.M. Kolb, J. Lichy and J. H. Newhouse, "Occult cancer in women with dense breast: detection with screening US - diagnostic yield and tumor characteristics," Radiology 1998; **207**: 191-199.

25. Jholboke M, Tromberg B, Li X, Shah N, Fishkin J, Kidney D, Butler J, Chance B, and Yodh A. Three-dimentional diffuse optical mammography with ultrasound localization in human subject. Journal of Biomedical Optics 2000; **5**(2): 237-247.

Figure Captions

Fig. 1. (a) Picture of the combined probe and frequency domain NIR imager. (b) Sensor distribution of the combined probe. Smaller circles in (b) are optical source fibers and big circles are detector fibers. A commercial ultrasound probe is located at the center of the combined probe and the optical source and detector fibers are distributed at the periphery of the ultrasound probe.

Fig. 2. (ID41P2). (a) US image of a suspicious lesion located at 3 o'clock of the left breast of a 45-year old woman. Doppler US revealed large blood vessels both inside and at peripheral of the lesion. (b) and (c) are optical absorption maps at 780 nm and 830 nm, respectively. The first slice is the spatial x-y image of 0.5 cm deep from the skin surface and the last slice is 3.5 cm toward the chest wall. The spacing between the slices is 0.5 cm. The lesion is well resolved in slice #2. (d) The total hemoglobin concentration map computed from absorption maps of (b) and (c). The vertical scale is the total hemoglobin concentration in μ M.

Fig. 3. (ID52P7). (a) US image of an infiltrating lobular carcinoma located at 12 o'clock position of the right breast of a 37-year old woman. The lesion was measured 1 cm in size by US at the time of this study. No blood vessels or flow were seen by Doppler US. (b) and (c) are optical absorption maps at 780 nm and 830 nm, respectively. (d) The total hemoglobin concentration map computed from absorption maps of (b) and (c). The lesion is resolved in slices 3 and 4.
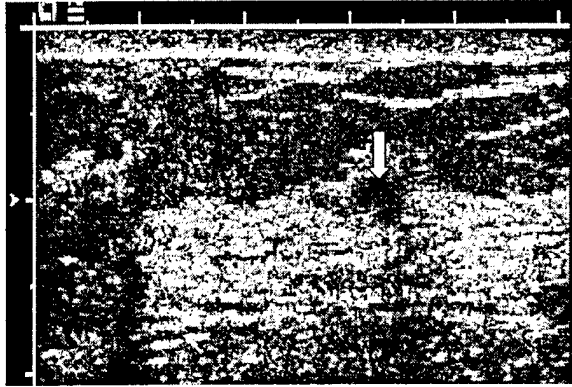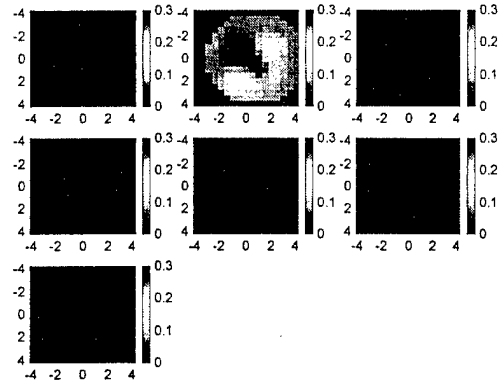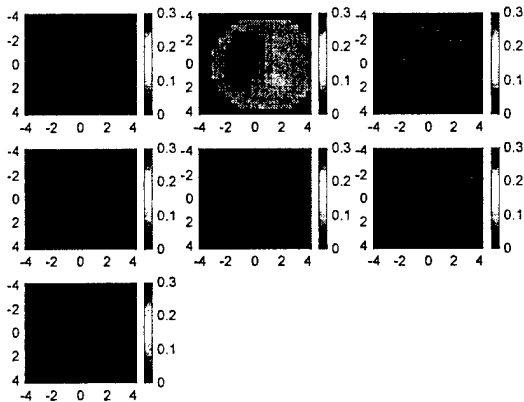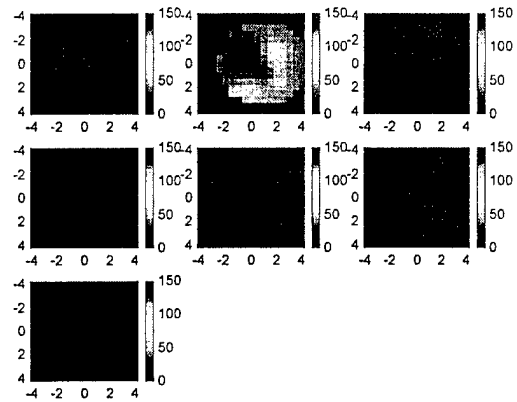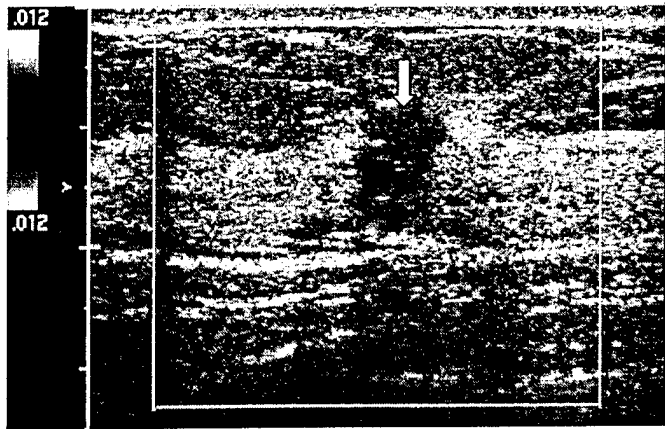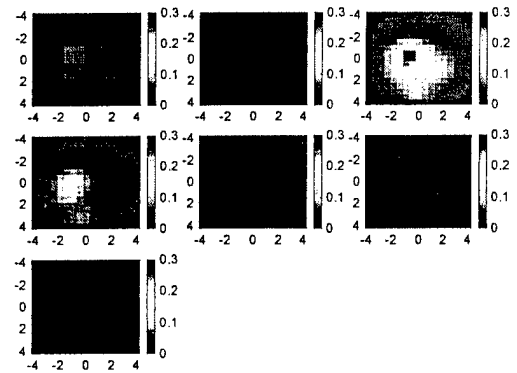
Fig. 4. (ID52P17). (a) US image of a suspicious lesion located at 7 o'clock of the right breast of the same patient with an infiltrating lobular carcinoma shown in Fig.3. No blood vessels or flow were seen by Doppler US. (b) and (c) are optical absorption maps at 780 nm and 830 nm,

respectively. (d) The total hemoglobin concentration map computed from absorption maps of (b) and (c).

Fig. 5. (ID54P3_P17 REF). (a) US image of a suspicious lesion located at 9 o'clock of the right breast of a 75-year old woman. Large blood vessels were seen by Doppler US at the peripheral of the lesion. (b) and (c) are optical absorption maps at 780 nm and 830 nm, respectively. (d) The total hemoglobin concentration map computed from absorption maps of (b) and (c).

Fig. 6. (ID58P1). (a) US image of a suspicious lesion located at 7 o'clock of the left breast of a 47-year old woman. The patient had family history of breast cancer. No blood flow was seen by Doppler US. (b) and (c) are optical absorption maps at 780 nm and 830 nm, respectively. (d) The total hemoglobin concentration map computed from absorption maps of (b) and (c).

Fig. 7. Statistics of measured total hemoglobin concentration of benign and malignant groups.

Table Captions

Table I: Biopsy, US and NIR Parameters of 5 Cancer Cases

Table II: Biopsy, US and NIR Parameters of 11 Benign Cases

(a)

(b)

Fig.1.

(a)

(b)

(c)

(d)

Fig. 2. (ID41P2). (a) US image of a suspicious lesion located at 3 o'clock of the left breast of a 45-year old woman. Doppler US revealed large blood vessels both inside and at peripheral of the lesion. (b) and (c) are optical absorption maps at 780 nm and 830 nm, respectively. The first slice is the spatial x-y image of 0.5 cm deep from the skin surface and the last slice is 3.5 cm toward the chest wall. The spacing between the slices is 0.5 cm. The lesion is well resolved in slice #2. (d) The total hemoglobin concentration map computed from absorption maps of (b) and (c). The vertical scale is the total hemoglobin concentration in μM.

(a)

(b)

(c)

(d)

Fig. 4. (ID52P17_P38 REF). (a) US image of a suspicious lesion located at 7 o'clock of the right breast of the same patient with an infiltrating lobular carcinoma shown in Fig.3. No blood vessels or flow were seen by Doppler US. (b) and (c) are optical absorption maps at 780 nm and 830 nm, respectively. (d) The total hemoglobin concentration map computed from absorption maps of (b) and (c).
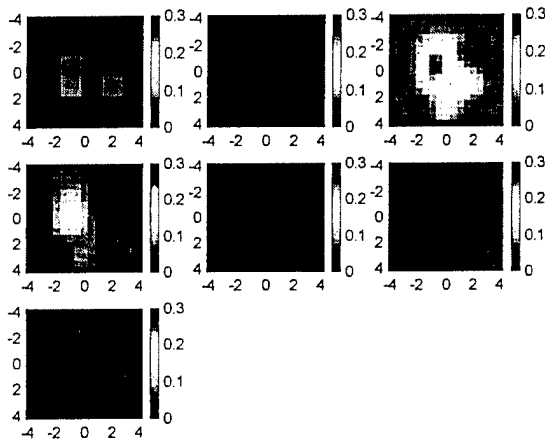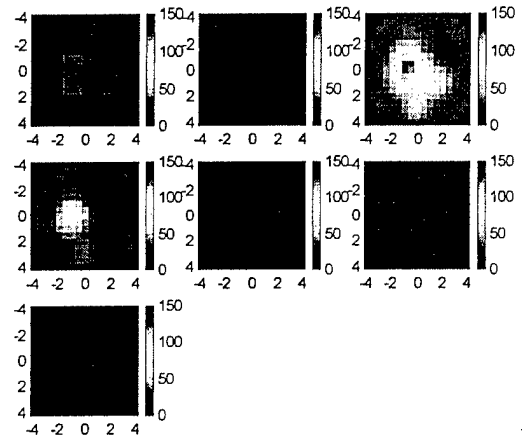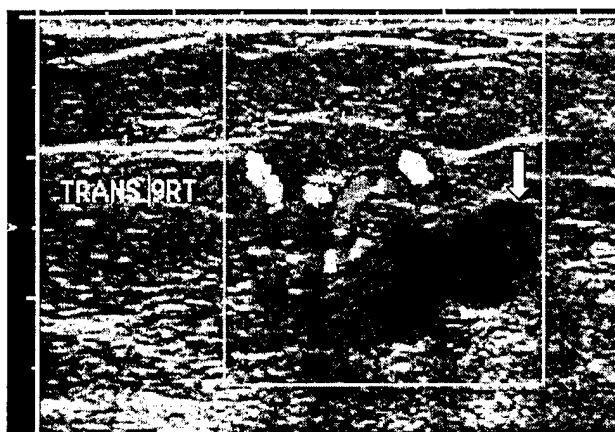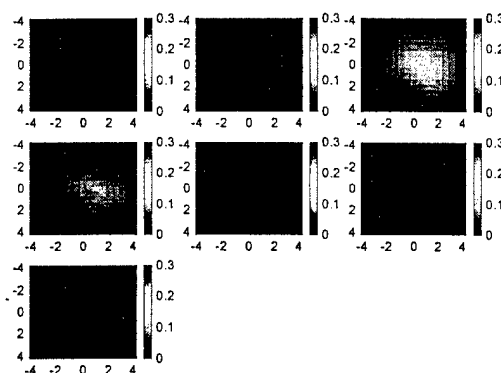
(a)

(b)

(c)

(d)

Fig. 3. (ID52P7). (a) US image of an infiltrating lobular carcinoma located at 12 o'clock position of the right breast of a 37-year old woman. The lesion was measured 1 cm in size by US at the time of this study. No blood vessels or flow were seen by Doppler US. (b) and (c) are optical absorption maps at 780 nm and 830 nm, respectively. (d) The total hemoglobin concentration map computed from absorption maps of (b) and (c). The lesion is resolved in slices 3 and 4.
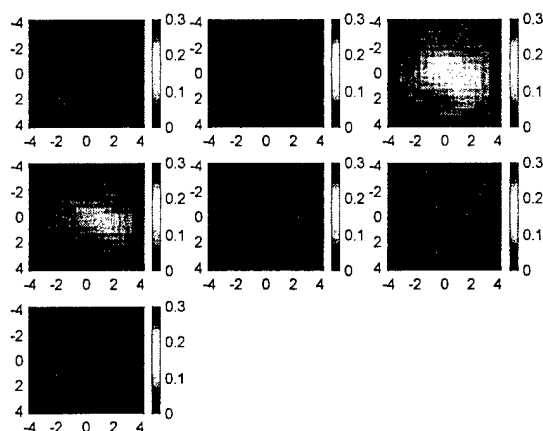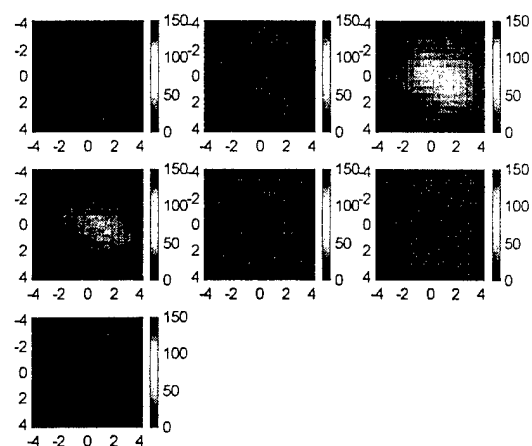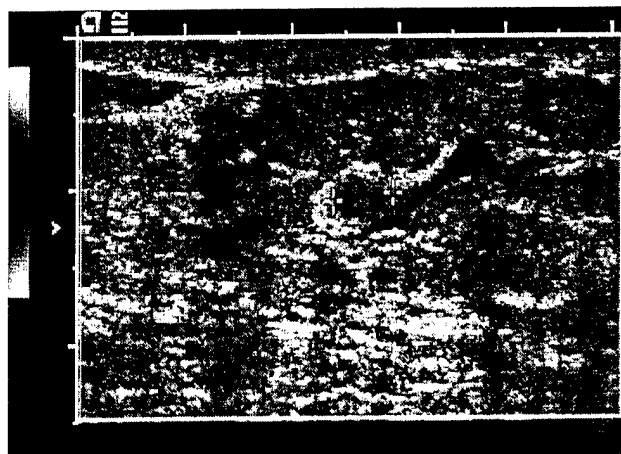
(a)

(b)

(c)

(d)

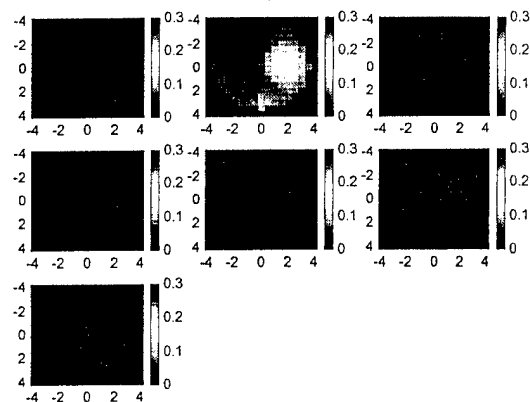Fig. 5. (ID54P3_P17 REF). (a) US image of a suspicious lesion located at 9 o'clock of the right breast of a 75-year old woman. Large blood vessels were seen by Doppler US at the peripheral of the lesion. (b) and (c) are optical absorption maps at 780 nm and 830 nm, respectively. (d) The total hemoglobin concentration map computed from absorption maps of (b) and (c).

(a)

(b)

(c)

(d)

Fig. 6. (ID58P1). (a) US image of a suspicious tabulated solid lesion located at 7 o'clock of the left breast of a 47-year old woman. The patient had family history of breast cancer. No blood flow was seen by Doppler US. (b) and (c) are optical absorption maps at 780 nm and 830 nm, respectively. (d) The total hemoglobin concentration map computed from absorption maps of (b) and (c).
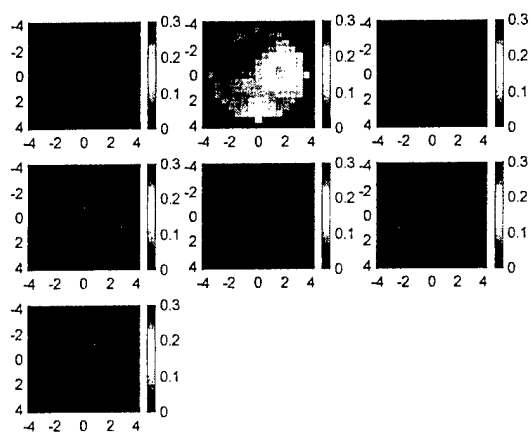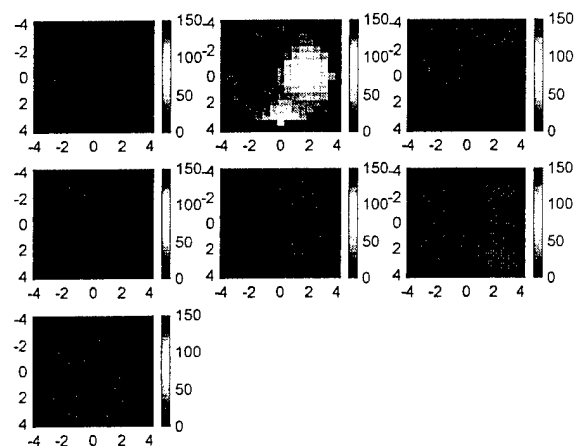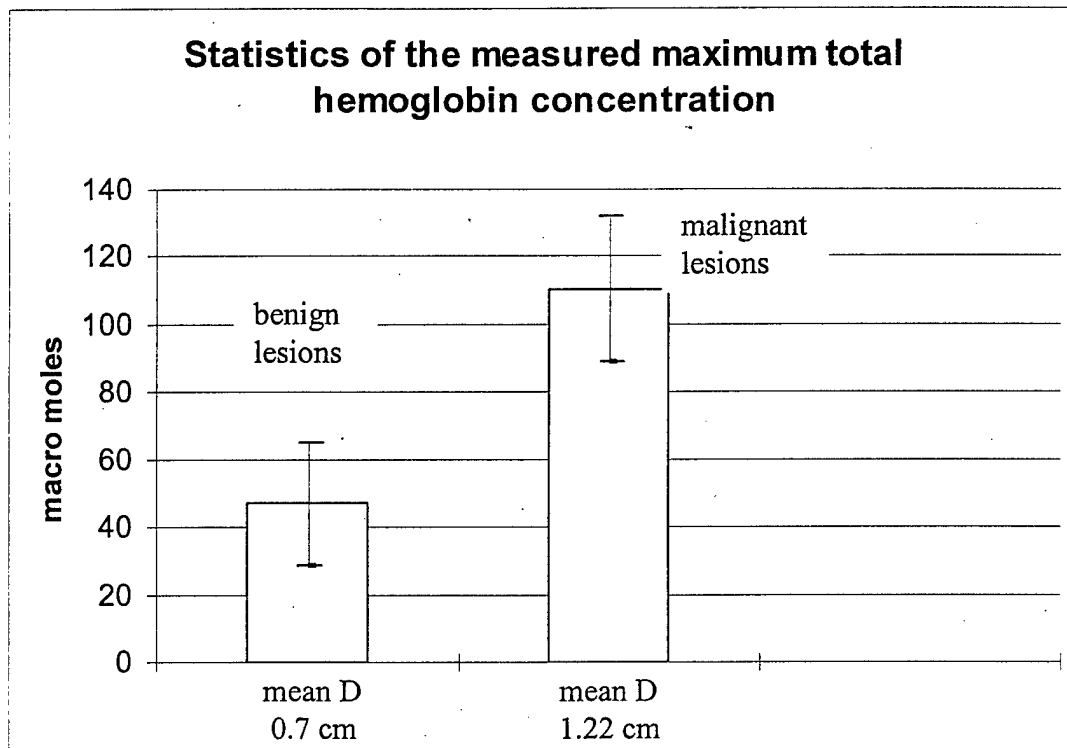
Statistics of the measured maximum total hemoglobin concentration

Fig.7.

Table I: Biopsy, US and NIR Parameters of 5 Cancer Cases and 3 Benign Lesions

Ref. #	Biopsy Results	Size(US) cm	US Diagnosis	Doppler US	Total Hb (max μM)	Total Hb (ave) μM	Size (NIR) cm
#41	intraductal and invasive mammary duct carcinoma	0.8x0.5	suspicious	both	147.9 ($\pm$ 39.2)	109.5 ($\pm$ 30.8)	2.67
#52	#1: infiltrating lobular carcinoma	0.91x0.92	known at biopsy	no flow	102.1 ($\pm$ 8.1)	68.7 ($\pm$ 8.6)	3.91
	#2: non-proliferative fibroadipose breast tissue	0.62x0.33	suspicious	no flow	24.2 ($\pm$ 12.8)	17.3 ($\pm$ 7.3)	5.25
	#3: proliferative fibroadipose breast tissue	0.66x0.33	suspicious	no flow	27.5	21.1	4.69
#30	invasive mammary duct carcinoma & DCIS	1.1x1.1	highly suspicious	peripheral	97.5 ($\pm$ 12.5)	67.7 ($\pm$ 9.4)	4.62
#46	infiltrating ductal carcinoma & DCIS	1.2x0.8	suspicious	no flow	100.0 ($\pm$ 9.6)	68.4 ($\pm$ 6.2)	3.71
#23	#1: intraductal and invasive mammary duct carcinoma	3.1x	known at biopsy	Peripheral	103.8 ($\pm$0.8)	69.2 ($\pm$ 0.9)	4.91
	#2: non-proliferate fibrocystic changes	0.72x0.43	suspicious	inside	68.7 ($\pm$2.34)	48.5 ($\pm$4.9)	4.58

Table II: Biopsy, US and NIR Parameters of 10 Benign Cases (13 lesions)

Ref. #	Biopsy Results	Size(US) cm	US Diagnosis	Doppler US	Total Hb (max μM)	Total Hb (ave) μM	Size (NIR) cm
#54	Intraductal papilloma	1.88x1.11	suspicious	peripheral	38.3 ($\pm$1.4)	26.6 ($\pm$1.1)	5.24
#45	fibroadenoma	1.92x1.02	suspicious	both	28.7 ($\pm$2.4)	17.6 ($\pm$2.2)	8.0
#28	Apocrine cyst	0.6x0.35	probably benign	peripheral	36.1 ($\pm$4.8)	24.6 ($\pm$3.4)	7.0
#31	Breast tissue showing nodular dense fibrosis hyalinized fibroadenoma	#1*:1.2x0.72	suspicious	Peripheral	37.8 ($\pm$0.3)	26.2 ($\pm$0.2)	4.89
		#2*:0.53x0.58	suspicious	no flow	37.8 ($\pm$0.3)	26.2 ($\pm$0.2)	
	fibroadenoma	#3:0.69x0.47	suspicious	no flow	70.9 ($\pm$2.4)	49.9 ($\pm$1.2)	3.24
#25	Sclerotic fibroadenoma	1.13x0.88	suspicious	no flow	48.7 ($\pm$2.9)	32.2 ($\pm$2.2)	2.64
#68	Proliferative fibrocystic changes	0.42x0.53	suspicious	peripheral	25.8 ($\pm$1.8)	17.9 ($\pm$2.5)	7.14
#61	Fibrocystic changes	0.47x0.48	suspicious	peripheral	59.5 ($\pm$7.2)	40.7 ($\pm$6.1)	4.21
#57	fibroadenoma	0.6 x 0.4 0.6 x 0.4	both are suspicious	no flow	63.0 ($\pm$2.3)	43.0 ($\pm$1.8)	2.47 2.91
#58	fibrocystic changes	0.51x0.38	suspicious	no flow	79.2 ($\pm$15.4)	56.9 ($\pm$10.7)	2.81
#21	fibroadenoma	0.61x0.38	suspicious	no flow	62.3 ($\pm$1.0)	44.1 ($\pm$0.4)	2.16

*these two lesions were located at 2:30 and 3 o'clock positions and were functionally un-resolvable.

Imaging tumor angiogenesis by use of combined near-infrared diffusive light and ultrasound

Appendix C

Quing Zhu and NanGuang Chen

Department of Electrical and Computer Engineering, University of Connecticut, Storrs, Connecticut 06269-2157

Scott H. Kurtzman

University of Connecticut Health Center, Farmington, Connecticut 06030

A novel two-step reconstruction scheme using a combined near-infrared and ultrasound technique and its utility in imaging distributions of optical absorption and hemoglobin concentration of breast lesions are demonstrated. In the first-step image reconstruction, the entire tissue volume is segmented based on initial coregistered ultrasound measurements into lesion and background regions. Reconstruction is performed by use of a finer grid for lesion region and a coarse grid for the background tissue. As a result, the total number of voxels with unknown absorption can be maintained on the same order of total measurements, and the matrix with unknown total absorption distribution is appropriately scaled for inversion. In the second step, image reconstruction is refined by optimization of lesion parameters measured from ultrasound images. It is shown that detailed distributions of wavelength-dependent absorption and hemoglobin concentration of breast carcinoma can be obtained with the new reconstruction scheme. © 2003 Optical Society of America

OCIS codes: 170.0170, 170.3010, 170.5270, 170.7170, 170.3830.

Tumor blood volume and microvascular density are parameters that are anatomically and functionally associated with tumor angiogenesis. During the past decade, modeling of light propagation in the near-infrared (NIR) region, combined with advancements of light source and detectors, has improved diffused light measurements and made possible the application of tomographic techniques for characterizing and imaging tumor angiogenesis.[1,2] However, the NIR technique has not been widely used in clinics, and the fundamental problem of intense light scattering remains. As a result, diffusive light probes a widespread region instead of providing information along a straight line, and tomographic image reconstruction is, in general, underdetermined and ill-posed. Zhu et al.[3] and Chen et al.[4] demonstrated a combined imaging technique, using *a priori* lesion structure information provided by coregistered ultrasound images to assist NIR imaging reconstruction in phantom studies.[3,4] As a result, the NIR image reconstruction is well defined and less sensitive to noise. In this Letter we report on our novel two-step image reconstruction scheme that uses the combined approach and demonstrate its utility in imaging tumor absorption and hemoglobin distributions. It is shown that detailed heterogeneous distributions of wavelength-dependent optical absorption and hemoglobin concentration of a breast carcinoma can be obtained. To the best of our knowledge, such detailed distributions have not been reported in the literature.

A picture of our combined hand-held probe used in clinical studies is shown in Fig. 1(a), and the probe dimensions and optical sensor distributions are shown in Fig. 1(b). The combined probe consists of a commercial ultrasound one-dimensional array located at the center of the probe and optical source and detector fibers distributed at the periphery and connected to the NIR imager. The NIR imager consists of 12 dual-wavelength source channels and 8 parallel receiving channels.[4] In the transmission part, 12 pairs of dual-wavelength (780- and 830-nm) laser diodes are amplitude modulated at 140 MHz. In the reception part, 8 photomultiplier tubes detect diffusely reflected light from the tissue. Both the amplitude and phase at each source–detector pair are obtained, and the resulting total number of measurements is $12 \times 8 \times 2 = 192$. The combined probe is made of a black plastic plate 10 cm in diameter; therefore, a semi-infinite boundary condition can be used for the NIR measurement geometry. The amplitude and phase measured from the normal side of the breast are used to calculate the background absorption $\bar{\mu}_a$ and reduced scattering coefficient $\bar{\mu}_s'$.[4] In our two-step image reconstruction, we first segment tissue volume into two regions, L and B, that contain a lesion as measured from coregistered ultrasound images and background tissue, respectively. We use the Born approximation to
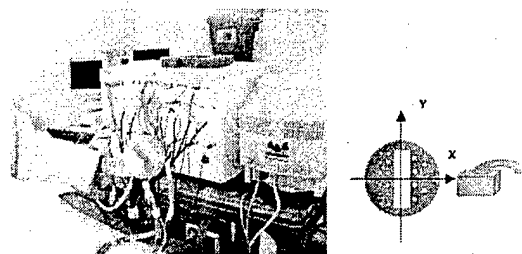

Fig. 1. (a) Hand-held combined probe and a frequency-domain NIR imager. (b) Sensor distribution of the combined probe (diameter, 10 cm). The smaller circles are optical source fibers, and the bigger circles are detector fibers. A commercial ultrasound probe is located at the center and its dimensions are 5.6 cm by 1 cm.

relate the scattered field $U_{sc}'(r_{si}, r_{di}, \omega)$ measured at source–detector pair i to absorption variations $\Delta\mu_a(r')$ in each volume element of two regions within the sample, where r_{si} and r_{di} are the source and detector positions, respectively. We then discretize the lesion volume and the background volume with different voxel sizes (a finer grid for lesion volume and a coarse grid for background). The scattered field can then be approximated as

$$U_{sc}'(r_{si}, r_{di}, \omega) \approx -\frac{1}{\overline{D}}$$
$$\times \left\lceil \sum_{Lj} G(r_{vj}, r_{di}) U_{inc}(r_{vj}, r_{si}) \int_j \Delta\mu_a(r') d^3 r' \right.$$
$$\left. + \sum_{Bk} G(r_{vk}, r_{di}) U_{inc}(r_{vk}, r_{si}) \int_k \Delta\mu_a(r') d^3 r' \right\rceil, \quad (1)$$

where r_{vj} and r_{vk} are the centers of voxels j and k in lesion volume L and background volume B, respectively[2], and $U_{inc}(r', r_{si})$ and $G(r', r_{di})$ are the incident wave and the Green function of the semi-infinite geometry, respectively. The matrix form of relation (1) is given as

$$[U_{sd}]_{M \times 1} = [W_L, W_B]_{M \times N}[M_L, M_B]^T, \quad (2)$$

where $W_L = [-1/_D G(r_{vj}, r_{di}) U_{inc}(r_{vj}, r_{si})]_{M \times N_L}$ and $W_B = [-1/_D G(r_{vk}, r_{di}) U_{inc}(r_{vk}, r_{si})]_{M \times N_B}$ are weight matrices for the lesion volume and the background volume, respectively; $[M_L] = [\int_{1_L} \Delta\mu_a(r') d^3 r, \ldots \int_{N_L} \Delta\mu_a(r') d^3 r']$ and $[M_B] = [\int_{1_B} \Delta\mu_a(r') d^3 r', \ldots \int_{N_B} \Delta\mu_a(r') d^3 r']$ are the total absorption distributions of the lesion volume and the background volume, respectively.

Instead of reconstructing the $\Delta\mu_a$ distribution directly as the standard Born approximation, we reconstruct total absorption distribution M and then divide the total by different voxel sizes of lesion and background tissue to obtain $\Delta\mu_a$ distribution. By choosing a finer grid for the lesion and a coarse grid for the background tissue, we can maintain the total number of voxels with unknown absorption on the same scale of the total measurements. As a result, the inverse problem is less underdetermined and ill-posed. In addition, since the lesion absorption coefficient is higher than that of the background tissue, in general, the total absorption of the lesion over a smaller voxel is on the same scale of total absorption of the background over a bigger voxel, and therefore the matrix $[M_L, M_B]$ is appropriately scaled for inversion. The reconstruction is formulated as a least-squares problem. The unknown distribution M can be iteratively calculated with the conjugate-gradient search method.

The lesion location and volume from coregistered ultrasound is estimated as follows: Since the commercial one-dimensional ultrasound probe that we use acquires two-dimensional ultrasound images in the y–z plane (z is the propagation direction) and the two-dimensional NIR probe provides three-dimensional images, the coregistration is limited to an interception plane. However, if we approximate a lesion as an ellipsoid, we are able to estimate its center and radii from two orthogonal ultrasound images and therefore obtain the lesion volume. Three sources of error may

lead to inaccurate estimation of the lesion center and radii and therefore to cause errors in reconstructed optical properties. First, the lesion boundaries may not be well defined in ultrasound images. Second, two separate orthogonal ultrasound images are used to estimate the radii and the center, and these parameters depend on the ultrasound probe position and compression of the hand-held probe. Third, the target volumes or shapes seen by different modalities may be different because of different contrast mechanisms. In the second step, we refine image reconstruction by perturbing the center c_0 and then the radii r_0 and choosing the optimal set of parameters (c_{opt}, r_{opt}).

Clinical studies were performed at the Health Center of the University of Connecticut, and the human subject protocol was approved by the Health Center IRB committee. Patients with palpable and nonpalpable masses that were visible on clinical ultrasound were used as subjects. These subjects were scanned with the combined probe, and ultrasound images and optical measurements were acquired at multiple locations, including the lesion region that was scanned at two orthogonal positions, and a normal region of the contralateral breast scanned at two orthogonal positions.

An example is given in this Letter to demonstrate the use of our reconstruction scheme. Figure 2(a) shows a gray-scale ultrasound image of a palpable lump in a 44-year-old woman. The lesion was located at the 6 to 8 o'clock position of the left breast at approximately 1.5-cm depth. Ultrasound showed an irregular poorly defined hypoechoic mass, and the lesion was considered highly suspicious for malignancy. An ultrasound guided-core needle biopsy was recommended. Biopsy results (after NIR imaging) revealed that the lesion was a high-grade *in situ* ductal carcinoma with necrosis.

Multiple optical measurements at two orthogonal positions were simultaneously made with ultrasound images at the lesion location as well as at approximately the same location of the contralateral normal breast. The fitted average tissue background measured on the normal side of the breast at both wavelengths was $\overline{\mu}_a^{780} = 0.03$ cm^{-1}, $\overline{\mu}_a^{830} = 0.05$ cm^{-1}, $\overline{\mu}_s'^{780} = 9.22$ cm^{-1}, and $\overline{\mu}_s'^{830} = 7.58$ cm^{-1}. The perturbations for both wavelengths used to calculate absorption maps were normalized as $U_{sc}'(r_{si}, r_{di}, \omega) = [U_L(r_{si}, r_{di}, \omega) - U_N(r_{si}, r_{di}, \omega)] U_B(r_{si}, r_{di}, \omega)/U_N(r_{si}, r_{di}, \omega)$, where $U_L(r_{si}, r_{di}, \omega)$ and $U_N(r_{si}, r_{di}, \omega)$ were measurements obtained from the lesion region and the contralateral normal region, respectively, and $U_B(r_{si}, r_{di}, \omega)$ was the incident field calculated with fitted background $\overline{\mu}_a$ and $\overline{D} = 1/3\mu_s'$. This procedure cancels unknown system gains associated with different sources and detectors as well as electronic channels. The initial estimates of the lesion center and diameter in two orthogonal ultrasound images were $(0, 0.39$ cm, 1.7 cm$)$ and 3.44 cm $\times 4.38$ cm $\times 1.76$ cm, respectively. A finer grid of 0.5 cm $\times 0.5$ cm $\times 0.5$ cm and a coarse grid of 1.5 cm $\times 1.5$ cm $\times 1.0$ cm were chosen for the lesion and background tissue, respectively. The total reconstruction volume was chosen to be 9 cm $\times 9$ cm $\times 4$ cm,
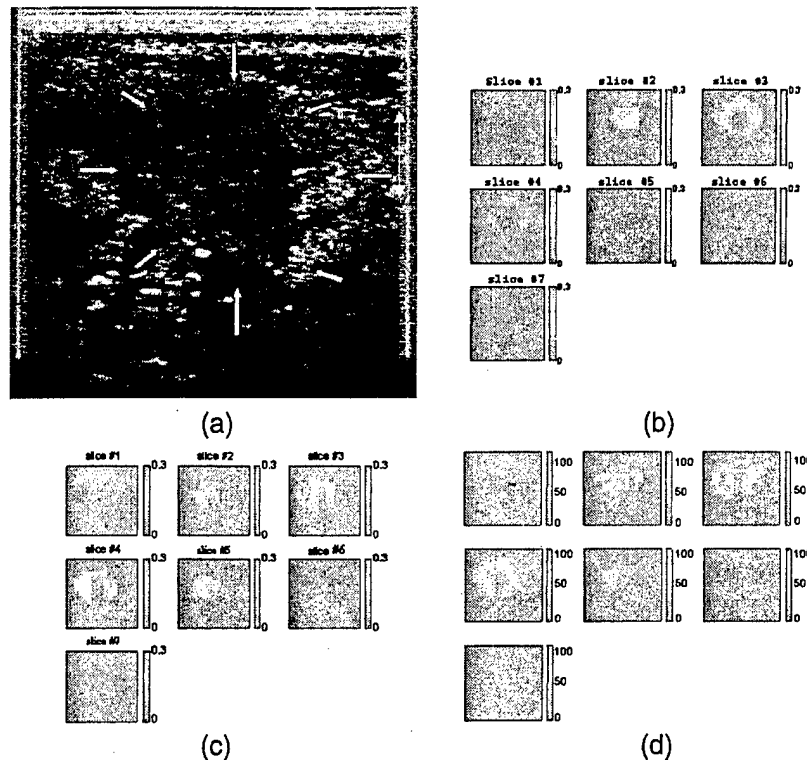
Fig. 2., (a) Gray-scale ultrasound image of a palpable lump of a 44-year-old woman. Ultrasound showed an irregular poorly defined hypoechoic mass, and the lesion was considered as highly suspicious for malignancy. Reconstructed optical absorption maps at (b) 780 nm and (c) 830 nm. The vertical color bars are the absorption coefficient [cm^{-1}]. (d) Total hemoglobin concentration map. The vertical color bars are μmol. The NIR data were simultaneously acquired with the ultrasound image shown in (a). Each image consists of seven slices obtained in 0.5-cm spacing from 0.5 to 3.5 cm in depth. The vertical and horizontal axes correspond to x and y dimensions of 9 cm by 9 cm.

and the total number of voxels with unknown optical absorption was 190, which was of the same order as the 192 total measurements. Image reconstruction was performed with the NIR data simultaneously acquired with the ultrasound image shown in Fig. 2(a). The second-step refined reconstruction revealed optimal lesion centers at approximately $(-1.1$ cm, 0.3 cm, 1.7 cm) for 780 nm and $(-0.9$ cm, -0.7 cm, 1.7 cm) for 830 nm and optimal diameters of 4.28 cm $\times$ 5.18 cm $\times$ 1.96 cm. The detailed absorption maps with high absorption nonuniformly distributed around the lesion boundaries at both wavelengths are shown in Figs. 2(b) and 2(c). By assuming that the major chromophores are oxygenated (oxyHb) and deoxygenated (deoxyHb) hemoglobin molecules in the wavelength range studied, we can estimate the distribution of total hemoglobin concentration as shown in Fig. 2(d). The measured average cancer and background total hemoglobin concentrations were 55.8 μmol and 20.7 μmol, respectively.

It is interesting to note that the absorption distributions at both wavelengths as well as the total hemoglobin concentration were distributed heterogeneously at the cancer periphery. To the best of our knowledge, such fine distributions have not been obtained by use of NIR-only reconstruction techniques. However, this finding agrees with the published literature showing that breast cancers have higher blood volumes than nonmalignant tissue because of angiogenesis, especially at the cancer periphery. In addition, the carcinoma reported here had a necrotic core, which could lead to the low absorption observed at both wavelengths in the center region.

References

1. B. Tromberg, N. Shah, R. Lanning, A. Cerussi, J. Espinoza, T. Pham, L. Svaasand, and J. Butler, Neoplasia **2**, 26 (2000).
2. B. Pogue, S. P. Poplack, T. O. McBride, W. A. Wells, K. S. Osterman, U. Osterberg, and K. D. Paulsen, Radiology **218**, 261 (2001).
3. Q. Zhu, T. Durduran, M. Holboke, V. Ntziachristos, and A. Yodh, Opt. Lett. **24**, 1050 (1999).
4. N. G. Chen, P. Y. Guo, S. K. Yan, D. Q. Piao, and Q. Zhu, Appl. Opt. **40**, 6367 (2001).
5. P. Vaupel, F. Kallinowski, and P. Okunieff, Cancer Res. **49**, 6449 (1989).

Imaging heterogeneous tumor angiogenesis distributions of advanced breast cancers by optical tomography with ultrasound localization

Quing Zhu*, Scott H. Kurtzman+, Poornima Hegde+, Minming Huang*, NanGuang Chen*, Bipin Jagjivan+, Mark Kane+, Kristen Zarfos+

*University of Connecticut
371 Fairfield Rd, U1157
Storrs, CT 06269

+University of Connecticut Health Center
263 Farmington, CT 06030

Correspondence: Prof. Quing Zhu
Bioengineering Program, Electrical Engineering Department
University of Connecticut
Storrs, CT 06269
Phone: 860-486-1815; Fax:860-486-1273
e-mail:zhu@engr.uconn.edu

Abstract

In this paper, we report high-resolution identification of angiogenesis distributions of advanced breast cancers imaged by a novel hybrid optical and ultrasound imaging technique. The hybrid technique deploys near-infrared (NIR) optical imaging sensors and a commercial ultrasound transducer on a hand-held probe. The ultrasound transducer is used for lesion localization and the optical sensors are used for imaging tumor angiogenesis. Preliminary results of four advanced cancer cases have shown correlation between cancer angiogenesis distributions and histological microvessel density counts.

Introduction

Noninvasive in vivo breast imaging at the molecular level presents a unique challenge . Optical tomography using near infrared diffused light has a great potential for monitoring tumor angiogenesis development, a key factor required for tumor growth and metastasis. This method also provides insight into tumor metabolism and tumor hypoxia, an important indicator of tumor response to various forms of therapy (1-5). These functional parameters are highly relavant for assessing tumor response to treatment as well as for diagnosis. However, optical tomography when used alone has been limited to laboratory tests and feasibility studies in the past. The fundamental problem remains the intense light scattering in tissue, which makes the localization of lesion difficult. A novel ultrasound guided optical imaging technique has shown promising results of overcoming the diffusive light localization problem in tissue (6-8). The technique is implemented by simultaneously deploying optical sensors and a commercial ultrasound transducer on a hand-held probe, and utilizing co-registered lesion structure information provided by ultrasound to improve the inverse optical imaging reconstruction. Preliminary results have shown that early stage invasive breast cancers present two-fold high total hemoglobin concentration than a group of fibroadenomas and benign lesions (9).

Tumor angiogenesis distribution of advanced cancers is highly heterogeneous (7). This is related to the complex angiogenesis process involving both the incorporation of existing host blood vessels into tumor and the creation of tumor microvessels. This process is modeled by angiogenesis factors (10). Blood flow through these tumor vessels is heterogeneous. Some areas have high flow, others have slower flow and develop necrosis (10). Tumors with relatively poor blood perfusion may not receive adequate delivery of systemic therapy. This lack of perfusion may be a factor in poor response to intravenous

chemotherapy treatment in some patients (11). Although pilot studies of imaging tumor angiogenesis have been conducted with optical tomography, no one has obtained high-resolution heterogeneous angiogenesis distributions in advanced cancers. In this paper, we report what we believe the first heterogeneous angiogenesis distributions of large cancers imaged by optical tomography. We also show that the angiogenesis distributions correlate, to a large extent, to histological microvessel density counts.

2.   Materials and Methods

A hand-held hybrid probe consists of a commercial ultrasound transducer located at the middle and near-infrared source-detector fibers distributed at the periphery. The picture of the probe and its dimensions are shown in Fig.1. The technical aspects of the NIR imager have been described in detail previously (8). Briefly, the imager consists of 12 pairs of dual wavelength (780nm and 830nm) laser diodes, which are used as light sources, and their outputs are coupled to the probe through optical fibers. On the receiving side, 8 photomultiplier tubes (PMTs) were used to detect diffusely scattered light from the tissue and 8 optical fibers were used to couple detected light to the PMTs. The laser diodes' outputs were amplitude modulated at 140 MHz and the detector outputs were demodulated to 20KHz. The demodulated signals were further amplified and band pass filtered at 20 KHz. A reference signal of 20 KHz was also generated by directly mixing the detected RF signals with the RF signal generated from the oscillator. The reference signal was necessary for retrieving phase shifts. Eight detection signals and one reference were sampled and acquired into a PC simultaneously. The entire data acquisition took about 3 to 4 seconds, which was fast enough for acquiring data from patients.

The details of our dual-mesh optical imaging reconstruction algorithm have been described in Ref (9). Briefly, the NIR reconstruction takes advantages of ultrasound localization of lesions and segments the imaging volume into finer grid in lesion region and coarser grid in non-lesion regions. A modified Born

approximation is used to relate the scattered field measured at the source-detector pairs to absorption variations in each volume element of two regions within the sample. With this dual-mesh scheme, the inverse optical reconstruction is well-conditioned and converges in few iterations.

Clinical studies were performed at the University of Connecticut Health Center (UCHC). The UCHC IRB committee approved the human subject protocol. Patients with palpable and non-palpable masses that were visible on clinical ultrasound and who were scheduled for biopsy were enrolled as research subjects. Ultrasound images and optical measurements were acquired simultaneously at multiple locations including the lesion region scanned at two orthogonal positions, a normal region of the same breast if the breast was large, and a normal symmetric region of the contralateral breast scanned at two orthogonal positions. The optical data acquired at normal region were used as reference for calculating the scattered field caused by lesions.

Of patients studied so far, four cases presented with advanced breast cancers; tumor sizes ranging from T2 to T4. One patient received chemotherapy for three months before surgery, and the other three have received definitive surgery. To correlate the imaged angiogenesis distribution with histology microvessels density, we have performed microvessel density counts. Samples obtained at surgical biopsy or breast-conservation surgery were used for counting. For each sample, sections 3 to 5 micrometer thick were stained on an immunohistochemistry slide staining system (DAKO autostainer) with factor 8/86 mouse monoclonal antibody (anti-human von Willebrand factor, DAKO Corp, Carpinteria, Calif) at 1:100 dilution digested by proteinase K for 3 minutes, by labeled polymers (DAKO EnVision plus) immunoperoxidase method. The microvessel density counts were performed in ten consecutive fields with the use of an ocular grid at X200 magnification. The first field chosen was a

hotspot (area of maximum vascular density either within the infiltrating tumor mass or at the tumor-stromal interface). Since the cancers were large, two to three separate sample blocks were selected for microvessel counts as per the specimen orientation in the surgical pathology report.

3. Results

During the diagnostic imaging study, we scanned a patient who was undergoing chemotherapy. This 44-year-old woman had a large 4 cm x 4 cm x 1.5 cm palpable mass (Fig.2 (a)) located at the 6 to 8 o'clock position of the left breast that was considered as highly suspicious for malignancy. The lesion center was approximately 1.5 cm in depth relative to the skin. An ultrasound guided needle biopsy revealed that the lesion was a high-grade invasive carcinoma with necrosis. Optical absorption maps of both wavelengths are shown in Fig. 2(b) and (c) and the distributions are highly heterogeneous with high absorption at the cancer periphery. Slice 1 is the spatial x-y image of 9 cm x 9 cm obtained at 0.5 cm deep from the skin surface. Slice 7 is 3.5 cm deep toward the chest wall and the spacing between slices is 0.5 cm. The total hemoglobin concentration map is shown in Fig.2 (d) and the maximum and average hemoglobin concentrations are 92.1 ? moles and 26.2 ? moles. The measured maximum absorption coefficients at 780 nm and 830 nm are 0.17 cm^{-1} and 0.22 cm^{-1}, respectively. Since this cancer was too large for breast conserving surgery, the patient was treated with chemotherapy in the neo-adjuvant setting for three months. At the time the patient completed the chemotherapy, we imaged her again with the combined US and NIR probe. Figure 3 (a) is the ultrasound image of the cancer three month later. The cancer contrast is poor and cancer boundaries are completely unclear, probably due to treatment. Figure 3 (b) and (c) are optical absorption maps at both wavelengths and (d) is the total hemoglobin distribution. The maximum and average hemoglobin concentrations of the lesion are 79.8 ? moles and 24.9 ? moles, respectively. The measured maximum absorption coefficients at 780 nm and 830 nm are

0.15 cm^{-1} and 0.19 cm^{-1}, respectively. Compared with the images acquired before treatment, the spatial extension of the angiogenesis pattern is much smaller and more confined to the core area. The maximum total hemoglobin concentration is reduced by about 10 ? moles and the average is about the same as before. This example demonstrates the feasibility of monitoring the treatment using the combined technique.

To correlate the NIR images with microvessel densities, we selected three block samples obtained at breast-conservation surgery marked as anterior, lateral and posterior (see Fig. 3 insertion) for microvessel counting. The total number of microvessels were 196 (lateral), 114 (anterior) and 48 (posterior and inferior) per 10 consecutive fields at 200 magnification, respectively (see table I: ID#19). The high counts obtained at anterior and lateral correlate with the high optical absorption and total hemoglobin concentration shown in slice 3 of Fig.3 (b)-(d). A representative section demonstrating high microvessel density is shown in Fig.3 (e). The low counts obtained at posterior and inferior block sample correlate with the low optical absorption as well as the low hemoglobin concentration seen in deeper slices 4 and 5 of Fig. 3(a)-(c).

The second imaging example was obtained from a 47-year-old woman who had a 3 cm x 3 cm x 2 cm dominant mass at the 2 o'clock position in her left breast. The lesion center was about 2.3 cm in depth relative to the skin. Ultrasound showed hypoechoic mass with irregular margins (see Fig. 4(a)) and the lesion was considered as highly suspicious for malignancy. Figure 4 (b) and (c) are optical absorption maps obtained at 780 nm and 830 nm and the vertical scale of (b) and (c) is half of that used in Fig.3 (b) and (c). Figure 4(d) is the total hemoglobin concentration distribution and the vertical scale is the same as that used in Fig. 3(d). The light absorption at both wavelengths is much lower than the previous example but the distributions are highly heterogeneous. The measured maximum absorption

coefficients at 780 nm and 830 nm are 0.08 cm^{-1} and 0.10 cm^{-1}, respectively. The measured maximum total hemoglobin concentration of the tumor and average of the lesion are 40.6 ? moles and 17.2 ? moles, respectively. Surgical pathology report revealed that the mass was an infiltrating carcinoma (histological grade II, nuclear grade II) with low mitotic activity. The total counts of microvessels obtained from anterior and posterior core biopsy samples were 61 and 40 per 10 consecutive fields at 200 magnification, respectively (see Table I: ID#5). The total counts measured from anterior and posterior tumor samples were 52 and 29, respectively. These low counts correlate well with the low optical absorption shown in Fig. 4 (b)-(c) and indicate that the tumor was poorly perfused. A representative section demonstrating low microvessel density is shown in Fig.4 (e).

Since our hand-held probe can be easily rotated or translated, we have acquired at least three co-registered ultrasound and NIR data sets at the lesion location for each patient and reconstructed corresponding optical absorption maps as well as the total hemoglobin concentration distribution under the co-registered ultrasound guidance. The measurements shown in Table II are average values taken over three images. The maximum absorption coefficient, the average absorption coefficient within the hot area defined as within 6 dB of the maximum value, the ratio of average absorption coefficient inside the lesion over the hot area, the maximum total hemoglobin concentration, the average total hemoglobin concentration inside the lesion, are all given in Table II. The ratio of average absorption coefficient inside the lesion over the hot area partially reflects the angiogenesis heterogeneity.

The third patient (Table I: ID#23) was a 33-year-old pregnant woman who had palpable left breast lump at 12'clock position measuring 3 cm x 3cm x 1.5 cm. The ultrasound image showed that the lesion had discrete nodularity (see Fig. 7(a)). The center of the lump was about 2.5 cm deep from the skin. An

ultrasound guided core biopsy was obtained and revealed that the lesion was both *in situ* and invasive ductal carcinoma as seen on multiple cores (histologic grade III, nuclear grade III). Optical absorption maps as well as total hemoglobin concentration map were obtained 8 days after core biopsy at the time of the patient visit (see Fig.5 (b)-(c)). The measured average maximum absorption coefficients at 780 nm and 830 nm are 0.15 cm^{-1} and 0.33 cm^{-1}, respectively (Table II: ID#23). The maximum total hemoglobin concentration of the tumor is 113.0 ? moles and the average is 24.5 ? moles. As seen from Table II, the standard deviation of maximum total hemoglobin concentration measured from different probe positions is 21? moles, which is much larger than those obtained from other cases. Since the optical imaging was performed eight days after core biopsy and possible hemoglobin changes due to a host response at biopsy sites could not be ruled out.

Histological microvessel counts of three sample blocks were 60 (anterior/lateral), 88(anterior/medial), and 152 (posterior and inferior) per 10 consecutive fields at 200 magnification, respectively. The larger variation in total counts at different tumor locations is partially related to the inherent heterogeneity of breast tumors and the resulting misdistribution of angiogenesis in the viable and schirrous regions. Nevertheless, the relatively higher counts obtained at anterior/lateral, anterior/medial correlate to some extent to the high optical absorption and total hemoglobin distribution seen in slice 4 of Fig. 5(b)-(d). The high counts obtained in the posterior and inferior sample do not correlate with the low optical absorption distribution seen by optical imaging in deeper slices. The reason for this discrepancy is explained in the following section.

The last example was obtained from a 53-year old woman who had a palpable mass, but a normal - mammogram. An ultrasound obtained revealed an irregularly shaped lesion of 2 cm x 2 cm x 1.3 cm

and ultrasound guided surgical biopsy confirmed an invasive and *in situ* ductal carcinoma (histological grade II, nuclear grade II). The lesion center was about 2.5 cm in depth relative to the skin. Optical absorption maps as well as the total hemoglobin concentration distribution were obtained. The measured maximum absorption coefficients at 780 nm and 830 nm are 0.20 cm^{-1} and 0.29 cm^{-1} (Table II: ID#21), respectively. The maximum total hemoglobin concentration of the tumor is 114.8 ? moles and the average is 20.9 ? moles. The total number of microvessels were 83 (anterior), 121 (posterior and lateral), 124 (posterior) per 10 consecutive fields at 200 magnification, respectively. The higher anterior and lateral counts correlate with the high optical absorption and high total hemoglobin concentration. Similar to the third example, the higher posterior counts do not correlate with the low light absorption and low hemoglobin concentration seen in deeper slices.

4. Discussion and Summary:

Reflection geometry is used for optical tomography because optical source and detector fibers can be easily integrated with a hand-held ultrasound probe. For deeply located, highly absorbing tumors, such as the third and fourth examples, the diffusely reflected photon density waves from the bottom of the tumor are weak when they reach the detectors. Therefore, the perturbations from the deeper part of the tumor are much weaker compared with perturbations from the top part of the tumor. As a result, the reconstructed images show higher absorption at top and lower absorption at the bottom. For the poorly perfused case (Fig.4), the light absorption of the cancer was not high and the lesion was imaged more uniformly from top to bottom. This depth dependent distribution imaged by diffused wave may be minimized by increasing the detection sensitivity and appropriately scaling the weight matrix for imaging reconstruction. Currently, we are pursuing investigations along this direction.

For the large cancers presented here, ultrasound can accurately diagnose the malignancy. The value of the optical tomography is to estimate tumor perfusion and evaluate treatment efficacy by providing angiogenesis maps as well as tumor hypoxia during the chemotherapy. This type of information could prove invaluable in determining whether or not the tumors are chemosensitive. Tumor hypoxia which can also be measured is related to tumor growth rate, drug response etc (12). In principle, the distribution of oxygenation saturation can be estimated from absorption maps at the two wavelengths of 780 nm and 830 nm. However, since background tissue mainly consists of water and lipid and these two chromophores contribute to the total absorption estimate as well, we could not obtain reasonable background oxygenation saturation and compare it with lesion oxygenation saturation. One or two more wavelengths will allow us to accurately estimate the background oxygenation saturation and to compare it with lesion oxygenation saturation.

In this paper, we have reported initial results of heterogeneous angiogenesis distributions of four average size cancer cases imaged by optical tomography with ultrasound localization. The angiogenesis maps correlate, to a large extent, to the histological microvessel density counts. These initial results are exciting and suggest that imaging with optical tomography at molecular level is feasible.

References:

[1] Tromberg B, Shah N, Lanning R, Cerussi A, Espinoza J, Pham T, Svaasand L, and Butler J (2000). Non-Invasive in vivo characterization of breast tumors using photon migration spectroscopy. Neoplasia vol.2, No 1:2: 26-40.

[2] Ntziachristos V, Yodh A, Schnall M., and Chance B (2000). Concurrent MRI and diffuse optical tomography of breast after indocyanine green enhancement. Proc. of Nat. Ac. of Sci., 97 (6), 2267-2772.

[3] Franceschini MA, Moesta KT, Fantini S, Gaida G, Gratton E, Jess H, Seeber M, Schlag PM, Kashke M (1997). Frequency-domain techniques enhance optical mammography: initial clinical results. Proc. of Nat. Ac. of Sci., 94: 6468-6473.

[4] Pogue B, Poplack SP, McBride TO, Wells WA, Osterman K, Osterberg U, and Paulsen KD (2001). Quantitative hemoglobin tomography with diffuse near-infrared spectroscopy: pilot results in the breast. Radiology, 218: 261-266.

[5] Jiang H, Xu Y, Iftimia N, Eggert J, Klove K, Baron L and Fajardo L (2001). Three-dimensional optical tomographic imaging of breast in a human subject. IEEE Trans on Medical Imaging, 20(12), 1334-1340.

[6] Zhu Q, Dunrana T, Holboke M, Ntziachristos V and Yodh A(1999). Imager that combines near infrared diffusive light and ultrasound. Optics Letters, **24**(15), 1050-1052.

[7] Zhu, Q., Chen NG, Kurtzman, S, "Imaging tumor angiogenesis using combined near infrared diffusive light and ultrasound," Optics Letters, **28** (5), 337-339,2003.

[8] Chen, NG, Guo, PY, Yan, SK, Piao DQ, and Zhu, Q., "Simultaneous near infrared diffusive light and ultrasound imaging," Applied Optics, December, Vol.40, No.34, 6367-6380, 2001

[9] Zhu, Q., Huang, MM, Chen, NG, Zarfos, K, Jagjivan, B, Kane, M, Hegde P Kurtzman, SH, "Ultrasound-guided optical tomographic imaging of malignant and benign breast lesions: initial clinical results of 19 cases" Neoplasia, Accepted.

[10] Vaupel P, Kallinowski F, Okunieff P (1989). Blood flow, oxygen and nutrient supply, and metabolic microenvironment of human tumors: a review. Cancer Research 49, 6449-6465, 1989

[11] Jain RK. Haemodynamic and transport barriers to the treatment of solid tumors. Int J Radiat Biol. 1991; 60:85–100.

[12] Vaupel P, Schlenger K, Knoop C, Hockel M, "Oxygenation of human tumors: evaluation of tissue oxygen distribution in breast cancers by computerized O2 tension measurements," Cancer Research, 51:3316-3322 (1991).

14

Figure Captions:

Figure 1. (a) The hand-held probe with ultrasound transducer located in the middle and optical sources and detectors distributed at the periphery. (b) Optical source and detector distribution.
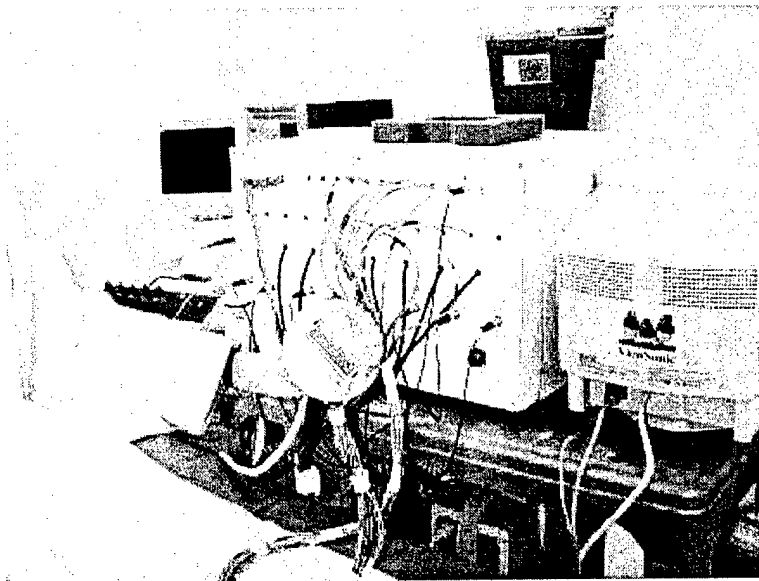
Figure 2. (a) Ultrasound image of a 44-year-old woman who had a large 4 cm by 4cm palpable left breast mass. (b) Optical absorption map at 780 nm. (c) Optical absorption map at 830 nm. (d) Total hemoglobin concentration of the lesion.

Figure 3 (ID#19P10). (a) Ultrasound image of the cancer treated with chemotherapy for three months. (b) Optical absorption map at 780 nm. (c) Optical absorption map at 830 nm. (d) Total hemoglobin concentration of the lesion. (e) Representative section of the infiltrating ductal carcinoma of breast (ID#19) demonstrating high microvessel density (original magnification X200; anti-human von Willebrand factor, DAKO EnVision plus).
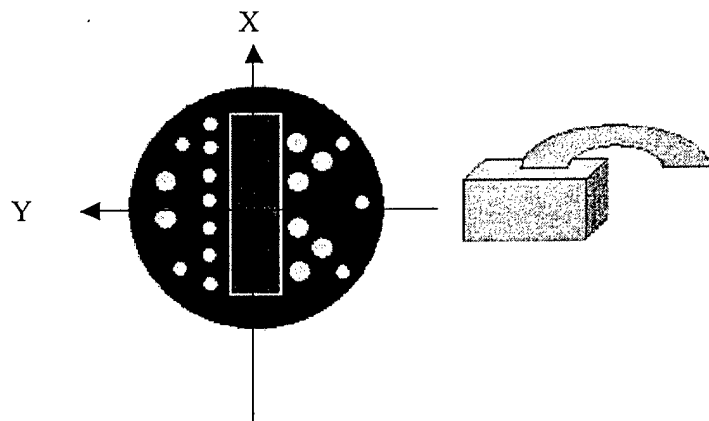
Figure 4(ID#5P4). (a) Ultrasound image of a 47-year-old woman with a highly suspicious lesion located at 2'oclock position of her left breast. (b) Optical absorption map at 780 nm. (c) Optical absorption map at 830 nm. Note the scales for Fig. 4(b) and (c) is half of that used in Fig. 3(b) and(c). (d) Total hemoglobin concentration of the lesion. The scale is the same as the Fig.3 (d). (e) Representative section of infiltrating ductal carcinoma of breast (ID#5, Fig.7) demonstrating low microvessel density (original magnification X200; anti-human von Willebrand factor, DAKO EnVision plus).

Figure 5 (ID#23P7). (a) Ultrasound image of a 33-year-old woman with a highly suspicious lesion at 12'clock position measuring 3 cm x 3cm x 1.5 cm, and the ultrasound showed that the lesion had

discrete nodularity. Ultrasound image cannot clearly identify the lesion sue the acoustic heterogeneous of tissue at pregnancy. (b) Optical absorption map at 780 nm. (c) Optical absorption map at 830 nm. (d) Total hemoglobin concentration of the lesion.
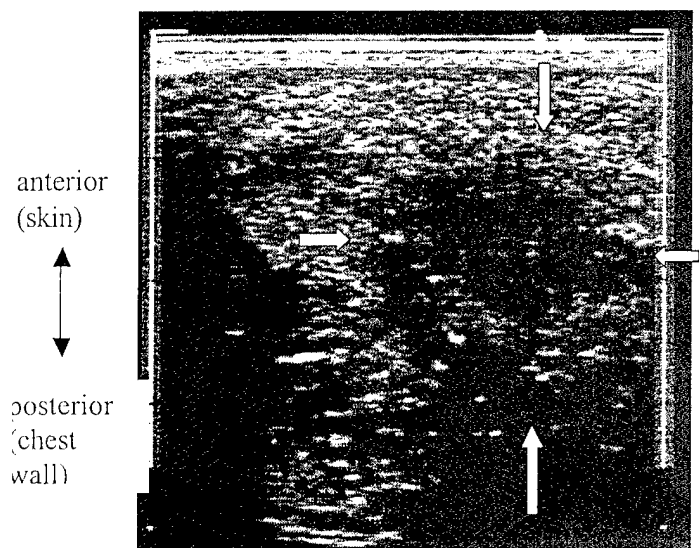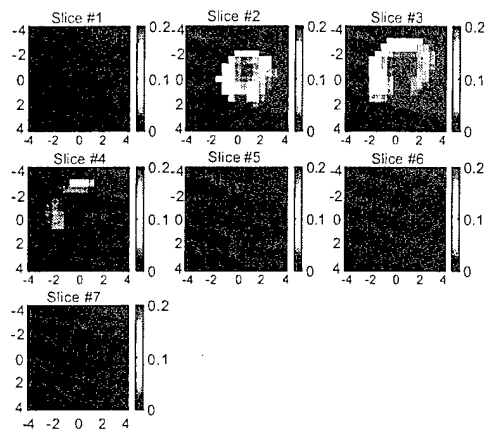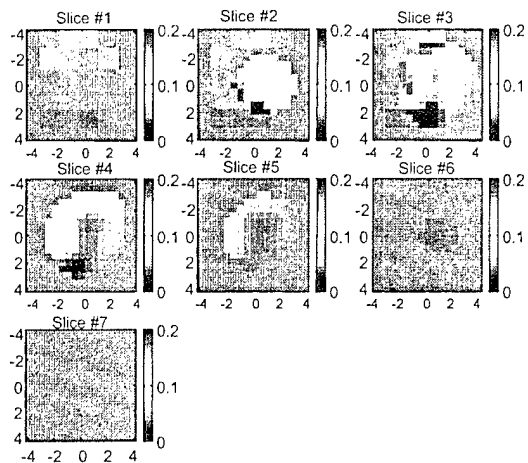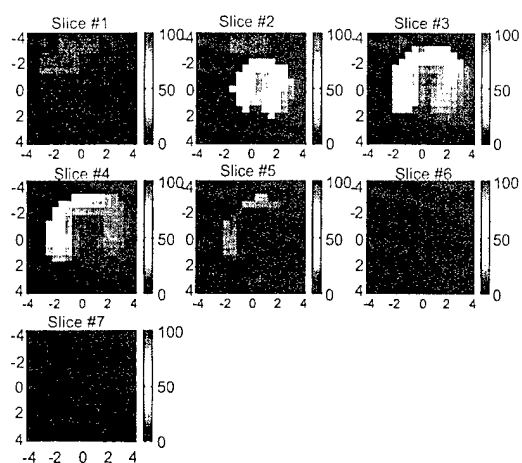
(a)

(b)

Fig.1.

anterior
(skin)
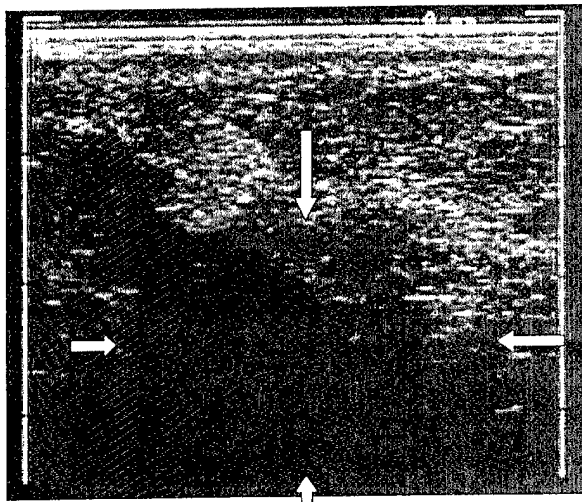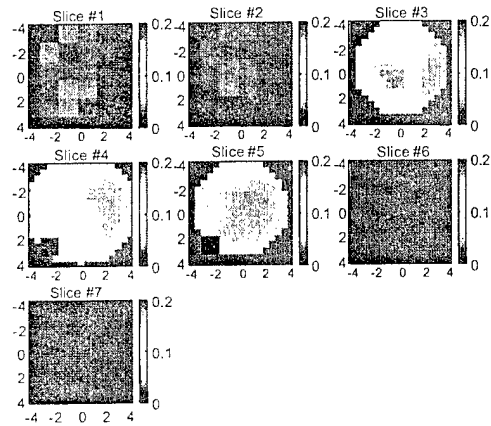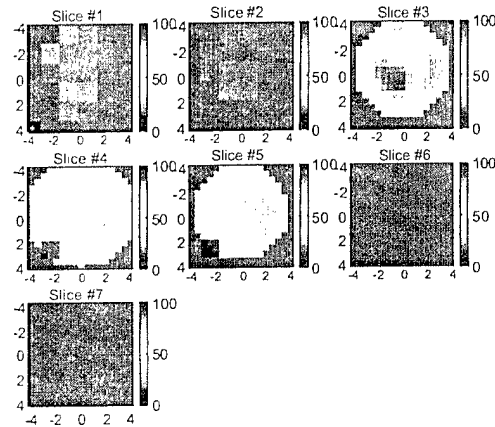
posterior
(chest
wall)

(a)

(b)

(c)
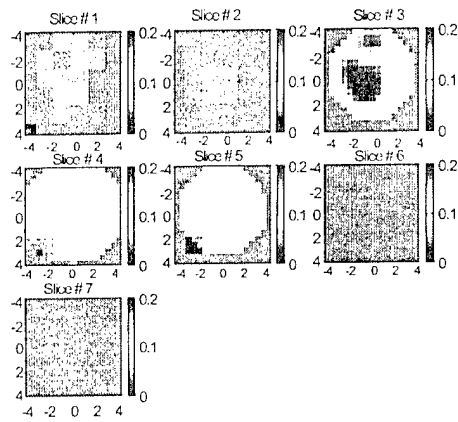
(d)

Figure 2

(a)

(b)

(c)

(d)

(e)

Figure 3

(a)

(b)

(c)

(d)

(e)

Figure 4.

(a)

(b)

(c)

(d)
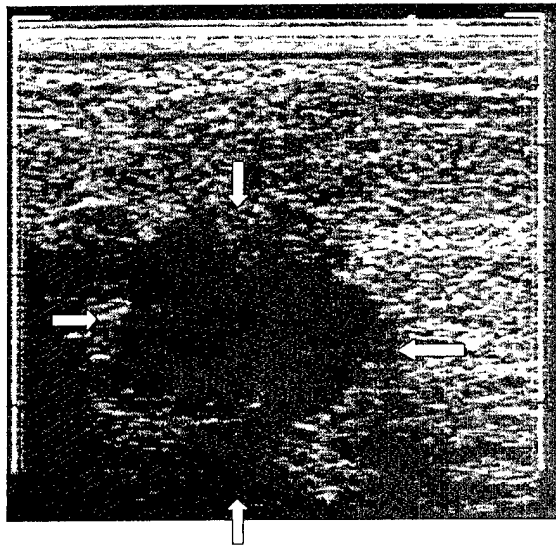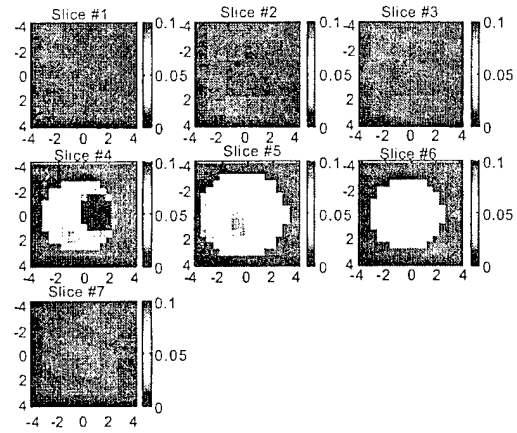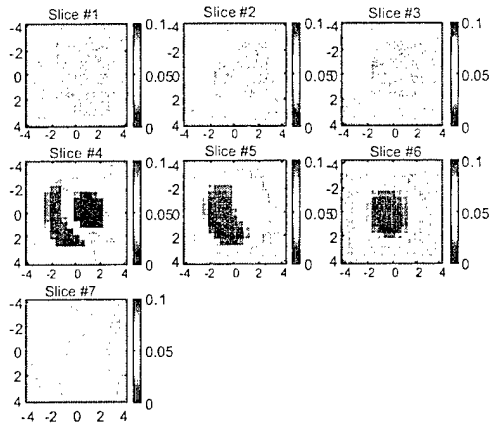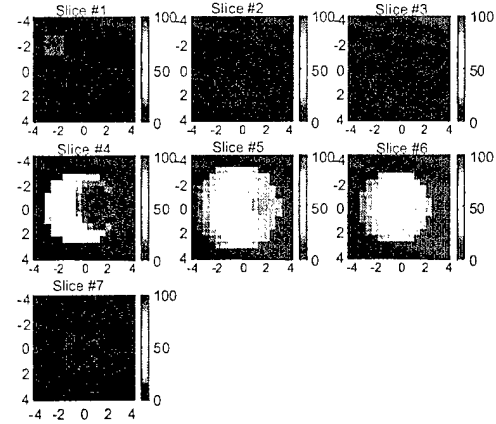
Figure 5.

Table I. Histological microvessel density counts

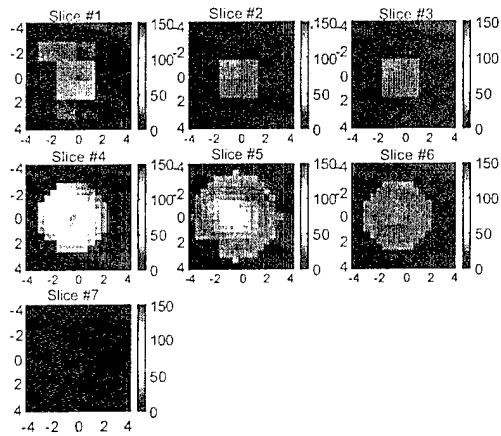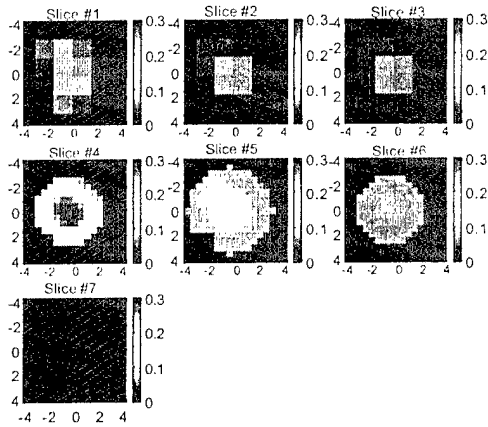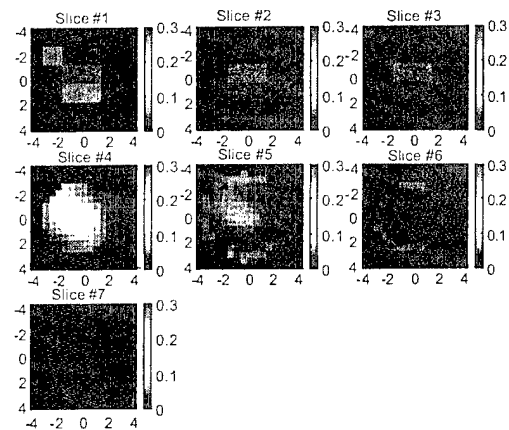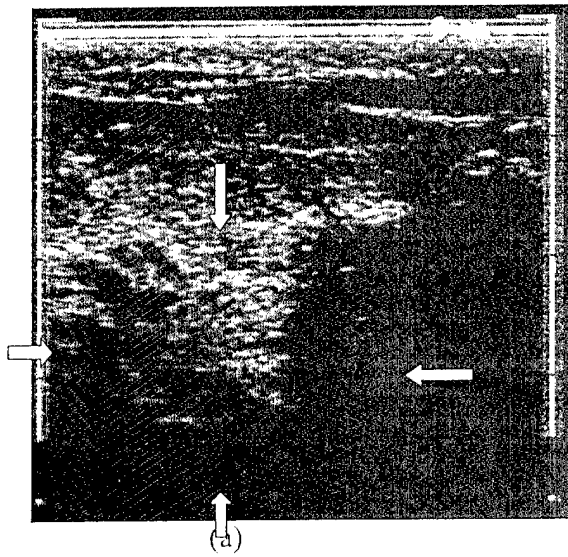| ID#	core bx #	block #	location	mvd/10 200x	lumpx #	block #	location	mvd/10 200x
ID#19	NONE	NA	NA	NA	S02-7823	B2	LATERAL	196
	NONE	NA	NA	NA	S02-7823	B6	ANTERIOR	114
	NONE	NA	NA	NA	S02-7823	B8	POST/INF	48
ID#5	S01-5578	A1	12 - ANT	61	S02-392	A4	ANT	52
	S01-5578	C1	6 - POST	40	S02-392	A2	POST	29
ID#23	NONE	NA	NA	NA	S02-4024	A3	POST/INF	152
	NONE	NA	NA	NA	S02-4024	A4	ANT/LAT	60
	NONE	NA	NA	NA	S02-4024	A6	ANT/MED	88
ID#21	NONE	NA	NA	NA	S02-4299	A3	POST/LAT	121
	NONE	NA	NA	NA	S02-4299	A2	POST	124
	NONE	NA	NA	NA	S02-4299	A1	ANT	83

Table II. Optical measurements

ID#	max μ_a cm^{-1} (780 nm)	ave.6dB μ_a cm^{-1} (780 nm)	aveL/ave.6dB. (780 nm)	max μ_a cm^{-1} (830 nm)	ave.6dB μ_a cm^{-1} (830 nm)	aveL/ave.6dB (830 nm)	max total Hb μ moles	ave. Hb μ moles
ID#19	0.16 (0.01)	0.11(0.01)	33.7%	0.18(0.004)	0.13(0.006)	50.2%	80.6(2.4)	24.1(1.1)
ID#5	0.08 (0.01)	0.05 (0.01)	56.7%	0.10 (0.01)	0.06 (0.01)	67.4%	44.0(5.3)	17.2(1.1)
ID#23	0.16 (0.01)	0.11 (0.01)	21.1%	0.33 (0.07)	0.24(0.05)	29.8%	113.0(21.4)	24.5 (2.4)
ID#21	0.20(0.01)	0.15 (0.01)	16.7%	0.29(0.01)	0.21 (0.01)	30.5%	114.8 (5.1)	20.9 (0.7)

Appendix E

Time-resolved optical measurements with spread spectrum excitation

Nan Guang Chen and Quing Zhu

Department of Electrical and Computer Engineering, University of Connecticut, Storrs, Connecticut 06269

We propose a novel method for measuring time-dependent optical quantities. A train of excitation pulses modulated by a pseudorandom bit sequence is used as the light source, and a cross-correlation scheme is used to retrieve the impulse response. Simulation results of the temporal point-spread function of a diffusive wave are provided, as well as experimental results of a fluorescence decay profile. It is demonstrated that our new time-resolved technique can lead to high signal-to-noise ratios and short data acquisition times. A fluorescence-time-dependent suppression process was also been discovered. © 2002 Optical Society of America

OCIS codes: 170.3650, 170.6920, 170.5280, 170.6280.

Time-resolved techniques are important in optical instrumentation. Measurements of time-dependent transmittance, reflectance, and fluorescence in response to illumination by an impulse of light always contain rich information that can be used to retrieve the dynamics and other properties of the sample under investigation. Time-resolved photon-migration imaging and time-resolved fluorescence spectroscopy and imaging are good examples of such techniques.

Photon-migration imaging has been emerging as a potential clinical diagnostic modality.[1] Conventional time-resolved photon-migration imaging measures temporal point-spread functions (TPSFs), which can be used for quantitative reconstruction of distributions of scattering and absorption coefficients.[2] Accurate measurement of the rising edge of a TPSF, which is related to that quasi-straightforward propagating component, is desirable for improving spatial resolution.[3,4] Time-resolved fluorescence spectroscopy[5] and imaging[6] have been used in a wide range of research areas such as biosciences, chemistry, and clinical diagnosis. The fluorescence lifetime of a chromophore depends on its characteristic internal structure as well as on its physical and chemical environments. Discrimination of signals related to different fluorescence lifetimes has been exploited to suppress background autofluorescence, improve signal-to-noise ratio, achieve high sensitivity and signal specificity, and measure local environmental parameters such as pH, temperature, and ion concentrations. Fluorescence-lifetime imaging microscopy makes it possible to reveal the biomedical processes and reactions within a cell with high spatial resolution. Determination of fluorescence lifetime is generally made in the time domain, in which short excitation pulses are used.

Currently, the temporal profile of the response to an ultrashort light pulse can be measured with either a streak camera or a time-correlated single-photon counting (TCSPC) system. TCSPC is preferred because its dynamic range and temporal linearity are better than those of streak cameras. A few time-resolved systems for medical optical tomography were reported recently, all of which use the TCSPC technique.[7,8] Nonetheless, the principle of single-photon counting requires that

no more than one photon be detected in each cycle. This restriction causes a big problem in data acquisition. The maximal count rate is limited by the repetition rate of laser pulses, the processing speed of electronic devices, and the time span of the impulse response. A typical count rate is 100,000 counts per second, which means that approximately 15–30 are required for acquisition of 10^5–10^6 photons for one temporal profile. In some applications, multiple detection channels are necessary to keep the overall data-acquisition time under control. For example, Schmidt et al. reported on a 32-channel time-resolved instrument that needs 10–20 min for a complete scan.[8] It is worthy of mention that far more photon counts are needed for accurate measurement of the intensity of early-arriving photons.

We propose in this Letter a coded excitation and correlation detection mechanism that borrows ideas from spread-spectrum communications. It is well known that a spread spectrum communication system possesses many desirable properties, such as selective addressing capability, low error rate, and interference rejection.[9] A broadband pseudorandom code has only a weak cross correlation with other codes and an autocorrelation function that is analogous to a delta function. Consequently, a receiving system can pick up the correct code sequence, addressing it from environmental noise and interference, and is able to distinguish the same sequence that arrives at different times from multiple paths. This property is utilized in our time-resolved optical system, in which photons detected at different time delays need to be resolved. Better signal-to-noise ratio, shorter data-acquisition time, and low system cost are the expected advantages of our new technique. Our computer simulations have demonstrated the feasibility of a time-resolved photon-migration imaging system based on spread spectrum excitation. We have also built a primitive time-resolved fluorometer and have conducted a series of experiments with it. The exponential decay profile of a long-lifetime dye was successfully retrieved.

The principle of our method is simple and straightforward. We denote by $I(t)$ the time-dependent response of a sample to the excitation of an ultrashort

pulse. A light source continuously modulated with a pseudorandom bit sequence is used to illuminate the sample. So the ac component in the detected signal is proportional to a convolution of the impulse response and the excitation:

$$R(t) = AI(t) * P(t), \qquad (1)$$

where A is the modulation depth and $P(t)$ is an N-bit-long pseudorandom bit sequence. $P(t)$ is a maximal length sequence, which has a circular auto-correlation function similar to a delta function:

$$
g(\tau) = \langle p(t)p(t - \tau) \rangle
$$
$$
= \begin{cases} 1 & \tau/T_0 = 0 \\ -1/N & \tau/T_0 = 1, 2, \ldots, N/2; \\ & \quad -1, -2, \ldots, \quad -N/2 \end{cases}
$$
$$\qquad (2)$$

in which τ is the time delay and T_0 is the bit period. $g(\tau)$ increases linearly when τ is within $[-T_0, 0]$ and decreases linearly in $[0, T_0]$. In regions out of $[-T_0, T_0]$, the autocorrelation values are essentially zero when N is big enough. By correlating $R(t)$ with $P(t)$ we have

$$f(\tau) = \langle R(t)P(t - \tau) \rangle = I(\tau) * g(\tau). \qquad (3)$$

Equation (3) is valid when the time span of the TPSF is less than NT_0. If T_0 is small enough, $f(\tau)$ at a specific delay time τ is well approximated by $I(\tau)$. When T_0 becomes comparable to the time scale of $I(\tau)$, $g(\tau)$ acts as an equivalent temporal gating window. So the impulse response or its integral over a time window can be retrieved by the correlation method.

Time-resolved measurement of diffusive photon density waves by the spread spectrum approach was simulated on a computer. A simulated photon migration imaging system consisted virtually of a four-channel 12.5-Gbit/s pattern generator (MP1775A, Anritsu), a 10-Gbit/s 850-nm vertical-cavity surface-emitting laser transmitter (1780, New Focus), a 12-GHz receiver (1580-A, New Focus), a light-collecting device that effectively increased the detection aperture to 1 mm^2, and electronic components such as mixers, filters, and amplifiers. A 4095-bit long pseuodrandom bit sequence $p(t)$ ($T_0 = 100$ ps) generated by the pattern generator was used to directly modulate the transmitter to generate an optical pulse sequence with a 1-mW peak-to-valley value. The optical fibers of the transmitter and the receiver were embedded in an infinite homogeneous turbid medium and were separated by 5 cm. The reduced scattering coefficient of the medium was 6 cm^{-1}, and the absorption coefficient was chosen to be 0.02 cm^{-1}. The ideal response of the receiver to a 1-nJ pulse from the transmitter was denoted $V(t)$ and is proportional to the TPSF that can be computed with the diffusion equation. The receiver's response to the pseudorandom normal sequence stimulation was given by

$$M(t) = AV(t) * [P(t) + n_s R_1(t)] + n_d R_2(t), \qquad (4)$$

where $A = 10^{-4}$ and where $R_1(t)$ and $R_2(t)$ were random sequences of normal distribution with a unit standard deviation. Noise levels $n_s = 0.022$ and $n_d = 2$ mV were derived from specifications of the transmitter and the receiver. The correlation can be performed by a mixer (e.g., ZMX-10G from Mini-Circuit) and a low-pass filter. The reconstructed $V(t)$ is compared in Fig. 1 with the original curve. The noise level in the reconstructed temporal profile was $\sim 6.13 \times 10^{-5}$, or 3.2% of the peak value of $V(t)$. Note that fewer than 41 photons could be detected by TCSPC within the same measurement time.

To validate our spread spectrum approach experimentally, we built a time-resolved fluoroscopy system and conducted experiments. The experimental system consists of an ultraviolet LED (NSHU550, Nichia America Corporation) whose output spectrum is centered at 375 nm and a photomultiplier tube (R928, Hamamatsu) that is used to detect fluorescent emissions. A personal computer is responsible for generating the same pseudorandom code as mentioned above, synchronizing input and output, and processing digital signals. A train of pseudorandom voltage signals superimposed upon a dc signal is generated from the analog output port of a multifunction data-acquisition card (PCI-MIO-16E-1, National Instruments) and then is power amplified by a current driver to feed the LED. The update rate for the bit sequence is 10^5 bits/s, and the sequence is generated repeatedly. The coded excitation light is directed to a fluorescent sample through a light guide. The fluorescent photons are converted by the photomultiplier tube into electrical signals, which are amplified by a 40-dB amplifier before being digitized by the data-acquisition card. Digital cross correlation is performed on the computer to retrieve the impulse response, i.e., the temporal fluorescence decay profile. A solution of a kind of europium chelate (Quantum Dye, Research Organics) was used as the fluorescence
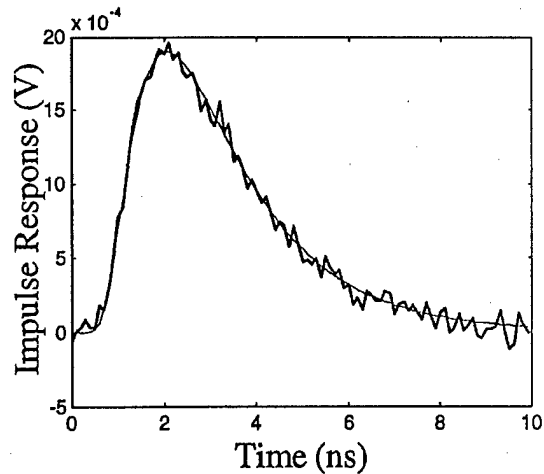

Fig. 1. Impulse response representing the TPSF of a diffusive photon density wave. Thin curve, theoretical prediction; thick curve, reconstruction from noisy environments.
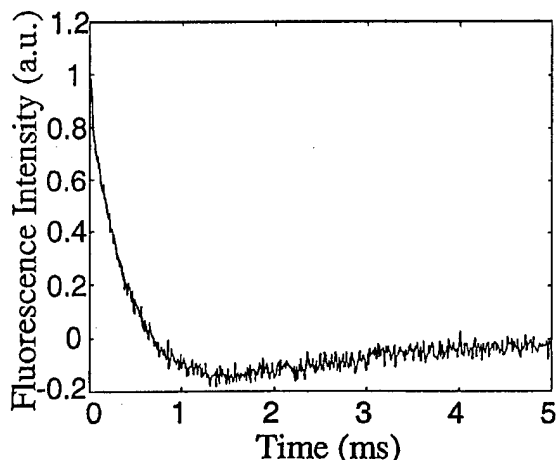
Fig. 2. Florescence decay temporal profile of the solution of eropium chelate, Quantum Dye.

sample. Quantum Dye has a long lifetime (more than 300 μs), which leads to moderate requirements for system-response speed. The specified excitation wavelength ranges from 360 to 390 nm, and the emission has a peak near 620 nm. An optical long-pass filter was used to separate the emission from the excitation.

An acquired decay profile is plotted in Fig. 2. Initially, the fluorescence intensity decays almost exponentially. However, the intensity crosses zero near ~700 μs and then remains negative for a few milliseconds. The best fit of profile $I(t)$ with two exponential decay terms is given by

$$I(t) = 1.33 \exp(-t/T_1) - 0.389 \exp(-t/T_2), \quad (5)$$

in which $T_1 = 424$ μs and $T_2 = 1745$ μs. The second term on the right-hand side of Eq. (5) represents an interesting phenomenon, which we call time-dependent suppression. To the best of our knowledge, this time-dependent suppression process had not been discovered previously. A simple theoretical explanation of it is as follows: An exciting pulse will bring more molecules to higher energy levels and thus temporarily reduce the population of the ground state. Consequently, the excitation rate is suppressed before the system returns to prepulse status. From the additional time constant T_2, one can learn more about radiative and nonradiative transitions involved.

The temporal profile in Fig. 2 was an average over 500 repeated excitations, which took 20.5 s in total. The acquisition time can be reduced to ~4 s if a bit rate of 5×10^5 bit/s is used. The standard deviation of the intensity is essentially independent of time

and averages 0.022, ~2.3% of the intensity at the origin of time. Suppose that we measure a fluorescence process described by the first term on the right-hand side of Eq. (5) with an ideal TCSPC system and that the photon-counting rate is set to be 200 counts/s. If the probability that a photon is detected in each circle (5 ms) is 1, the relative statistical error at the origin of time can be estimated by

$$\text{err} = \sqrt{\frac{T_1}{C\Delta}}, \quad (6)$$

where C is the total number of photon counts and $\Delta = 10$ μs is the temporal resolution. For example, we have err = 2.1% when $C = 10^5$. In such a case the total data-acquisition time would be 500 s. Our method can reduce the data-acquisition time by more than tenfold, or significantly improve the signal-to-noise ratio if the same time is spent. Of course, no one will really use single-photon counting for such a slow process. However, the above comparison indicates the great potential of the spread spectrum approach in its future applications in faster optical processes, such as fluorescence decays of nanosecond lifetimes.

To conclude, we have proposed a spread spectrum approach to measuring time-dependent optical processes. Our simulation and experimental results have demonstrated that this new method can remarkably reduce data-acquisition time and (or) improve overall signal-to-noise ratio. In some situations, a much lower system cost can also be expected.

References

1. A. Yodh and B. Chance, Phys. Today **48**(3), 34 (1995).
2. F. Gao, H. J. Zhao, and Y. Yamada, Appl. Opt. **41**, 778 (2002).
3. N. G. Chen and J. Bai, Phys. Med. Biol. **44**, 1669 (1999).
4. N. G. Chen and Q. Zhu, Proc. SPIE **4250**, 37 (2001).
5. Y. C. Lee, Anal. Biochem. **297**, 123 (2001).
6. C. J. de Grauw and H. C. Gerritsen, Appl. Spectrosc. **55**, 670 (2001).
7. H. Eda, I. Oda, Y. Ito, Y. Wada, Y. Oikawa, Y. Tsunazawa, and M. Takada, Rev. Sci. Instrum. **70**, 3595 (1999).
8. F. E. W. Schmidt, M. E. Fry, E. M. C. Hillman, J. C. Hebden, and D. T. Delpy, Rev. Sci. Instrum. **71**, 256 (2000).
9. R. C. Dixon, *Spread Spectrum Systems* (Wiley, New York, 1976).

Simultaneous reconstruction of absorption and scattering maps with ultrasound localization: feasibility study using transmission geometry

Minming Huang, Tuqiang Xie, Nan Guang Chen, and Quing Zhu

We report the experimental results of the simultaneous reconstruction of absorption and scattering coefficient maps with ultrasound localization. Near-infrared (NIR) data were obtained from frequency domain and dc systems with source and detector fibers configured in transmission geometry. High- or low-contrast targets located close to either the boundary or the center of the turbid medium were reconstructed by using NIR data only and NIR data with ultrasound localization. Results show that the mean reconstructed absorption coefficient and the spatial distribution of the absorption map have been improved significantly with ultrasound localization. The improvements in the mean scattering coefficient and the spatial distribution of the scattering coefficient are moderate. When both the absorption and the scattering coefficients are reconstructed the performance of the frequency-domain system is much better than that of the dc system. © 2003 Optical Society of America

OCIS codes: 170.0170, 170.3010, 170.5270, 170.7170, 170.3830.

1. Introduction

Functional imaging with near-infrared (NIR) diffused light has found potential applications in many areas.[1-9] However, one fundamental problem that we have to overcome is the intense scattering of light. As a result, diffused light probes a widespread region instead of providing information along a straight line. Multiple measurements are always correlated as a result of the overlapping of probed regions. Therefore increasing the total number of measurements does not necessarily provide more independent information for image reconstruction. In general the inverse image reconstruction is underdetermined and ill-posed. The behavior of reconstruction algorithms is affected by many factors, such as the system signal-to-noise ratio, the probe configuration, and regulation schemes used in image reconstructions.

The current approaches to image-reconstruction algorithms are (1) simple backprojection methods,[3,4] (2) perturbation methods,[10-12] and (3) finite-element

methods (FEMs).[13-15] The backprojection method provides a real-time estimation of the coarse optical properties of lesions. However, the reconstructed-image resolution is low and the lesions that appear in the images are often displaced from true locations. Perturbation methods are in general based on linear approximations to the heterogeneous functions. Born and Rytov approximations are examples. Measurements between the background and the heterogeneous medium are used to relate the optical signals at the measurement surface to absorption and scattering variations in each volume element within the sample. The least-squares method is in general used to formulate the inverse problem. Iterative search methods, such as conjugate-gradient techniques, are employed to iteratively solve the inverse problem. However, an accurate estimation of the target optical properties depends on an accurate estimation of the background optical properties, which are in general not easy to obtain in breast tissues. In addition, when the absorption or the scattering coefficients of the lesions are significantly higher than the background, the linear perturbation methods cannot give accurate optical properties. Reconstructions based on FEMs provide higher-order estimations to heterogeneous functions. However, as the scattering and absorption coefficients are expanded over local basis functions, the number of unknowns is increased considerably. Nonetheless the

independent information from diffused light is limited, and it essentially stops increasing when the source–detector pairs reach a certain number. In this case the inverse problem becomes more ill-posed and the behavior of the reconstruction algorithm may be unpredictable.

Reconstructions with the aid of *a priori* target geometry information provided by coregistered ultrasound have shown promising results in improving the accuracy of reconstructed optical properties and the localization of targets.[16–20] In this method an ultrasound probe and NIR source and detector fibers have been deployed on a handheld probe and configured in the reflection geometry. The *a priori* tissue type and lesion location as well as shape provided by coregistered ultrasound can guide the NIR image reconstruction to localized target regions. Therefore the total number of voxels with unknown optical properties can be reduced significantly and the inversion becomes well defined. In general the solution is unique and the iterative search algorithms converge very fast.

In this paper we explore experimentally the utility of the combined imaging with NIR sources and detectors configured in transmission geometry. The standard pulse-echo technique is used to obtain coregistered ultrasound images. Compared with NIR reflection geometry, transmission geometry may have the advantages of a lower requirement on the system dynamic range and higher sensitivities. In the reported experiments the FEM forward solver is used to generate a Jacobian weight matrix for simultaneous reconstruction of the absorption and the scattering coefficient maps, and the inversion is performed by using NIR data only and NIR data with *a priori* target geometry provided by coregistered ultrasound.

Frequency-domain and dc systems are widely used by many research groups. The advantage of using a frequency-domain system is that both amplitude and phase information can be obtained, and therefore simultaneous reconstruction of absorption and scattering coefficients is feasible. The disadvantage is the complexity in constructing high-frequency transmission and reception circuitries, particularly when many parallel channels are needed for fast data acquisition. This situation is more pronounced when nearly 100 source and detector positions are needed for three-dimensional (3D) imaging in transmission geometry. In addition the system cost is high. Direct-current systems have the advantages of simplicity in circuit construction and low cost. The drawbacks are that the phase information is not available and cross talk between the reconstructed absorption and scattering coefficients may be unavoidable. In this paper we compare the performance of both systems in simultaneously constructing absorption and diffusion coefficient maps in conditions of NIR reconstruction only and ultrasound guided NIR reconstruction.

2. Forward Model

A commercial FEM package FEMLAB has been used as a forward solver to generate the Jacobian weight matrix. This software has an interactive environment for modeling and simulating scientific and engineering problems based on partial differential equations. Users can utilize various existing models by defining relevant parameters and can also design specific models based on equations under consideration.

In FEMLAB the scalar-governing equation and boundary condition are given as

$$d_a \frac{\partial U(\bar{r})}{\partial t} - \nabla \cdot [c \cdot \nabla U(\bar{r}) + \alpha U(\bar{r})\gamma]$$
$$+ aU(\bar{r}) + \beta \nabla U(\bar{r}) = f(\bar{r}) \text{ in } \Omega, \quad (1)$$

$$\hat{n} \cdot [c\nabla U(\bar{r}) + \alpha U(\bar{r})\gamma] + qU(\bar{r})$$
$$= g(\bar{r}) \text{ on boundary } \partial\Omega. \quad (2)$$

Ω is the domain of interest where Eq. (1) is satisfied, and $\partial\Omega$ is the boundary of Ω where Eq. (2), representing a generalized Neumann boundary condition, is satisfied. $U(\bar{r})$ is the unknown scalar to be solved, f is the source term in Ω, c is the diffusion coefficient, a is the absorption coefficient, α is the conservative flux convection coefficient, d_a is the mass coefficient, β is the convection coefficient, γ is the conservative flux source term, $g(r)$ is the source at the boundary, $\hat{n}$ is the outward unit normal vector on $\partial\Omega$, and q is a positive number related to the internal reflection at the boundary. The time-domain photon-diffusion equation can be obtained from Eq. (1) as

$$\frac{1}{v} \frac{\partial\phi(\bar{r}, t)}{\partial t} - \nabla \cdot D(\bar{r}) \cdot \nabla\phi(\bar{r}, t) + \mu_a\phi(\bar{r}, t) = S_0(\bar{r}, t),$$
$$(3)$$

where U is replaced with $\phi(\bar{r}, t)$, the photon density at location $\bar{r}$; f with $S_0(\bar{r}, t)$, the point source term; a with μ_a, the optical absorption coefficient; c with D, the diffusion coefficient [$D = 1/(3\mu_s')$, where μ_s' is the reduced scattering coefficient]; and d_a with $1/v$, where v is the speed of light in the medium. All other coefficients are chosen to be zero.

By letting $g(r)$ equal zero, we can obtain the Neumann-type boundary condition as

$$\hat{n} \cdot D(\bar{r}) \cdot \nabla\phi(\bar{r}, t) + q\phi(\bar{r}, t) = 0. \quad (4)$$

By setting d_a to zero, we can obtain the steady-state diffusion equation as

$$\nabla \cdot D(\bar{r}) \cdot \nabla\phi(\bar{r}) - \mu_a\phi(\bar{r}) = -S_0(\bar{r}). \quad (5)$$

Furthermore, by replacing μ_a with $\mu_a - i\omega/v$, where ω is the modulation frequency, we can obtain a frequency-domain diffusion equation as

$$\nabla \cdot D(\bar{r}) \cdot \nabla\phi(\bar{r}, \omega) - \left(\mu_a - \frac{i\omega}{v}\right)\phi(\bar{r}, \omega)$$
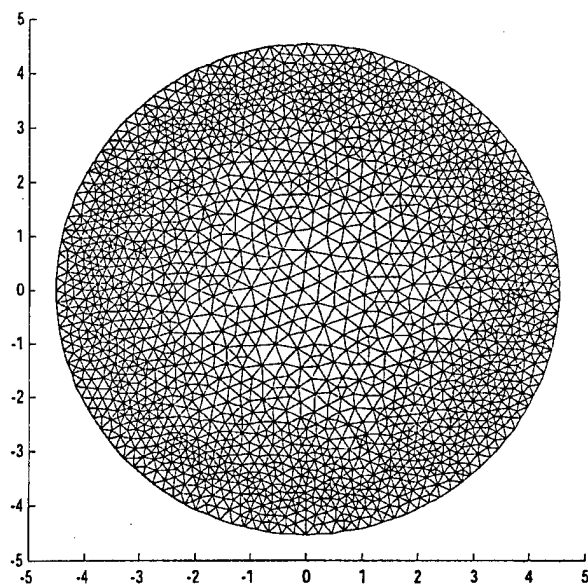$$= -S_0(\bar{r}, \omega). \quad (6)$$

Fig. 1. Two-dimensional mesh used for NIR image geometry.

Assume that the changes due to the absorption and the scattering inhomogeneities are small. The Jacobian matrix

$$\mathbf{W}_{ij} = \left[\frac{\Delta \phi_{ij}}{\Delta \mu_{aj}}, \frac{\Delta \phi_{ij}}{\Delta D_j} \right],$$

that relates the photon-density perturbation at boundary cell i and imaging voxel j with absorption coefficient change $\Delta \mu_{aj}$ and diffusion coefficient change ΔD_j, is given as

$$[\mathbf{W}_{ij}] = \begin{bmatrix} \dfrac{\Delta \phi_{11}}{\Delta \mu_{a1}} & \cdots & \dfrac{\Delta \phi_{1L}}{\Delta \mu_{aL}} & \dfrac{\Delta \phi_{11}}{\Delta D_1} & \cdots & \dfrac{\Delta \phi_{1L}}{\Delta D_L} \\ \dfrac{\Delta \phi_{21}}{\Delta \mu_{a1}} & \cdots & \dfrac{\Delta \phi_{2L}}{\Delta \mu_{aL}} & \dfrac{\Delta \phi_{21}}{\Delta D_1} & \cdots & \dfrac{\Delta \phi_{2L}}{\Delta D_L} \\ \vdots & \ddots & \vdots & \vdots & \ddots & \vdots \\ \dfrac{\Delta \phi_{M1}}{\Delta \mu_{a1}} & \cdots & \dfrac{\Delta \phi_{ML}}{\Delta \mu_{aL}} & \dfrac{\Delta \phi_{M1}}{\Delta D_1} & \cdots & \dfrac{\Delta \phi_{ML}}{\Delta D_L} \end{bmatrix},$$

(7)

where M is the total number of boundary cells and L is the total number of imaging voxels.

3. Computation Procedures

We have generated a two-dimensional (2D) mesh with 4050 triangle elements and 2088 nodes (Fig. 1). The radius of the physical boundary is chosen to be 45.26 cm and the extrapolation distance $Z_b = 0.7 \cdot 1_{tr}$ [$1_{tr} = 1/(\mu_s' + \mu_a)$] is calculated to be 0.1169 cm,[21] where $\mu_s' + \mu_a$ is the background value and is chosen to be 6 cm^{-1} (a typical value for normal breast tissue). To speed up the Jacobian matrix calculation, we chose a coarse mesh of 5 cm × 5 cm in the middle of the 2D mesh by assuming that there are no perturbations outside this area. The imaging pixel size is chosen to be 0.25 cm × 0.25 cm inside the coarse

mesh. As a result the total number of unknown voxels is 400, which is comparable with the total number of measurements.

In the Jacobian matrix calculation we evaluated the linearity of $\Delta \phi_{ij} / \Delta \mu_{aj}$ versus $\Delta \mu_{aj}$ with μ_{aj} changing from 0.02 to 0.3 cm^{-1} (the typical range of the absorption coefficient for breast lesions) at many cell locations. For dc component calculations the error due to the linear approximation is always less than 0.4%. For frequency-domain calculations the real and imaginary parts of ϕ_{ij} of several cells are 1 or 2 orders smaller, and they are very sensitive to small perturbations. However, even for the worst case, the error due to the use of the linear approximation is also less than 0.5% for 24 out of 28 detector locations. Therefore we can simplify the Jacobian matrix calculation by computing $\Delta \phi_{ij} / \Delta \mu_{aj}$ at two points (μ_{aL}, μ_{aH}) that are between 0.02 and 0.3 cm^{-1}. The selection of these two points is based on the following considerations. The linear slope $\Delta \phi_{ij} / \Delta \mu_{aj}$ is best estimated when a smaller perturbation $\Delta \mu_{aj}$ is used. However, a $\Delta \mu_{aj}$ that is too small is not suitable for computing $\Delta \phi_{ij}$. As a good compromise we chose $\mu_{aL} = 0.02$ cm^{-1} and $\mu_{aH} = 0.06$ cm^{-1} for all the calculations. We also evaluated the linearity of $\Delta \phi_{ij} / \Delta D_j$ versus ΔD_j with D_j changing from 0.0556 (the corresponding μ_s' is 6 cm^{-1}) to 0.0306 cm (the corresponding μ_s' is 10.9 cm^{-1}) (the typical diffusion coefficient range for breast lesions) at many cell locations. For both the dc component and frequency-domain calculations the error due to the use of a linear approximation is always less than 0.2%. Therefore we compute $\Delta \phi_{ij} / \Delta D_j$ by using two points at 0.0556 and 0.0356 cm.

The experimental data included many unknown systematic factors (unknown source, detector gains, etc.). To remove those unknown factors, we used the normalized difference method in Ref. 22 as

$$\left[\frac{\phi_{m(i)} - \phi_{mr(i)}}{\phi_{mr(i)}} \phi_{cr(i)} \right] = [W_{ij}] \cdot [\Delta \mu_{a(ji)}, \Delta D_{ji}], \quad (8)$$

where $\phi_{m(i)}$ is the measured heterogeneous data associated with the source–detector pair i with the target in the homogeneous medium, $\phi_{mr(i)}$ is the measured homogeneous data, $\phi_{cr(i)}$ is the calculated forward homogeneous data used for the weight matrix calculation. The ϕ is a complex value in the frequency-domain case. The unknown system factors present in both sets of measured heterogeneous and homogeneous data are canceled by taking the ratio of the perturbation (heterogeneous–homogeneous) to the reference (homogeneous) measurements.

To alleviate the cross talk between the absorption coefficient and the diffusion coefficient, we also normalized each column and row of the weight matrix by

their own mean value to improve the matrix condition. Thus the inverse problem is modified as

$$[F_{ii}] \cdot \left[\frac{\phi_{m(i)} - \phi_{mr(i)}}{\phi_{mr(i)}} \phi_{cr(i)} \right]$$
$$= [F_{ii}] \cdot [W_{ij}] \cdot [G_{jj}] \cdot [\Delta X_{ji}], \quad (9)$$

where $\lfloor \Delta\mu_{a(ji)}, \Delta D_{ji} \rfloor = \lfloor G_{jj} \rfloor \cdot \lfloor \Delta X_{(ji)} \rfloor$ and

$$F_{ii} = \left(\frac{1}{N} \sum_{k=1}^{N} W_{ik} \right)^{-1},$$
$$i = 1, 2, \ldots, M \ (F_{ij} = 0 \text{ when } i \neq j),$$

$$G_{jj} = \left(\frac{1}{M} \sum_{k=1}^{M} W_{kj} \right)^{-1},$$
$$j = 1, 2, \ldots, L \ (G_{ij} = 0 \text{ when } i \neq j).$$

Finally the conjugate gradient method is used for solving Eq. (9). Since the error function

$$\left\| F \cdot W \cdot G \cdot \Delta X - F \cdot \frac{\phi_{m(i)} - \phi_{mr(i)}}{\phi_{mr(i)}} \phi_{cr(i)} \right\|^2$$

reduces consistently and becomes flat after certain iterations (around 30 for reconstruction with the NIR data only and 3 for the NIR with ultrasound guidance), the stopping criteria are chosen to be 100 and 3 iterations for the NIR only and the NIR with ultrasound localization, respectively. The corresponding computation time is around 2 min for NIR data only and 30 s for NIR with ultrasound information.

In the experiments, data are obtained from a 3D model (the finite cylindrical medium and the finite length target). However, the Jacobian matrix computation is based on a 2D model (the infinite cylindrical medium and the infinite-length target). According to Refs. 23 and 24 the 2D/3D difference between intensity is reasonably independent of source–detection separation and it is reasonable to correct it by simply multiplying or dividing a constant. Therefore the normalized difference method not only cancels the unknown source–detector gains but also partially eliminates the 2D/3D model mismatch by taking the ratio of the perturbation and the reference measurements.

4. Experimental Systems

To compare the performance of the frequency-domain and the dc systems with and without ultrasound localization, we constructed both systems. Details of our multisource and multidetector frequency-domain system can be found in Ref. 18. Briefly, it consists of 12 pairs of dual-wavelength sources [780 nm (LT024) and 830 nm (LT015), Sharp Corporation] modulated at 140 MHz and 8 parallel detectors (R928, Hamamatsu Corporation). These sources and detectors are coupled to the medium through optical fibers.

Our new dc system consists of six pairs of dual-wavelength laser diodes (780 and 830 nm) amplitude modulated at 20 kHz to avoid dc fluctuations (Fig. 2).
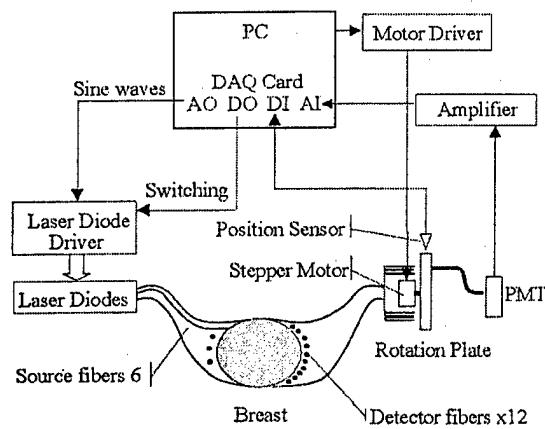

Fig. 2. Schematic of our new dc system: AO, analog output; AI, analog input; DO, digital output; DI, digital input.

Twelve detector fibers are sequentially coupled to a photomultiplier tube (PMT) (R928, Hamamatsu Corporation) through a mechanical multiplexer that uses a stepper motor to collimate accurately a coupling light guide on a rotation plate to one of the detection fibers. Each light source has two output levels of 30 dB in difference to avoid PMT saturation and to improve the system dynamic range. A National Instrumentation data acquisition (DAQ) card is used to generate sinusoidal waveforms on top of a constant current to drive one laser diode at a time. The photon density wave detected by the PMT is amplified and then digitized by the same DAQ card. The corresponding amplitude is retrieved from the acquired waveform on a PC. The digital ports of the DAQ card are used to switch laser diodes sequentially, control the output level, and input a feedback signal for closed-loop stepper motor control. The total DAQ time for a complete data set is around 1 min.

Since our dc system is modulated at 20 kHz, the measured amplitude is an ac signal instead of the dc component that we used for forward Jacobian matrix calculation. We estimated the difference by using a spherical wave of light energy density $[\exp(jk\rho)/D\rho]$ of two wave numbers, $k_1 = (-\mu_a/D)^{1/2}$ and $k_2 = [(-\mu_a + j \times \omega/\upsilon)/D]^{1/2}$, where $\omega = (2\pi)2 \times 10^4$ Hz and υ and D are the speed of light and the diffusion coefficient, respectively. The normalized difference $[\exp(jk_1\rho) - \exp(jk_2\rho)]/\exp(jk_1\rho)$ can be approximated as

$$-\frac{j\rho\omega}{2\upsilon} [1/(D\mu_a)]^{1/2},$$

and it is larger when the wave propagates deeper into the tissue and the background absorption is smaller. For the worst case of $\mu_a = 0.01$ cm^{-1} and $\rho = 10$ cm the difference is less than 3.295^{-5}. Therefore we directly use the Jacobian matrix calculated from the steady-state diffusion equation [Eq. (5)] to relate the measured amplitude data for the inversion.

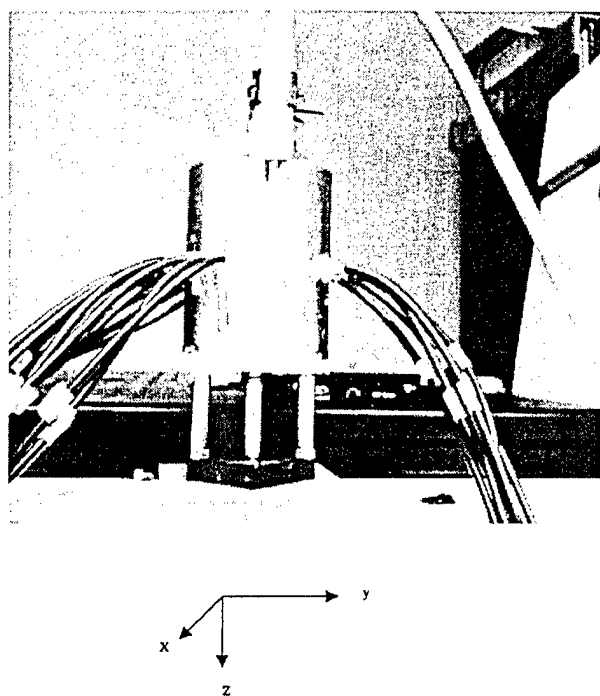The experimental setup is shown in Fig. 3. During experiments, source and detector fibers were

Fig. 3. Experimental setup. A commercial ultrasound probe is located at the top of a water tank, and the NIR source and detector fibers are deployed around the tank and configured in transmission geometry.

placed on a circular plane (Fig. 4). A commercial ultrasound probe of 3.5-MHz central frequency (HP77020A ultrasound imaging system) was placed on top of a water tank filled with Intralipid. This one-dimensional commercial probe provides a cross-section image in the y-z imaging plane (called the B-scan), where y is the lateral direction and z is the propagation direction. By translating the probe mechanically in the x direction, we acquired 3D volumetric image data. Windowing the 3D data in the z direction at a particular depth provides 2D target spatial images at the x-y plane (called the C-scan). C-scans are coregistered with the NIR images. An Intralipid solution of 0.6% was used as a homogeneous background. The fitted μ_a and μ_s' of the Intralipid at 780 nm were 0.02 and 6 cm^{-1}, respectively.

Since we have a limited number of source and detector positions, we placed 8 source fibers instead of 12 on a quarter circle and 8 detector fibers on the opposite quarter for frequency-domain measurements [Fig. 4(a)]. For dc measurements we placed 6 source fibers on a quarter circle and 12 detector fibers on the opposite quarter [see Fig. 4(b)]. After obtaining one set of heterogeneous NIR data with a target in the Intralipid (8 × 8 measurements for the frequency system, 6 × 12 measurements for the dc system), we simply rotated the target by 90° for the frequency-domain system and 77.14° for the dc system to get another set of data. Figure 4(c) shows the rotation scheme used during frequency-domain experiments. Three rotations were performed to obtain one complete data set for reconstruction, which covered 360°. For dc measurements a similar rotation scheme was used and four rotations were performed to obtain one complete data set. Three-dimensional ultrasound data were obtained simultaneously with NIR data acquisition.

5. Results

For NIR reconstruction with transmission geometry the perturbations in ϕ caused by the target are related to the location of the target and the contrast between the target and the background. It is much harder to reconstruct a low-contrast target located in the middle of the medium. In our experiments a cylindrical target (high/low contrast) 1.0 cm in diameter was placed at two typical locations (at the center and close to the boundary). The target was made of polyester resin with calibrated μ_a and μ_s'.[25] Based on the calibration results from Dartmouth College, the absorption coefficient of the target was from 0.20 to 0.3 cm^{-1} for the high-contrast target case and was 0.07 cm^{-1} for the low-contrast target; μ_s' of both targets was 9.6 cm^{-1}. The repeatability of the calibration was within ±5%.

A. Reconstruction when the Frequency-Domain System is Used

For the high-contrast target case, improvements in the reconstructed μ_a are dramatic when ultrasound localization is used. Figures 5(a) and 5(b) show the simultaneously reconstructed absorption and diffu-
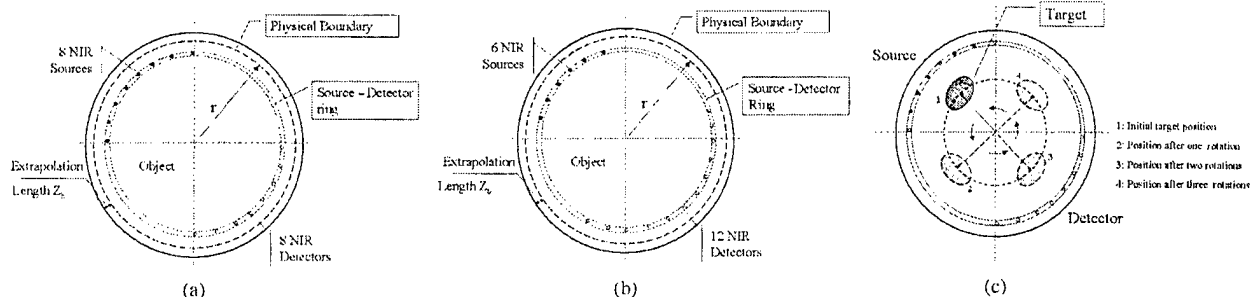

Fig. 4. Configurations of NIR sources and detectors used in the reported experiments: (a) frequency-domain experiments, (b) dc experiments, (c) top view of target rotation scheme used in frequency-domain measurements.
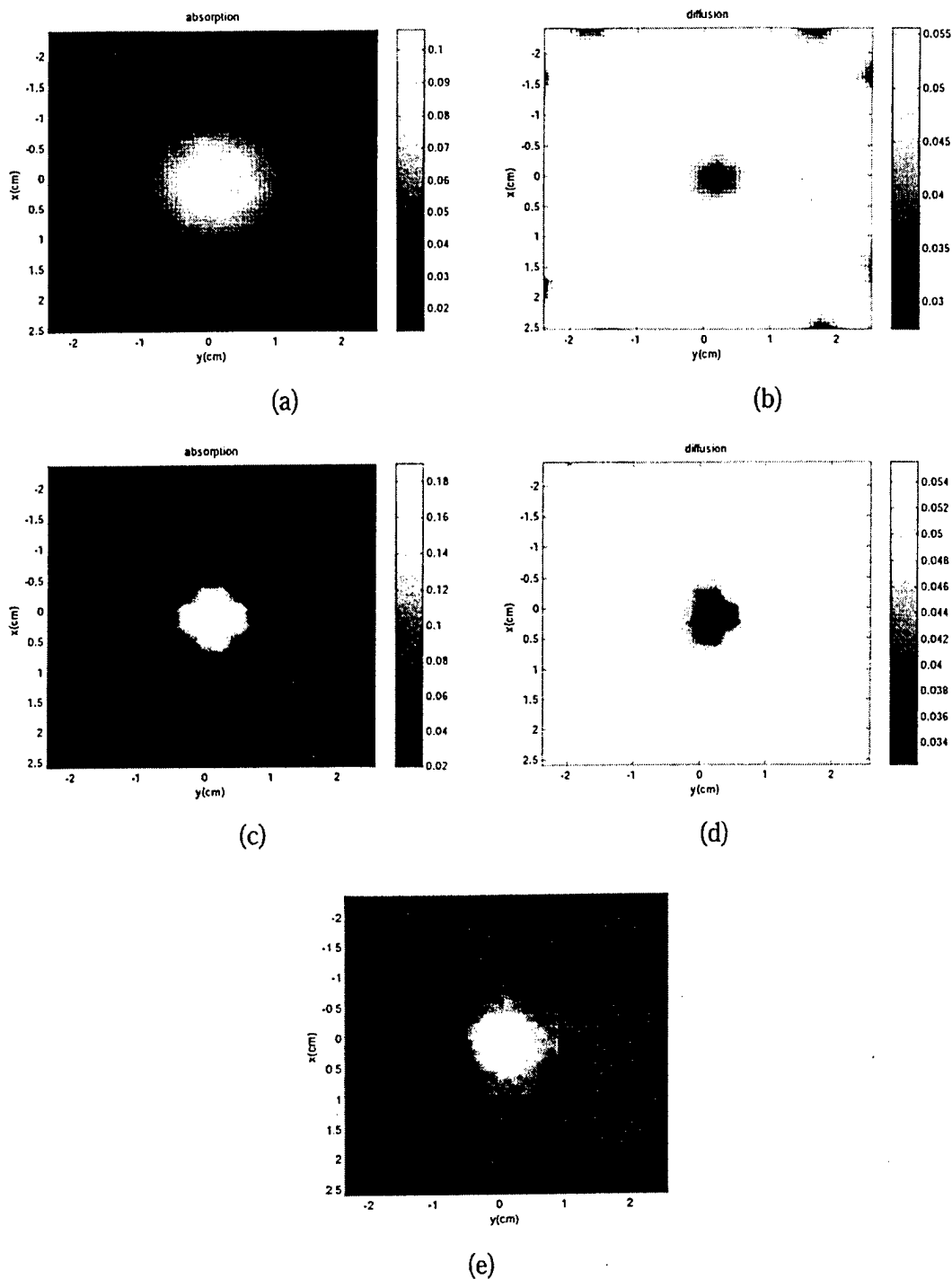
Fig. 5. Comparisons of simultaneously reconstructed absorption and diffusion coefficient maps of a high-contrast target located at the center of the turbid medium: (a), (b) reconstructed μ_a and D distributions when NIR data only are used; (c), (d), reconstructed μ_a and D distributions with ultrasound localization; (e) coregistered ultrasound C-scan image used to guide the NIR reconstruction. X and Y are the spatial dimensions in centemeters.

sion maps where NIR data only is used when the target is located at the center of the medium, while Figs. 5(c) and 5(d) show the reconstructed absorption and diffusion maps with ultrasound localization. Figure 5(e) is the C-scan ultrasound image obtained

at the source–detector plane. A threshold was applied to the ultrasound image, which was chosen as the FWHM from the peak value. The pixels with gray-scale values greater than the threshold were mapped out as a target region, while the pixels with
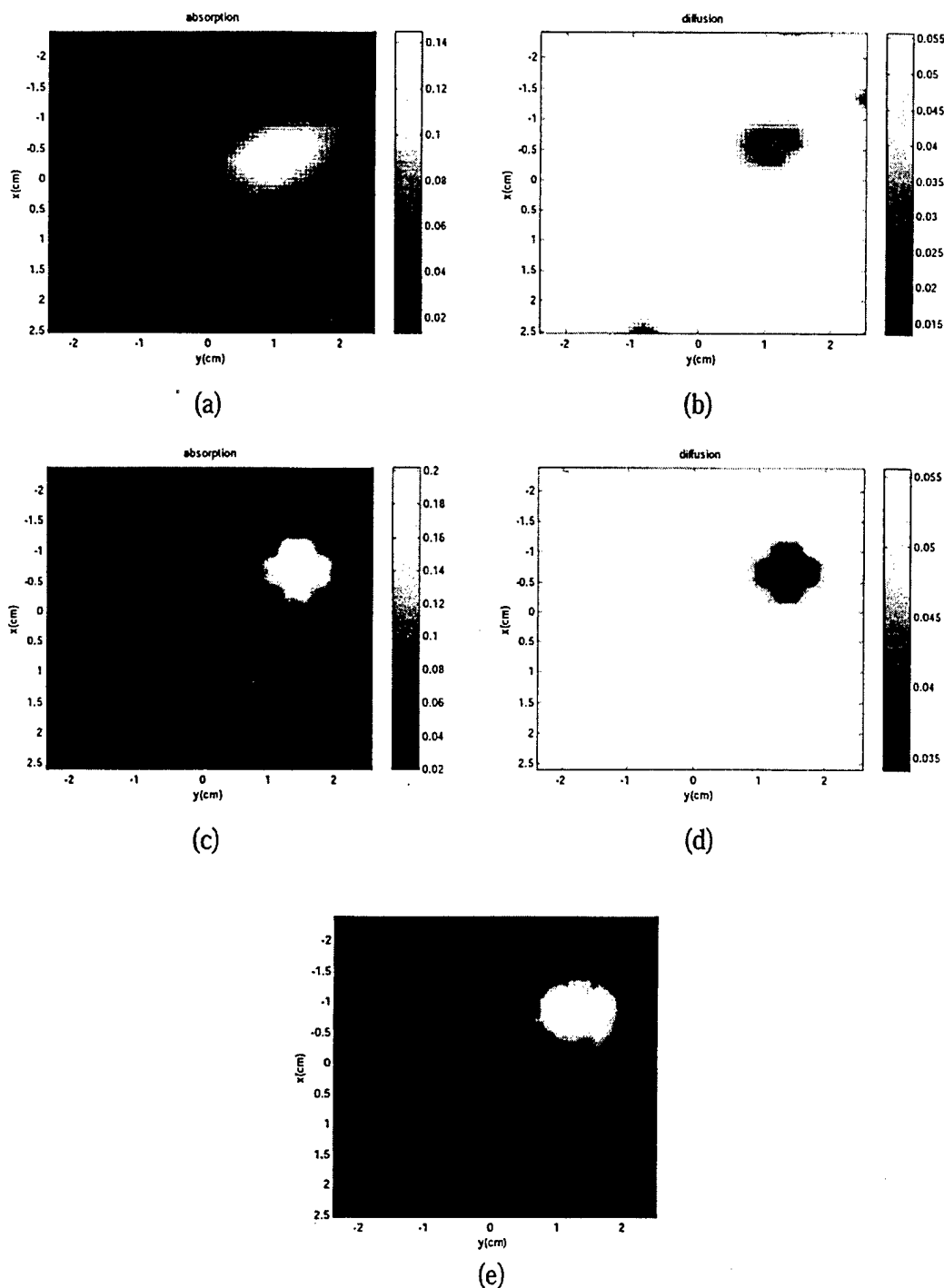
Fig. 6. Comparisons of simultaneously reconstructed absorption and diffusion coefficient maps of a high-contrast target located closer to the boundary of the turbid medium: (a), (b) reconstructed μ_a and D distributions when NIR data only are used; (c), (d), reconstructed μ_a and D distributions with ultrasound localization; (e) coregistered ultrasound C-scan image used to guide the NIR reconstruction.

values less than the threshold were identified as a nontarget region. The inverse reconstruction was localized to the target region. With ultrasound the mean reconstructed absorption coefficient was improved from 32.4% to 64.4% of the calibrated mean value and the FWHM was improved from 140% to 100% of the true target size. The mean value was calculated from the pixels with absorption coefficients greater than the FWHM in the target mass region. As for the diffusion coefficient the mean reconstructed values were within 5% of the calibrated value both with and without ultrasound localization.

(a)   (b)

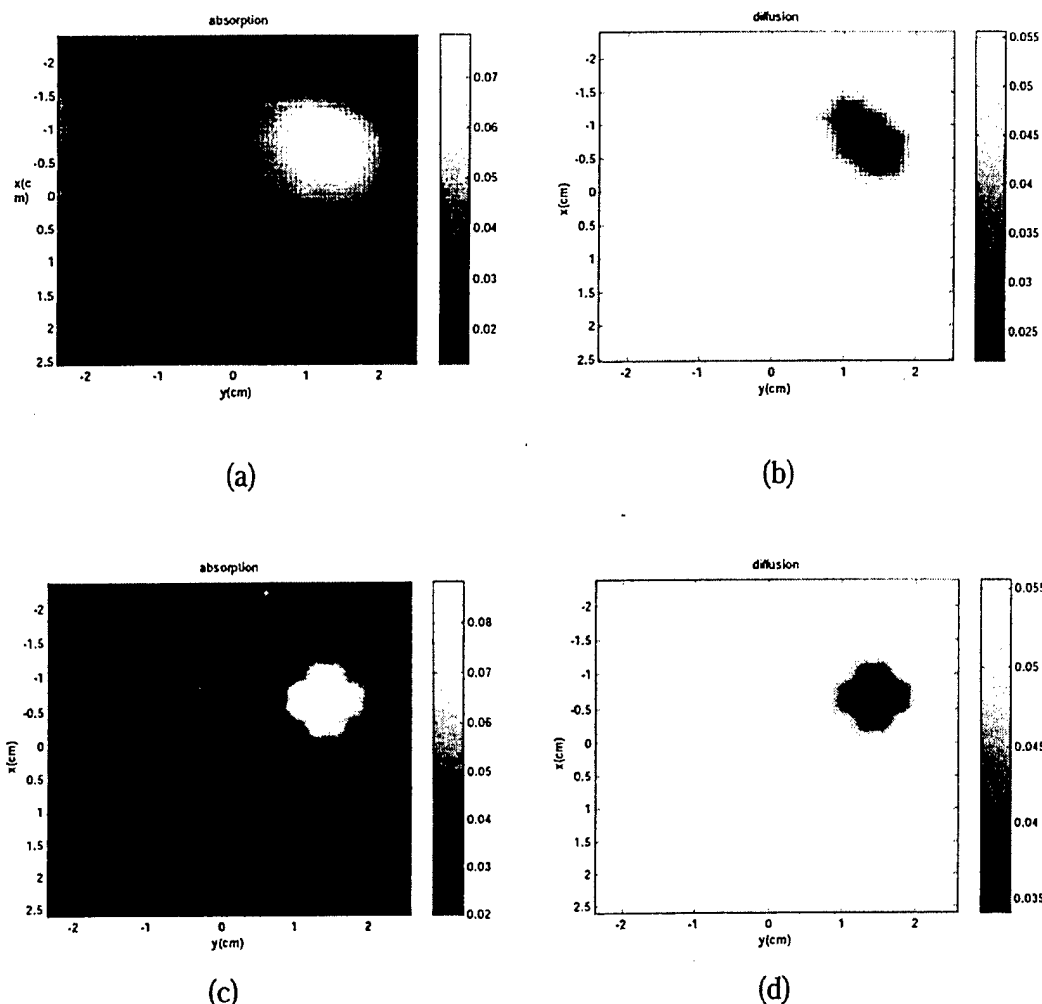(c)   (d)

Fig. 7. Comparisons of simultaneously reconstructed absorption and diffusion coefficient maps of a low-contrast target located closer to the boundary: (a), (b) simultaneously reconstructed μ_a and D distributions when NIR data only are used; (c), (d), simultaneously reconstructed μ_a and D distributions with ultrasound localization.

However, the edge artifacts seen in Fig. 5(b) were eliminated by using ultrasound guidance.

Figure 6 shows the experimental results of the same high-contrast target located close to the boundary. Figure 6(a) is the μ_a distribution reconstructed by using NIR data only. The reconstructed mean absorption coefficient was ~45.2% of the calibrated mean value, and the FWHM was around 1.3 cm, which was 130% of the true target size. Figure 6(b) is the D distribution simultaneously reconstructed with the μ_a map by using NIR data only. Artifacts in the boundary of D distribution are visible. The reconstructed mean value was ~65.2% of the calibrated value, and the FWHM was around 1.2 cm. Figures 6(c) and 6(d) are the simultaneously reconstructed μ_a and D distributions with coregistered ultrasound localization. Figure 6(e) is the coregistered C-scan ultrasound image obtained in the source–detector plane. With ultrasound localization the mean μ_a

was improved to 65.2% of the calibrated mean value and the FWHM was improved to 1 cm. The mean D was improved to 102% of the calibrated value. Artifacts in the D distribution were eliminated with ultrasound localization.

Figure 7 shows the experimental results of the low-contrast target located close to the boundary. Figure 7(a) is the μ_a distribution reconstructed by using NIR data only. The reconstructed mean absorption coefficient was ~93% of the calibrated value, and the FWHM was around 1.3 cm. Figure 7(b) is the D distribution simultaneously reconstructed with the μ_a map by using NIR data only. The reconstructed mean value was ~81% of the calibrated value, and the FWHM was around 1.2 cm. Figures 7(c) and 7(d) are the simultaneously reconstructed μ_a and D distributions with coregistered ultrasound localization. With ultrasound localization the mean μ_a was within 11% of the calibrated value and the FWHM was improved to 1 cm. The mean D was improved to
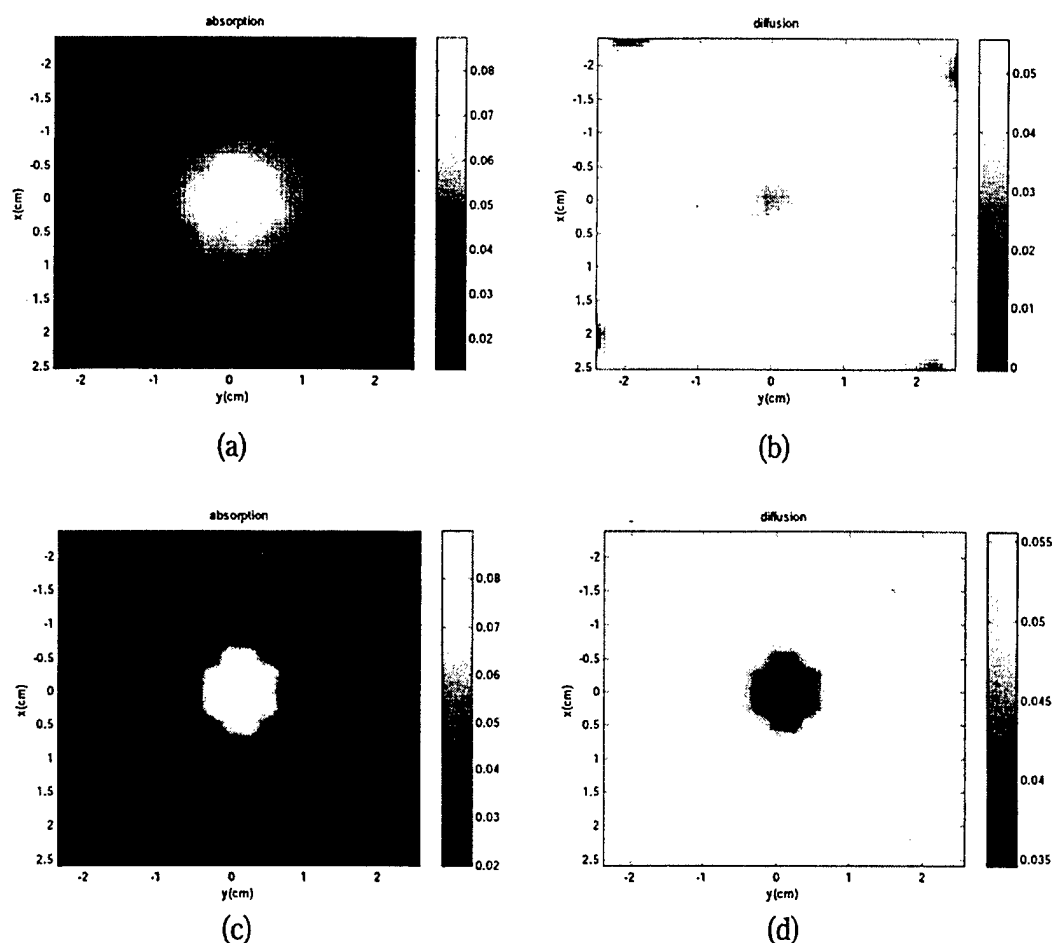
(a)

(b)

(c)

(d)

Fig. 8. Comparisons of simultaneously reconstructed absorption and diffusion maps of the same low-contrast target located at the center of the turbid medium: (a), (b), reconstructed μ_a and D distributions when NIR data only are used; (c), (d), reconstructed μ_a and D distributions with ultrasound localization.

102% of the calibrated value. The edge artifacts seen in the D distribution were eliminated with ultrasound localization.

Figure 8(a) and 8(b) show the simultaneously reconstructed μ_a and D distributions of the same low-contrast target located at the center. As one can see the spatial distributions of μ_a and D are worse than those shown in Figs. 7(a) and 7(b). Artifacts in the boundary of the D distribution are visible.

The reconstructed mean μ_a was ~94% of the calibrated value, and the reconstructed mean D was ~92% of the calibrated value. Figures 8(c) and 8(d) are the simultaneously reconstructed absorption and diffusion coefficient maps with ultrasound localization. The reconstructed mean μ_a is within 13% of the calibrated value and the reconstructed mean D is within 6% of the calibrated value. The FWHM of the μ_a map has been improved by 30%,

Table 1. Experimental Results from the Frequency-Domain System

Target Location	Target Contrast	NIR Only		NIR + US		Calibrated Value from Dartmouth College	
		Mean μ_a (cm^{-1})	Mean D (cm)	Mean μ_a (cm^{-1})	Mean D (cm)	Mean μ_a (cm^{-1})	Mean D (cm)
Close to the boundary	High contrast	0.113 (45.2%[a])	0.030 (87%)	0.163 (65.2%[a])	0.0355 (102%)	0.2–0.3	0.0347 ± 5%
	Low contrast	0.065 (93%)	0.028 (81%)	0.078 (111%)	0.0355 (102%)	0.07 ± 5%	0.0347 ± 5%
At the center	High contrast	0.081 (32.4%[a])	0.0353 (101%)	0.161 (64.4%[a])	0.0363 (105%)	0.2–0.3	0.0347 ± 5%
	Low contrast	0.067 (94%)	0.032 (92%)	0.0793 (113%)	0.037 (106%)	0.07 ± 5%	0.0347 ± 5%

[a]The percentage is calculated based on the mean value of 0.2–0.3 cm^{-1}.
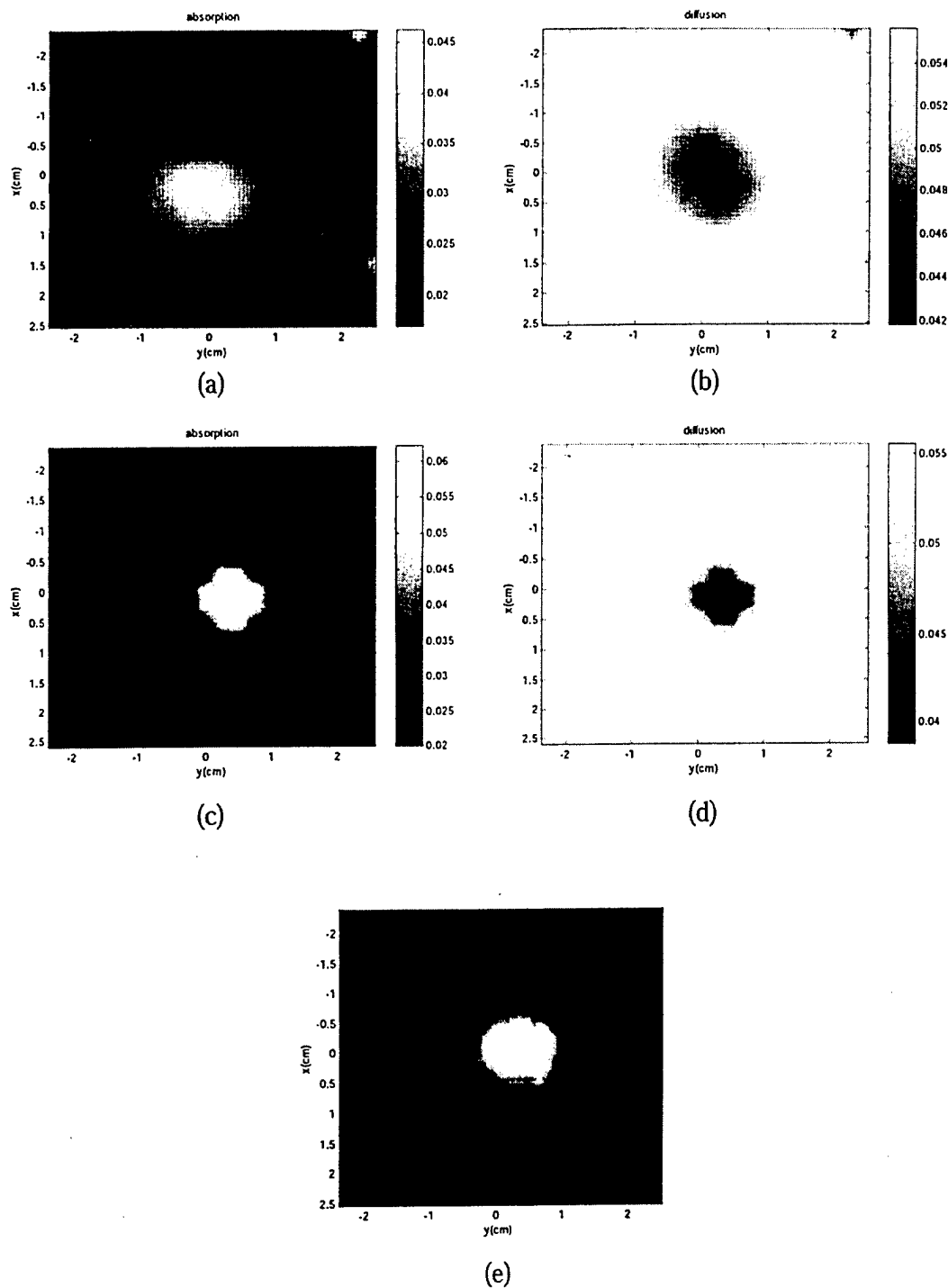US, ultrasound

Fig. 9. Comparisons of simultaneously reconstructed absorption and diffusion maps of a high-contrast target located at the center of the medium. The dc system of the configuration in Fig. 4(b) was used for the experiments: (a), (b), reconstructed μ_a and D distributions when NIR data only are used; (c), (d), reconstructed μ_a and D distributions with ultrasound localization; (e) coregistered C-scan ultrasound image used to guide the NIR reconstruction.

and artifacts in the D distribution have been eliminated.

In Table 1 are summaries of the experimental results of the two cases in which the target was located

at different positions. In general, when the target was located at the center, the results with NIR data only were poorer than those when the target was located closer to the boundary. With ultrasound lo-
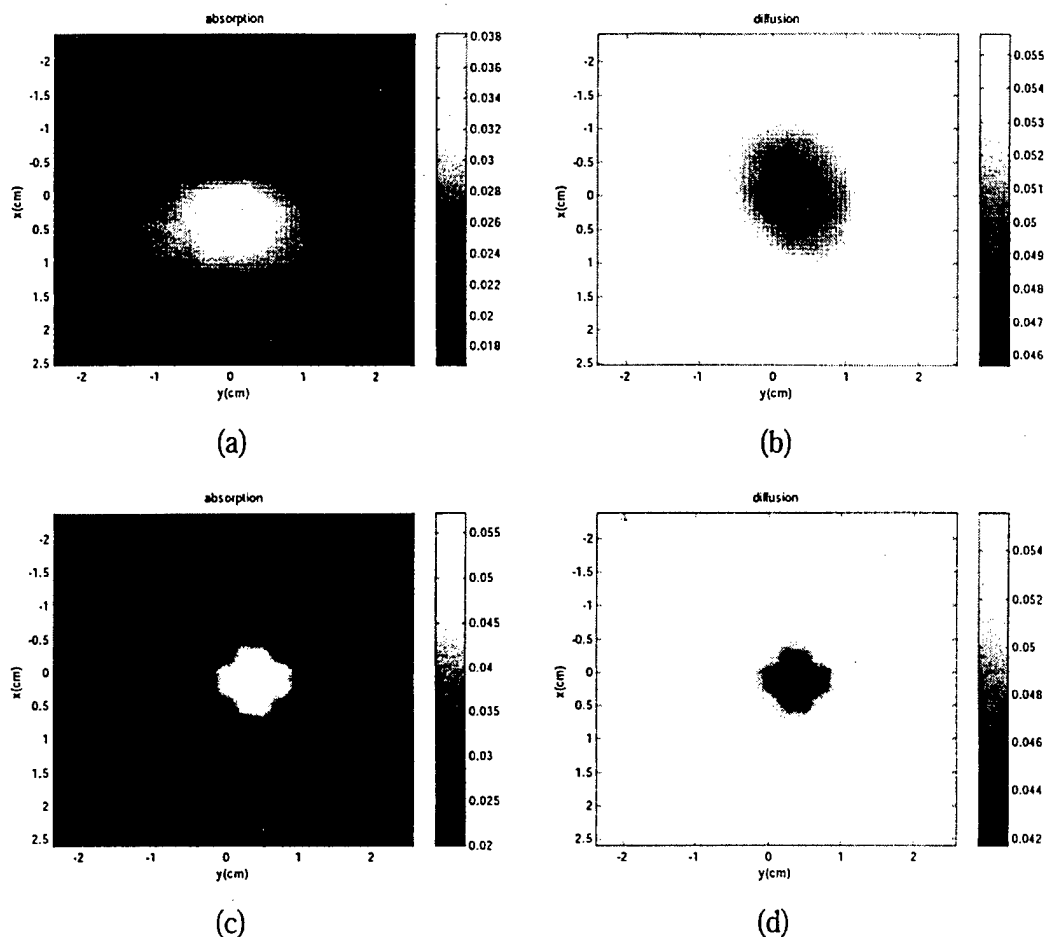
Fig. 10. Comparisons of simultaneously reconstructed absorption and diffusion coefficient maps of a low-contrast target located at the center of the medium: (a), (b), reconstructed μ_a and D distributions, respectively, when NIR data only are used; (c) (d), reconstructed μ_a and D distributions, respectively, with ultrasound localization.

calization, improvements in terms of spatial distributions were higher than those when the target was located at the boundary.

B. Reconstruction when the Direct-Current System is Used

Figures 9(a) and 9(b) show the simultaneously reconstructed μ_a and D distributions of the high-contrast target located at the center. The reconstructed mean μ_a was only 15.6% of the calibrated value, and the reconstructed mean D was ~132% of the calibrated value. Figures 9(c) and 9(d) are the simultaneously reconstructed absorption and diffusion maps with ultrasound localization. Figure 9(e) shows the C-scan ultrasound image obtained at the source–detector plane and used for the localization. The reconstructed mean μ_a has been improved to 22% of the calibrated value and the reconstructed mean D has been improved to 121% of the calibrated value. The FWHM's of μ_a and the D maps have been improved by 50% and 30%, respectively.

Figure 10 shows the experimental results of the low-contrast target located at the center of the me-

dium. Figure 10(a) is the μ_a distribution reconstructed by using NIR data only. The spatial distribution of μ_a is much worse than the high-contrast case. The reconstructed mean absorption coefficient is only 47% of the calibrated value, and the FWHM is around 1.6 cm. Figure 10(b) shows the D distribution simultaneously reconstructed with μ_a by using NIR data only. The reconstructed mean value was ~140% of the calibrated value, and the FWHM was around 1.4 cm. Figures 8(c) and 8(d) are the simultaneously reconstructed μ_a and D distributions with coregistered ultrasound localization. With ultrasound localization the accuracy of reconstructed mean μ_a was improved to 73% of the calibrated value, and the FWHM was improved to 1 cm, while the accuracy of reconstructed mean D was 126% of the calibrated value and the FWHM was improved by 40%.

In Table 2 are summaries of the experimental results of high- and low-contrast cases when the target is located at different positions. Generally the reconstructed absorption coefficients are much lower than those obtained from the frequency-domain sys-

Table 2. Experimental Results from the dc System

Target Location	Target Contrast	NIR Only		NIR + US		Calibrated Value from Dartmouth College	
		Mean Mua (cm^{-1})	Mean D (cm)	Mean Mua (cm^{-1})	Mean D (cm)	Mean Mua (cm^{-1})	Mean D (cm)
Close to the boundary	High contrast	0.0485 (19.4%[a])	0.043 (123%)	0.059 (23.6%[a])	0.043 (123%)	0.2–0.3	0.0347 ± 5%
	Low contrast	0.047 (67%)	0.044 (126%)	0.049 (70%)	0.046 (132%)	0.07 ± 5%	0.0347 ± 5%
At the center	High contrast	0.039 (15.6%[a])	0.046 (132%)	0.055 (22%[a])	0.042 (121%)	0.2–0.3	0.0347 ± 5%
	Low contrast	0.0328 (47%)	0.0486 (140%)	0.051 (73%)	0.044 (126%)	0.07 ± 5%	0.0347 ± 5%

[a]The percentage is calculated on the basis of the mean value of 0.2–0.3 cm^{-1}.
US, ultrasound

tem, and the reconstructed diffusion coefficients are much higher than those from the frequency domain. The improvements with ultrasound localization are much less than that obtained from the frequency-domain system.

Comparing the results from frequency-domain and dc systems, we find that the reconstructed results from the frequency-domain system are much better in terms of accuracy. With ultrasound localization the mean absorption coefficients obtained from the frequency-domain data are approximately 111–113% of the calibrated value for the low-contrast target and around 64–65% of the calibrated mean value for the high-contrast target, while they are only 70–73% and 22–23.6% for the same cases in dc. The mean diffusion coefficients obtained from the frequency-domain data are within 102–108% of the calibrated value, while they are approximately 121–132% for the same cases in the dc. The FWHMs obtained from the frequency-domain reconstructions are always within 90–130% of the calibrated value, while the FWHMs are approximately 110–160% for the same cases in the dc.

6. Discussion

The reconstructed absorption and scattering distributions can be partially improved by iteratively updating the Jacobian matrix to account for higher-order terms of the weight matrix. However, this procedure is time-consuming and prohibits near-real-time NIR image processing. The iterative updating of a localized Jacobian matrix within the ultrasound specified region could further improve the accuracy of reconstructed absorption and diffusion coefficients with reduced computation load. Currently we are pursuing this research, and results will be reported in the near future.

In the reported phantom studies we assume that the lesions are isolated and embedded in a homogeneous background. Therefore we localize the image reconstruction by using the target geometry obtained from ultrasound. In the clinical breast-imaging cases the background tissues also scatter and absorb the diffusive light, which are also accounted for in the dual-mesh reconstruction scheme reported in Ref. 20.

7. Summary

We have reported experimental results from the simultaneous reconstruction of absorption and scattering maps with ultrasound localization. Transmission geometry was used for NIR-imaging reconstruction, and standard pulse-echo ultrasound was used for obtaining coregistered ultrasound images. When a frequency-domain system was used the ultrasound localization results showed that the reconstructed mean absorption coefficients of high-contrast phantom targets improved more than 20%, while improvements to the reconstructed mean diffusion coefficients were moderate. For low-contrast targets no significant improvement has been shown in the mean reconstructed values. However, improvements in the target spatial distributions are significant. When a dc system was used, improvements in using ultrasound localization were small in terms of mean reconstructed values. Owing to the lack of phase information and possible cross talk between absorption and scattering coefficients, the dc system performance is much worse than that of the frequency-domain system. With ultrasound localization the reconstruction speed has improved by a factor of 10 and near-real-time optical imaging becomes feasible.

References

1. B. Tromberg, N. Shah, R. Lanning, A. Cerussi, J. Espinoza, T. Pham, L. Svaasand, and J. Butler, "Noninvasive *in vivo* char-

acterization of breast tumors using photon migration spectroscopy," Neoplasia 2(1:2), 26–40 (2000).

2. J. B. Fishkin, O. Coquoz, E. R. Anderson, M. Brenner, and B. J. Tromberg, "Frequency-domain photon migration measurements of normal and malignant tissue optical properties in human subject," Appl. Opt. 36, 10–20 (1997).

3. S. Fantini, S. Walker, M. Franceschini, M. Kaschke, P. Schlag, and K. Moesta, "Assessment of the size, position, and optical properties of breast tumors in vivo by noninvasive optical methods," Appl. Opt. 37, 1982–1989 (1998).

4. R. M. Danen, Y. Wang, X. D. Li, W. S. Thayer, and A. G. Yodh, "Regional imager for low-resolution functional imaging of the brain with diffusing near-infrared light," Photochem. Photobiol. 67, 33–40 (1998).

5. B. Pogue, S. P. Poplack, T. O. McBride, W. A. Wells, K. S. Osterman, U. Osterberg, and K. D. Paulsen, "Quantitative hemoglobin tomography with diffuse near-infrared spectroscopy: pilot results in the breast," Radiology 218, 261–266 (2001).

6. B. Chance, J. Glickson, R. Weissleder, C. Tung, D. Blessington, and L. Zhou, "High sensitivity and specificity in human breast cancer detection with near-infrared imaging," in Digest of Topical Meeting on Biomedical Optical Spectroscopy and Diagnostics (Optical Society of America, Washington, D.C., 2002), pp. 450–455.

7. E. M. Sevick, G. Lopez, J. S. Reynolds, T. L. Troy, and C. L. Hutchinson, "Fluorescence and absorption contrast mechanism for biomedical optical imaging using frequency-domain techniques," Photochem. Photobiol. 66, 55–64 (1997).

8. H. Liu, Y. Song, K. L. Worden, X. Jiang, A. Constantinescu, and R. P. Mason, "Noninvasive investigation of blood oxygenation dynamics of tumors by near-infrared spectroscopy," Appl. Opt. 39, 5231–5243 (2000).

9. D. A. Boas, D. H. Brooks, E. L. Miller, C. A. DiMarzio, M. Kilmer, R. J. Gaudette, and Q. Zhang, "Imaging the body with diffuse optical tomography," IEEE Signal Process. Mag. 18, 57–75 (2001).

10. X. Li, T. Durduran, A. Yodh, B. Chance, and D. N. Pattanayak, "Diffraction tomography for biomedical imaging with diffuse-photon density waves," Opt. Lett. 22, 573–575 (1998).

11. Y. Yao, Y. Wang, Y. Pei, W. Zhu, and R. L. Barbour, "Frequency-domain optical imaging of absorption and scattering distributions by a Born iterative method," J. Opt. Soc. Am. A 14, 325–341 (1997).

12. M. A. O'Leary, "Imaging with diffuse photon density waves," Ph.D dissertation (University of Pennsylvania, Philadelphia, Pa., 1996).

13. H. Jiang, "Frequency-domain fluorescent diffusion tomography: a finite-element-based algorithm and simulations," Appl. Opt. 37, 5337–5343 (1998).

14. K. Paulsen and H. Jiang, "Spatially varying optical property reconstruction using a finite element diffusion equation approximation," Med. Phys. 22, 691–701 (1995).

15. S. Arridge and M. Schweiger, "Photon-measurement density functions. Part II: Finite-element-method calculations," Appl. Opt. 34, 8026–8037 (1995).

16. Q. Zhu, T. Dunrana, M. Holboke, V. Ntziachristos, and A. Yodh, "Imager that combines near infrared diffusive light and ultrasound," Opt. Lett. 24, 1050–1052 (1999).

17. Q. Zhu, E. Conant, and B. Chance, "Optical imaging as an adjunct to sonograph in differentiating benign from malignant breast lesions," J. Biomed. Opt. 5, 229–236 (2000).

18. N. G. Chen, P. Y. Guo, S. K. Yan, D. Q. Piao, and Q. Zhu, "Simultaneous near-infrared diffusive light and ultrasound imaging," Appl. Opt. 40, 6367–6380 (2001).

19. N. G. Chen and Q. Zhu, "Characterization of small absorbers inside the turbid medium," Opt. Lett. 27, 252–254 (2002).

20. Q. Zhu, N. G. Chen, and S. Kurtzman, "Imaging tumor angiogenesis using combined near-infrared diffusive light and ultrasound," Opt. Lett. 38, 337–339 (2003).

21. N. G. Chen and J. Bai, "Monte Carlo approach to modeling of boundary conditions for the diffusion equation," Phys. Rev. Lett. 80, 5321–5324 (1998).

22. Y. Pei, H. L. Graber, and R. L. Barbour, "Influence of systematic errors in reference states on image quality and on the stability of derived information for dc optical imaging," Appl. Opt. 40, 5755–5769 (2001).

23. E. M. C. Hillman, J. C. Hebden, F. E. W. Schmidt, S. R. Arridge, M. Schweiger, H. Dehghani, and D. T. Delpy, "Calibration techniques and data type extraction for time-resolved optical tomography," Rev. Sci. Instrum. 71, 3415–3427 (2000).

24. M. Schweiger and S. R. Arridge, "Comparison of two- and three-dimensional reconstruction methods in optical tomography," Appl. Opt. 37, 7419–7428 (1998).

25. M. Firbank, M. Oda, and D. T. Delpy, "An improved design for a stable and reproducible phantom material for use in near-infrared spectroscopy and imaging," Phys. Med. Biol. 40, 955–961 (1995).